HallThruster.jl

1D fluid model for a Hall Thruster discharge

Paul Schedler

MSc Mechanical Engineering

MSc Thesis

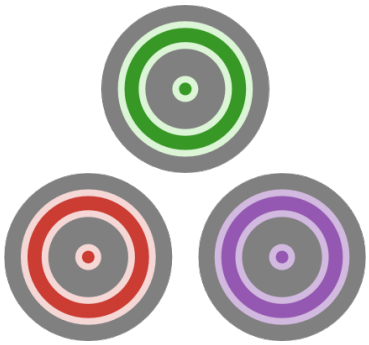

Institute of Fluid Dynamics
Eidgenössiche Technische Hochschule Zürich, Switzerland

conducted at
Plasmadynamics and Electric Propulsion laboratory
Department of Aerospace Engineering
University of Michigan, Ann Arbor

Advisor UM: Prof. Benjamin Jorns
Advisor ETH: Prof. Patrick Jenny

Acknowledgements

I would like to thank PEPL PhD student Thomas Marks for the helpful guidance and support in learning Julia. It was great co-developing HallThruster.jl with you. I thank Prof. Benjamin Jorns for hosting me at the University of Michigan and for challenging my assumptions which led me to gain a better understanding of fundamental plasma physics. Thank you to all the PEPL lab members, the discussions with you offered an extraordinary amount of insight spiced up by good and sometimes not so great humor.

Abstract

Hall thrusters are a type of electric propulsion offering a high specific impulse $1500-4000$s and efficiencies > 50 %. They are by far the dominant type of electric propulsion in the power segment of $1 - 100$ kW. Even though these thrusters have been used in space for decades, predictive Hall thruster simulations remain inaccessible. When treating the plasma discharge as a fluid, as commonly done to reduce computational complexity, the electron conductivity is vastly underpredicted. This gave rise to a correction factor termed anomalous collision frequency. Finding a form of the anomalous collision frequency that is valid over a wide range of operating conditions and geometries has proven to be a major challenge. Current efforts are focused on applying data-driven methods to isolate governing parameters and subsequently calibrate anomalous collision frequency models. This procedure requires quick simulations to generate large datasets, which can be achieved at the expense of physical fidelity. Consequently, a 1D fluid model is desireable. This thesis is thus on the development of a 1D fluid model for Hall thruster discharges, HallThruster.jl. The governing equations are presented and the implmentation in the programming language Julia is discussed. The model is efficient while allowing flexibility, enabling the user to adapt the underlying physics. HallThruster.jl is verified and a comparison to higher fidelity codes is explored systematically by employing a Hall Thruster efficiency model and investigating the impact of assumptions on the individual terms.

List of Abbreviations

Abbreviation	Property
CFL	Courant Friedrich Lewis
CNRS	French National Research Institute
ECR	Electron Cyclotron Thruster
EnKF	Ensemble Kalman Filter
FDM	Finite Difference Method
FFT	Fast Fourier Transform
FVM	Finite Volume Method
FVS	Flux Vector Splitting
GEO	Geostationary Earth Orbit
GIT	Gridded Ion Thruster
GLF	Global Lax-Friedrichs
Hall2De	Fluid code developed by JPL
HALLIS	Hybrid code developed by University of Toulouse and CNRS
HET	Hall Effect Thruster
HLLE	Harten Lax van-Leer Einfeldt
HYPHEN	Hybrid code developed by UM3C
ITAR	International Traffic in Arms
JPL	Jet Propulsion Laboratory
LANDMARK	Low temperature magnetized plasma benchmarks
LEO	Low Earth Orbit
LHS	Left Hand Side
LLF	Local Lax-Friedrichs
MUSCL	Monotonic upstream-centered scheme for conservation laws
NASA	National Aeronautics and Space Administration
NND	Non-neutral drift diffusion
ODE	Ordinary Differential Equation
OVS	Order verification study
PDE	Partial Differential Equation
PEPL	Plasmadynamics and Electric Propulsion laboratory
PIC	Particle-in-cell
PSD	Power Spectral Density
QDD	Quasineutral Drift Diffusion
REA	Reconstruct, Evolve, Average
RHS	Right Hand Side
RMF	Rotating Magnetic Field
SPT	Stationary Plasma Thruster
TVD	Total-Variation Diminishing
WENO	Weighted essentially non-oscillatory

List of Symbols

Physical constants

Symbol	Value	Unit	Description
k_B	$1.380649 * 10^{-23}$	$[m^2 kg s^{-2} K^{-1}]$	Boltzmann constant
e	$1.602176634 * 10^{-19}$	$[C]$	Elementary charge
m_e	$9.10938356 * 10^{-31}$	$[ms^{-2}]$	Electron mass
R_0	8314.46261815324	$[Jkmol^{-1}K]$	Universal gas constant
g	9.81	$[ms^{-2}]$	Gravitational acceleration on Earth
ε_0	$8.85418782 * 10^{-12}$	$[m^{-3}kg{-}1s^4A^2]$	Permettivity of free space

Variables

Symbol	Unit	Description
$_n$	$[-]$	Subscript n refers to neutrals
$_i$	$[-]$	Subscript i refers to ions
$_{ij}$	$[-]$	Subscript ij refers to ions of charge state j
$_e$	$[-]$	Subscript e refers to electrons
Δv	$[ms^{-1}]$	Delta v, change in velocity
M_i	$[kg]$	Initial mass
M_f	$[kg]$	Final mass
I_{sp}	$[s]$	Specific impulse
m_α	$[kg]$	Atom mass of species α
u_0	$[ms^{-1}]$	Velocity at presheath edge
ϕ_0	$[V]$	Potential at presheath edge
u	$[ms^{-1}]$	Depending on application mean or bulk velocity
$\mathbf{u}$	$[ms^{-1}]$	Depending on application mean or bulk velocity vector
v'	$[ms^{-1}]$	Random part of velocity
$\mathbf{v}'$	$[ms^{-1}]$	Random part of velocity vector
$\mathbf{v}$	$[ms^{-1}]$	Velocity vector
n_0	$[m^{-3}]$	Number density at presheath edge
n_α	$[m^{-3}]$	Number density of species α
$\dot{n}_\alpha$	$[m^{-3}t^{-1}]$	Rate of change of number density of species α
T_α	$[K]$	Temperature of species α
$T_{\alpha v}$	$[eV]$	Temperature of species α
$\mathbf{B}$	$[T]$	Magnetic field vector
$\mathbf{E}$	$[Vm^{-1}]$	Electric field vector
B_r	$[T]$	Radial magnetic field
E_z	$[Vm^{-1}]$	Axial electric field
$f(\mathbf{x}, \mathbf{v}, t)$	$[-]$	Particle distribution function, 3 dimensions in space, 3 in velocity space, 1 in time
$\mathbf{x}$	$[m]$	Space vector
$\mathbf{a}$	$[ms^{-2}]$	Acceleration-space vector
$C_{\alpha\beta}$	$[s^{-1}]$	Operator relating change in species α due to collisions with species β
$\mathbf{F}$	$[N]$	Three dimensional force vector
$\hat{n}$	$[-]$	Normal vector to a surface
q_α	$[C]$	Charge state of species α
$\mathbf{R}_{\alpha\beta}$	$[N]$	Drag force vector for species α due to collisions with species β

Symbol	Unit	Description
$\mathbf{P}$	$[Nm^{-2}]$	Pressure tensor
p	$[Nm^{-2}]$	Scalar pressure
$\mathbf{j}$	$[Am^{-2}]$	Current density vector
j	$[Am^{-2}]$	Scalar current density
S_{loss}	$[Js^{-1}]$	Summation of electron power loss terms
Ω_α	$[-]$	Hall parameter of species α
$\omega_{c\alpha}$	$[s^{-1}]$	Cyclotron frequency of species α
ν_α	$[s^{-1}]$	Total momentum transfer collision frequency of species α
$\nu_{\alpha\beta}$	$[s^{-1}]$	Collision frequency of species α with species β
ν_{AN}	$[s^{-1}]$	Anomalous electron momentum transfer collision frequency
Z	$[-]$	Charge state
$\langle Z \rangle$	$[-]$	Number averaged charge state
σ	$[Cm^{-3}]$	Charge density
$\mu_\perp$	$[Cskg^{-1}m^{-3}]$	Cross-field electron mobility
$k_{\alpha j}$	$[m^3s^{-1}]$	Ionization rate coefficient for species α to charge state j
$\sigma_{\alpha\beta}$	$[m^2]$	Collissional cross section for collisions of species α with species β
$ln(\lambda)$	$[m]$	Coulomb logarithm
t	$[s]$	time
I	$[A]$	Current
ρ_c	$[m]$	Cyclotron radius
ϕ_s	$[V]$	Sheath potential
L_{ch}	$[m]$	Thruster channel length
L	$[m]$	Domain length
l	$[m]$	Mean free path
τ_α	$[s]$	Total collisional time constant of species α
γ	$[-]$	Secondary electron emission coefficient
ϵ	$[eV]$	Electron internal energy, defined as $\frac{3}{2}T_{ev}$
F_i	$[whatever]$	Flux at location i
c_i	$[ms^{-1}]$	Speed of sound at location i
s_i	$[ms^{-1}]$	Wavespeed at location i
Δt	$[s]$	timestep
Δx	$[m]$	numerical cell size
e_i	$[-]$	Normalized error at location i
η_a	$[-]$	Anode efficiency
η_m	$[-]$	Mass utilization efficiency
η_d	$[-]$	Beam divergence
η_v	$[-]$	Voltage utilization efficiency
η_b	$[-]$	Beam utilization efficiency
η_q	$[-]$	Charge correction factor
V_a	$[V]$	Effective acceleration voltage
V_d	$[V]$	Applied discharge potential
I_b	$[A]$	Beam current (total ion current)
I_{bz}	$[A]$	Axial component of beam current
I_d	$[A]$	Discharge current

List of Figures

Contents

Chapter 1

Introduction

Human civilization is rapidly turning into a more and more space-faring society. Both commercial and governmental players are sending ever more spacecraft into orbit to exploit the potentials offered for communications, surveillance and science. In fact, Goldman Sachs estimates the space industry compound annual rate of growth at 9% until 2040. [2]. This would turn what is now a global ≈ 500 billion USD market into a multi-trillion USD industry. The ever higher number of satellites associated with this growth need effective propulsion systems.

Historically, most of mankind's activity in space has been propelled by chemical rocket engines. They convert thermal (random kinetic) energy created by combustion into directed kinetic energy, producing thrust in the opposite direction. Electric propulsion encompasses all thrusters where electricity is used in one form or another to impart additional energy on the propellant. They can roughly be characterised in three categories: electrothermal, electrostatic and electromagnetic. Arcjets and resistojets belong to the first category. They operate on the same principle as chemical rocket engines, albeit extra energy is not added through combustion but a discharge arc or resistive heating. Like in chemical rocket engines, electrothermal thrusters are constrained by materials within the heating region which introduces a limit on the maximum temperature and thus on the gas exhaust velocity.

In other types of electric propulsion, thrust is generated by directly accelerating a propellant using electrostatic or electromagnetic forces. The direct acceleration mechanism allows these thrusters to generate exhaust velocities much higher than systems converting thermal energy into kinetic energy through expansion. The impulse is directly related to the exhaust velocity through the famous Tsiolkovsky equation.

$$\Delta v = g I_{sp} ln \left(\frac{M_i}{M_f} \right) \tag{1.1}$$

The specific impulse I_{sp} is defined such that its product with g gives the exhaust velocity v_e. The propellant launch mass can be up to 50% of the total spacecraft mass for satellites powered by chemical engines, while electric propulsion keeps this mass ratio usually below 10% since the specific impulse is up to an order of magnitude higher, $1500 - 5000$s vs $200 - 500$s. In space missions, launch costs can account for up to 40% of total mission cost. [3] Consequently electrically powered thrusters enjoy a huge competitve advantage. On the flipside, penalties associated with electric propulsion do in general include a relatively high power consumption, possibly the need for power electronics and a relatively heavy thruster. Detailed mission analysis and design is required to determine the exact advantages and drawbacks of certain propulsion systems.

Considering electromagnetic and electrostatic propulsion, Hall Thrusters along with Gridded Ion Thrusters (GIT) are the oldest and most mature technologies. More recent developments are electrospray thrusters, electron cyclotron resonance thrusters (ECR) and rotating magnetic field (RMF) thrusters. The latter two are in a rather early stage of their development, with possible applications over a wide range of powers. Electrospray thrusters are very competitive in the low power segment and widely used on small satellites. GIT's are the most efficient high power electric propulsion thruster today, but are limited in current density and consequently relatively large and heavy. While the specific impulse of Hall thrusters is typically slightly lower than GITs, their current density can be much higher and the devices are therefore smaller and lighter. At the same time the elimination of extractor grids simplifies the mechanical design. This explains why Hall Thrusters are the by far most successful type of electric propulsion in the power segment from 1 kW to 100 kW.

1.1 Hall Thrusters

Thus far, Hall Thrusters have been mostly used for station keeping on LEO and GEO satellites while occupying a niche market segment. However, mainly through SpaceX's starlink satellites, the amount of Hall Thrusters in orbit has recently increased drastically. In addition, through continuous improvement and magnetic field profiles reducing erosion [4], lifetimes are now sufficiently long to be used on space exploration missions as well. [5]

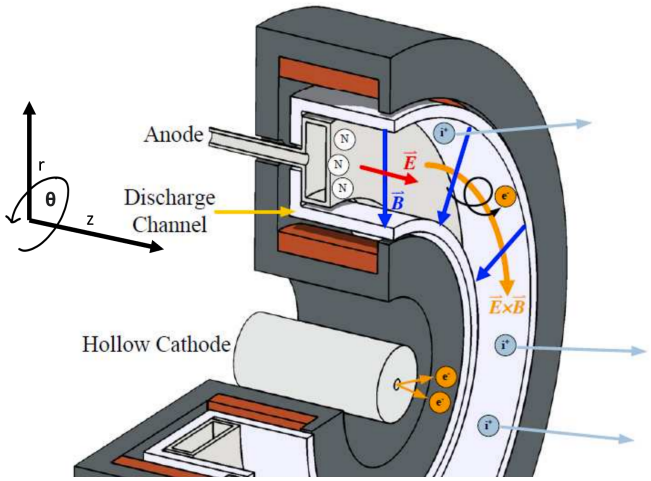

(a) Isometric schematic of a Hall Thruster [6]

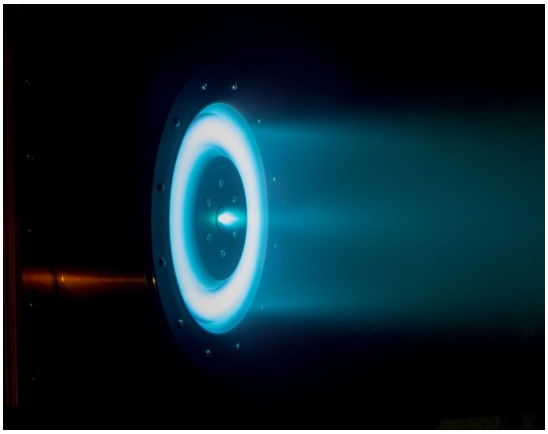

(b) The University of Michigan's H9 9kW magnetically shielded thruster in operation

Figure 1.1

A schematic of an axisymmetric Hall Thruster with center mounted cathode is shown in Figure 1.1a. A potential difference is generated by an anode and a hollow cathode, perpendicular to a magnetic field applied by coils on the outer walls and centerline of the thruster. This results in electrons being trapped along the radial magnetic field lines, creating a strong azimuthal $\mathbf{E} \times \mathbf{B}$ Hall current. The energized electrons ionize injected neutral gas, usually xenon. The ions are then accelerated out of the channel by an axial electric field, which generates thrust. The axial electric field is sustained by the lowered electron conductivity towards the anode. Hall thrusters offer a specific impulse on the order of 1500-3000s, and can achieve efficiencies higher than 50% [7].

The plasma state in Hall Thrusters is characterized as a low temperature magnetized plasma. Electron energies are on the order of 10s of eV, while ions and neutrals remain cold. Magnetized refers to the fact that the electron motion in magnetic cross field direction is hindered as they are entrained in a cyclotron motion along magnetic field lines. This is illustrated in the discharge channel in Figure 1.1a.

In operation, Hall thrusters exhibit dynamic instabilities that remain poorly understood. A low frequency oscillation termed the breathing mode in the axial direction can be found in the $10 - 50$ kHz range. The name stems from the nature of the oscillation, since it is related to neutral depletion and ionization instabilities. In the past, the breathing mode has been studied using a simple predator-prey model [8], where the ionization rate coefficient as a function of electron temperature is the key variable. Linear perturbation theory applied to a 1D axial model can recover breathing mode oscillations as well. Recently, [9] have found the breathing mode to arise due to non-linearities in the electron power consumption, while [10] believe the main reason is an ion back-flow towards the anode. Consequently there is no consensus on the origin of the breathing mode at this point.

A slightly higher frequency oscillation at 100 to 500 kHz is related to the ion residence time in the

channel, commonly referred to as transit time oscillations. Wave-driven oscillations in the MHz range persist in the azimuthal direction [11]. Cumulatively, these instabilities lead to 3 dimensional turbulent effects and wave driven transport phenomena.

Hall Thruster discharges can be modelled using particle in cell (PIC) simulations, fluid models or hybrids in between the two. Three dimensional kinetic models could resolve the previously mentioned instabilities, but are usually too expensive to model for full scale thrusters, as plasma Debye lengths can be on the order of μm and thruster sizes on the order of cm. An example of a kinetic model is [12]. The ions and electrons can be approximated relatively well as fluids, since the mean free path to length scale ratio is low owing to electrostatic collisions. As neutrals can only exchange momentum in direct collisions, their velocity distribution is less Maxwellian and the fluid formulation is less valid. Hall2De [13] developed at JPL is an example of a fluid code. HYPHEN [14] and HALLIS [15] are hybrid codes treating neutrals and ions as particles, while resorting to a fluid approach for the electrons. The axial symmetry of Hall Thrusters is exploited in all of the above mentioned models, reducing the problem to two dimensions. The r-z domain (see Figure 1.1a for the coordinate system) is the preferred plane for Hall Thruster models aiming to predict the global plasma state and thruster properties. Axial-azimuthal simulations are mostly used to study instabilities and wave-driven phenomena.

The electron cross-field transport towards the anode in a Hall thruster discharge is strongly underestimated when applying fluid and hybrid models. The experimental transport is orders of magnitude higher than predicted by the generalized Ohm's law, Equation 2.18. The equation is will be explained in detail, however it is noted here that it only takes classical collisions into account. It is generally accepted that electron cross field transport is enhanced by kinetic microinstabilities [16], which cannot be captured using a fluid formulation by definition. In order to deal with the discrepancy between fluid theory and experiment, the usual approach is to add an anomalous (in contrast to classical) collision frequency ν_{AN}. This creates a closure problem, requiring additional insights.

Thus far, zero-equation closure models derived from first principles could match experimental data in specific operating conditions, but failed to generalize to a broader range of conditions. Jorns [17] has been able to exploit a data driven approach to generate a closure model, and could identify some parameters that are likely related to cross-field electron transport. This model has been applied in Chapter 5. In 2D simulations, additional terms may be required, as the channel dynamics are usually treated differently than the cathode plume transport, leading to two closure problems. The models need to be calibrated, which is formulated as a Bayesian inference problem to be able to quantify uncertainties. Marks et al. [18] have been able to exploit a data-driven approach with higher predictability towards thrusters and conditions not included in the training data. In order to simulate high number of different initial conditions and perform parameter studies with increased search area, a 1D model is desirable due to lower computational cost compared to higher dimensional models.

To summarize, even though Hall thrusters have been flown for decades, predictive simulations remain inaccessible at this point. Finding a general model for anomalous electron transport is the holy grail. One attempt to get there is by employing data driven approaches. Therefore, in order to perform a high number parameter studies with increased search area, a 1D model is desirable due to lower computational cost compared to higher dimensional models. Consequently, this work is on developing a 1D model satisfying this need.

1.2 HallThruster.jl

0D Lotka-Volterra models do not resolve the plasma evolution in space at all, while 2D simulations are expensive to evaluate. To fill the data-gap, a one dimensional fluid model is a good compromise between fidelity and computational cost. Axial state propagation is achieved, and axial instabilities such as the breathing mode and transit time oscillations can be resolved. This results in the ability to run calibrated data-driven models for anomalous electron transport that are a function of the plasma state. While the radial direction is not modelled at all, different energy loss terms can in part account for the change in geometry. One advantage is that the magnetic field profile along the centerline of the thruster channel is usually close to being purely radial. The transformation from a 3 dimensional thruster to a 1D domain is shown in Figure 1.2. Shown on the left is the University of Michigan's H9 magnetically shielded Hall Thruster with a center mounted cathode.

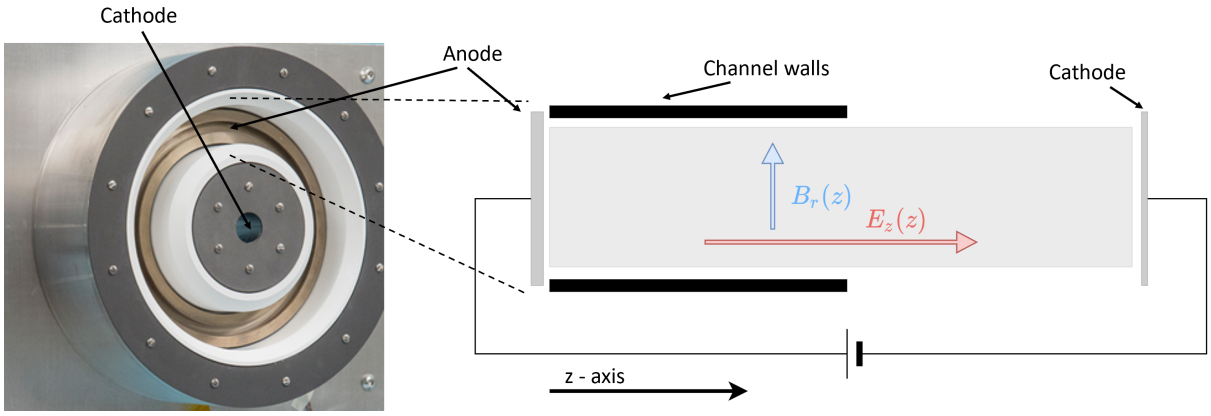

Figure 1.2: Illustration of 1D domain

Due to dimensionality one, the left boundary will always correspond to the anode and the right boundary to the cathode, even if an axial domain of multiple channel lengths is simulated. While obviously reducing fidelity drastically, this approximation does not render the model useless since the magnetic field profile can be imposed as a function of space, informed by the real centerline magnetic field. It is the radial magnetic field strength that governs the (at least classical) electron resistivity in axial domain and therefore gives rise to the axial electric field. Thus, even though the position of the cathode might be far off geometrically speaking, the magnetic field profile ensures the potential structure and peak electric field are at similar axial positions as in a 2D simulation.

1D fluid models have been studied by the Hall thruster community since the 1990's [19]. Early models did not self-consistently evaluate the electron temperature, but rather imposed a given profile. Hagelaar et al. [20] decreased the computational effort by implicitly treating the source terms appearing in the electron energy equation. 1D models were then extensively used to study axial instabilities, with mostly non-conclusive results. Even though many 1D codes have been developed and some are openly accessible, none were found that are easily extensible and can be adapted to the needs of the user. This limitation renders those models not very useful for inference tasks. The model developed here, HallThruster.jl, is based on previously formulated models, especially [11], [21] and [22]. In an effort to contribute to open science, HallThruster.jl is open source and available on Github. [23]

The following chapter describes the physics model of HallThruster.jl, while Chapter 3 describes the discretization and numeric implementation of the equations. Chapter 4 deals with verification and model behaviour is discussed. Subsequently, results from HallThruster.jl are compared to a 2D higher fidelity simulation applying a data-driven anomalous transport model in Chapter 5. A conclusion and clear recommendations for future work are offered in Chapter 6.

Chapter 2

Governing Equations

This chapter focuses on deriving and presenting the governing model equations to inform physics represented in HallThruster.jl. In Section 2.1 the Euler equations are derived from the Vlasov equation following [24]. These equations are restated in the exact way implemented for neutrals, ions and electrons in Section 2.2. Further assumptions and a simplification to the electron momentum equation is shown in Section 2.3. The source terms appearing in the equations and the collisions governing electron transport are introduced in Section 2.4. As the electron transport is vastly underpredicted in classical models, the standard methodology addressing the problem is presented in Section 2.5. The electron energy loss terms are discussed in Section 2.6. The resulting physical 1D model behind the equations implemented in HallThruster.jl relies on a lot of assumptions, which are summarized in Section 2.8. This is done both to gain an overview for convenience and additionally provides an opportunity to discuss the limitations of the model.

2.1 Derivation of fluid equations from Vlasov equation

Leaving the macroscopic view of continuous fields, the Vlasov equation describes the evolution of discrete particles of a single species in phase space. The constituents are merely described by two properties: position and velocity. The Vlasov equation can be written as

$$\frac{\partial f}{\partial t} + \mathbf{v} \cdot \frac{\partial f}{\partial \mathbf{x}} + \mathbf{a} \cdot \frac{\partial f}{\partial \mathbf{v}} = 0 \tag{2.1}$$

where $f(\mathbf{x}, \mathbf{v}, t)$ is the distribution function, $\mathbf{x}$ is the three dimensional space distribution while $\mathbf{v}$ is the three dimensional velocity distribution. Equation 2.1 can be written as is since $\mathbf{x}$ and $\mathbf{v}$ are independent variables. It is assumed, that as particles collide, their position in space does not change much over the course of their encounter, but their position in velocity space can be altered substantially. To model the sinks and sources of particles in phase-space, a collision operator is added to the Vlasov equation.

$$\frac{\partial f_\alpha}{\partial t} + \frac{\partial (\mathbf{v} f_\alpha)}{\partial \mathbf{x}} + \frac{\partial (\mathbf{a} f_\alpha)}{\partial \mathbf{v}} = \sum C_{\alpha\beta}(f_\sigma) \tag{2.2}$$

where $C_{\alpha\beta}(f_\alpha)$ represents the rate of change of f_α as a result of collisions of species α with species β. The collision operator has to satisfy a number of properties, namely conservation of particles in total, conservation of momentum of a specific species for collisions with only that species and conservation of momentum of all species for collisions involving multiple species. Similarly the collision operator has to conserve total energy of a species for collisions involving only that species, and conserve the total energy of multiple species for interspecies collisions. See chapter 2 in [24] for a mathematical definition of these constraints, here merely conservation of particles is repeated in Equation 2.3.

$$\int d\mathbf{v} C_{\alpha\beta}(f_\alpha) = 0 \tag{2.3}$$

Fluid equations can be derived by taking moments of the Vlasov equation. Looking at the distribution function $f(\mathbf{x}, \mathbf{v}, t)$ alone, one can effectively average over the velocity distribution by integrating with respect to it and obtain the macroscopic fluid properties density and mean velocity.

$$n(\mathbf{x}, t) = \int f(\mathbf{x}, \mathbf{v}, t) d\mathbf{v} \tag{2.4}$$

$$u(\mathbf{x}, t) = \frac{\int \mathbf{v} f(\mathbf{x}, \mathbf{v}, t) d\mathbf{v}}{n(\mathbf{x}, t)} \tag{2.5}$$

Integrating Equation 2.2 over velocity space is taking the 0th moment of the Vlasov equation. $\mathbf{x}$, $\mathbf{v}$ and t being independent, the first two terms on the left hand side commute with time and space. Gauss'

theorem, $\int_{volume}(\nabla \cdot \mathbf{F})d\mathbf{x} = \int_{surface}(\mathbf{F} \cdot \hat{\mathbf{n}})d\mathbf{s}$ can be applied to the third term on the left hand side which results in f_σ being evaluated at $v = \infty$. This term disappears as the amount of particles with velocity infinity approaches 0.
The continuity equation therefore results in

$$\frac{\partial n}{\partial t} + \nabla \cdot (n\mathbf{u}) = 0 \tag{2.6}$$

The right hand side is 0 since the amount of particles is conserved when considering one fluid only. In modelling a Hall thruster discharge, multiple fluids are present and this term will therefore be non-zero and corresponding to ionization and recombination rates. Treatment of the source terms applied in the fluid equations to model Hall thrusters is described in Section 2.4.

The first moment is obtained by multiplying Equation 2.2 by $\mathbf{v}$ and integrating again over $d\mathbf{v}$

$$\frac{\partial n_\alpha \mathbf{u}_\alpha}{\partial t} + \frac{\partial}{\partial \mathbf{x}} \cdot \int (\mathbf{v}'\mathbf{v}' + \mathbf{v}'\mathbf{u}_\alpha + \mathbf{v}'\mathbf{u}_\alpha + \mathbf{u}_\alpha\mathbf{u}_\alpha) f_\alpha d\mathbf{v}' - \frac{q_\alpha}{m_\alpha} \int (\mathbf{E} + \mathbf{v} \times \mathbf{B}) f_\alpha d\mathbf{v}' = -\frac{1}{m_\alpha}\mathbf{R}_{\alpha\beta} \tag{2.7}$$

$\mathbf{R}_{\alpha\beta}$ is the drag force resulting from collisions between species α and β. These momentum transfer collisions and the operator will be treated in Section 2.4. Equation 2.7 can be rewritten into

$$\frac{\partial n_\alpha \mathbf{u}_\alpha}{\partial t} + \frac{\partial}{\partial \mathbf{x}} \cdot (n_\alpha \mathbf{u}_\alpha \mathbf{u}_\alpha + \frac{\mathbf{P}_\alpha}{m_\alpha}) = n_\alpha q_\alpha (\mathbf{E} + \mathbf{u}_\alpha \times \mathbf{B}) - \mathbf{R}_{\alpha\beta} \tag{2.8}$$

This is effectively the ion momentum equation solved in HallThruster.jl. The stress tensor and viscosity are neglected. A closure problem is evident for the pressure term. The pressure tensor is defined as $\mathbf{P} = m_\alpha \int \mathbf{v}'\mathbf{v}' f_\alpha d\mathbf{v}'$. It is assumed that the distribution function is isentropic, which leads to the following definition of scalar pressure. This assumption is considered acceptable as particle and coulomb collisions drive the distribution towards isotropy.

$$\mathbf{P}_\alpha = \frac{m_\alpha}{3} \int \sum_{j=1}^{3} v'^2_j f_\alpha d^3\mathbf{v}' \tag{2.9}$$

The dimensionality is three as HallThruster.jl is supposed to approximate a 3D discharge, even though it solves a one dimensional system. This is done to account for the three dimensional effects of the force exerted by the pressure, and a similar approach will be applied to the energy equation. The ideal gas law $P_\alpha = n_\alpha k_B T_\alpha$ is used as the thermodynamic relation to compute P_α in HallThruster.jl.
The Vlasov equation is multiplied by $m_\alpha v^2/2$ and integrated over velocity to obtain the second moment, which results in the energy equation. The dimensionality is once again three.

$$\frac{\partial}{\partial t} \int \frac{m_\alpha v^2}{2} f_\alpha d^3\mathbf{v} + \frac{\partial}{\partial x} \cdot \int \frac{m_\alpha v^2}{2} \mathbf{v} f_\alpha d^3\mathbf{v} + q_\alpha \int \frac{v^2}{2} \frac{\partial}{\partial \mathbf{v}} \cdot (\mathbf{E} + \mathbf{v} \times \mathbf{B}) f_\alpha d^3\mathbf{v} = \sum_\alpha \int m_\alpha \frac{v^2}{2} C_{\alpha\beta} f_\alpha d^3\mathbf{v} \tag{2.10}$$

The collision term on the right hand side refers to the rate at which energy is lost due to collisions with other species and will be written as S_{loss} in the following. This term will be extended in Section 2.6 to include additional losses not related to collisions to account for the finite domain. As in the momentum equation, the stress tensor and the associated macroscopic property viscosity is neglected. Equation 2.10 can be simplified by integration, for details the reader is referred to chapter 2 in [24]. This results in the following.

$$\frac{\partial}{\partial t}\left(\frac{3}{2}P_\alpha + \frac{m_\alpha n_\alpha u_\alpha^2}{2}\right) + \nabla \cdot \left(\mathbf{Q}_\alpha + \frac{5}{2}P_\alpha \mathbf{u}_\alpha + \frac{m_\alpha n_\alpha u_\alpha^2}{2}\mathbf{u}_\alpha\right) - q_\alpha n_\alpha \mathbf{u}_\sigma \cdot \mathbf{E} = -S_{loss} \tag{2.11}$$

In order to derive an equation for the evolution of internal energy, Equation 2.8 can be multiplied with $\mathbf{u}_\alpha$ and inserted into Equation 2.11.

$$\frac{3}{2}\frac{dP_\alpha}{dt} + \nabla \cdot \left(\frac{5}{2}P\mathbf{u}_\alpha + \mathbf{Q}_\alpha\right) = \mathbf{j}_\alpha \cdot \mathbf{E} - S_{loss} \tag{2.12}$$

The Ohmic heating term $\mathbf{j}_\alpha \cdot \mathbf{E}$ is only valid if the kinetic energy is negligible. In this form it solely consists of frictional heating. The term represents conversion of directed kinetic energy into random kinetic energy, which is thermal energy. However, if the electric field becomes negative, the meaning of the term becomes unphysical. Depending on the boundary conditions, this can happen close to the anode. This is further discussed in Section 2.8 and Section 4.3.

2.2 Fluid equations HallThruster.jl

The canonical fluid continuity, momentum and energy equations derived from the Vlasov equation in the previous section are known collectively as the Euler equations. HallThruster.jl solves the neutral continuity equation, thereby assuming constant neutral velocity and constant temperature. For each of the up to three ion fluids the isothermal Euler equations are solved, which are the continuity and momentum equation. As quasineutrality is assumed, the electron density is determined as a function of cumulative ion density, while additional assumptions are made on the electron momentum equation, which greatly simplifies the expression and reduces computational complexity, see Section 2.3. The electron internal energy equation is solved to solve for the electron energy profile along the domain, which drives the ionization profile and therefore has strong influence in the overall discharge properties. The assumptions and their validity leading to this system of equations are summarized in Section 2.8. In the following, the governing equations are mentioned explicitly. The source terms are discussed and defined in the following sections.

Neutrals

The neutral continuity equation is one to one Equation 2.6 with an added source term for ionization.

$$\frac{\partial n_n}{\partial t} + \frac{\partial}{\partial z}(n_n u_n) = \dot{n}_n \tag{2.13}$$

Ions

The ion continuity equation is one to one Equation 2.6 with an added source term for ionization.

$$\frac{\partial n_{ij}}{\partial t} + \frac{\partial}{\partial z}(n_{ij} u_{ij}) = \dot{n}_{ij} \tag{2.14}$$

The ion momentum equation is derived from Equation 2.8, neglecting the contribution by the magnetic field (unmagnetized ions) and momentum transfer from other species to ions. See Section 2.8 for reasoning and justification.

$$\frac{\partial}{\partial t}(n_{ij} u_{ij}) + \frac{\partial}{\partial z}(n_{ij} u_{ij}^2 + \frac{p_{ij}}{m_i}) = \frac{je}{m_i} n_{ij} E_z \tag{2.15}$$

Electrons

Quasineutrality eliminates the need for an electron continuity equation, the electron momentum equation is simplified in Section 2.3 applying a number of assumptions. The electron energy equation is derived from Equation 2.12.

$$\frac{\partial}{\partial t}\left(\frac{3}{2}n_e k_B T_e\right) + \frac{\partial}{\partial z}\left(\frac{5}{2}n_e k_B T_e u_{ez} + q_{ez}\right) = e n_e u_{ez}\frac{\partial \phi}{\partial z} - S_{loss} \tag{2.16}$$

2.3 Current conservation and electron drift diffusion approximation

As the electrons are very light and a fast moving species, representing their non-linear advection in a momentum equation would lead to severe timestepping restrictions in a fluid solver. Consequently, to reduce computational expense, the electron momentum equation is simplified. Assuming quasineutrality , neglecting electron inertia and looking at a steady state while removing the embedded continuity equation, the electron momentum equation can be rewritten from Equation 2.8 into

$$\nu_e \frac{m_e}{e}\mathbf{j}_e = e n_e \mathbf{E} + \nabla p_e - \mathbf{j}_e \times \mathbf{B} \tag{2.17}$$

In Equation 2.17 the collisional term $\mathbf{R}$ is assumed of the form $\mathbf{R}_{total} = \mathbf{R}_{ei} + \mathbf{R}_{en} = m_e n_e(\nu_{ei}(\mathbf{u}_e - \mathbf{u}_i) + \nu_{en}(\mathbf{u}_e - \mathbf{u}_n))$. As neutral and ion velocity are assumed small compared to electron velocity, both contributions can be dropped and $\nu_e = \nu_{ei} + \nu_{en}$ encapsulating both electron ion and electron neutral collision frequencies. Applying this equation to a 1D geometry and assuming that the magnetic field is purely radial, Equation 2.17 can be split in the axial and azimuthal directions.

$$j_{ez} = \frac{e^2 n_e}{m_e \nu_e}\frac{1}{1+\Omega_e^2}\left(E_z + \frac{1}{e n_e}\frac{\partial p_e}{\partial z}\right) \tag{2.18}$$

$$j_{e\theta} = \Omega_e j_{ez} \tag{2.19}$$

where $\Omega_e = \omega_{ce}/\nu_e = e|B|/m_e\nu_e$ is the Hall Parameter. It is the ratio of the electron cyclotron frequency to the electron momentum transfer collision frequency and can be interpreted as a measure of how magnetized the electrons are. The first two fractions on the right hand side of Equation 2.18 are often referred to as the cross-field electron mobility $\mu_\perp$.

$$\mu_\perp = \frac{e n_e}{m_e \nu_e}\frac{1}{1+\Omega_e^2} \tag{2.20}$$

Equation 2.18 vastly underpredicts the electron current in a Hall Thruster by orders of magnitude. As a result, the scientific community has introduced an anomalous collision frequency, which is supposed to take into account the physics being missed by a fluid formulation. Aid in finding better approximations of ν_{AN} is the primary reason HallThruster.jl was developed. This is further thematized in Section 2.5.

The charge density σ is zero since quasineutrality is assumed. As multiple ion species are allowed, ion and electron currents are first summed and then inserted in the charge continuity equation.

$$\sigma = \sum_{j=1}^{3} j\ n_{ij} - n_e \tag{2.21}$$

$$j_{iz} = \sum_{j=1}^{3} j\ n_{ij} u_{ij} \tag{2.22}$$

$$\frac{\partial \sigma}{\partial t} + \frac{\partial}{\partial z}\left(j_{iz} - j_{ez}\right) = 0. \tag{2.23}$$

Equation 2.18 can be substituted in Equation 2.23 to obtain

$$\frac{\partial}{\partial z} j_{iz} - \frac{\partial}{\partial z}\left(\mu_\perp e\left(-\frac{\partial \phi}{\partial z} + \frac{1}{e n_e}\frac{\partial p_e}{\partial z}\right)\right) = 0. \tag{2.24}$$

Electrostatics is assumed rewrite E as $-\frac{d\phi}{dz}$. Rewriting for the potential results in an elliptic equation that can be evaluated self-consistently.

$$\frac{\partial}{\partial z}\left(\mu_\perp n_e \frac{\partial \phi}{\partial z}\right) = \frac{\partial}{\partial z}\left(\frac{\mu_\perp}{e}\frac{\partial p_e}{\partial z} - \frac{j_{iz}}{e}\right) \tag{2.25}$$

At this point, all primary equations governing HallThruster.jl have been presented. The source terms and various parameters however require further elaboration, which is handled in the following sections.

2.4 Reaction and collision models

This section deals with the reaction models for species creation through ionization. Elastic collisions are considered and influence electron mobility. Additionally, excitation rates are modelled.

Ionization

The source terms in Equation 2.13 and Equation 2.14 determining the number of ions created in each instance are modelled as a function of the respective densities of electron and reactant species and electron temperature. The rate coefficient is a function of electron temperature.

$$\dot{n}_n = -\sum_{j=1}^{3} n_e n_n k_{nj}(T_e) \tag{2.26}$$

Equation 2.26 is the source term in the neutral continuity equation. n_n is the neutral number density, n_e the electron number density and k_{nj} the rate coefficient. Up to 3 charge states are considered. The ion continuity equations are altered slightly, since ion number density can either increase by ionization from a lower charge state or decrease when ionized to a higher charge state.

$$\dot{n}_{ij} = n_e n_n k_{nj}(T_e) - \sum_{\ell=j+1}^{3} n_e n_{ij} k_{j\ell}(T_e) \tag{2.27}$$

Here, j refers to the charge state of the ion fluid described by Equation 2.27. As evident in these equations, recombination is not modelled. The ionization rate is either a function created by BOLSIG+ [25] or taken from the table provided by the Landmark study. Up to 3 ion fluids are supported by HallThruster.jl, necessitating the modelling of six reactions. The assumptions only hold for monatomic propellants.

$$A + e- \longrightarrow A^{+} + 2e- \tag{2.28}$$
$$A + e- \longrightarrow A^{2+} + 3e- \tag{2.29}$$
$$A + e- \longrightarrow A^{3+} + 4e- \tag{2.30}$$
$$A + +e- \longrightarrow A^{2+} + 2e- \tag{2.31}$$
$$A + +e- \longrightarrow A^{3+} + 3e- \tag{2.32}$$
$$A^{2+} + e- \longrightarrow A^{3+} + 2e- \tag{2.33}$$

Excitation

HallThruster.jl estimates the excitation rates, supplied by lookup tables, of monatomic gases as a function of electron temperature. The excitation states of different fluids are not tracked however, and only impact the electron energy balance described in Section 2.6.

Elastic collisions

Elastic momentum transfer to neutrals and ions is neglected, however electron transfer collisions are considered. A few different models are implemented, and these are described below. $\mu_\perp$ determines the electron mobility across magnetic field lines, and an important parameter in Equation 2.20 is the electron momentum transfer collision frequency ν_e. As stated previously, this consists of the classical collisions ν_c and anomalous collisions ν_{AN}. Collisions between electrons do not alter the total momentum balance of the electrons as a fluid. Therefore ν_{ee} is not considered. Momentum can however be transferred from neutrals and ions.

$$\nu_e = \nu_{ei} + \nu_{en} + \nu_{AN} \tag{2.34}$$

The individual contributions to ν_e are evaluated next.

Electron Neutral collisions

Three different models are implemented to estimate the electron neutral momentum transfer collision frequency. The simplest one is used in Landmark test case 3 [26]. It is a linear function of the neutral density and valid for Xenon.

$$\nu_{en,Landmark} = 2.5 * 10^{-13} * n_n \tag{2.35}$$

Another model to approximate the electron neutral collision frequency is by evaluating a numerical fit for the effective neutral electron collisional cross section as a function of electron temperature, valid for Xenon. [7] [27] This is averaged over a Maxwellian electron distribution.

$$\nu_{en,GK} = \sigma_{en}(T_e) n_n \sqrt{\frac{8eT_e}{\pi m_e}} \tag{2.36}$$

$$\sigma_{en,GK}(T_e) = 6.6 \times 10^{-19} \left[\frac{\frac{T_e}{4} - 0.1}{1 + \left(\frac{T_e}{4}\right)^{1.6}} \right] \ [\mathrm{m}^2] \tag{2.37}$$

Lastly, lookup tables can be provided that estimate a coefficient as a function ϵ, which is then applied to determine the collision frequency as a function of n_n. Further data can be added by the user as well and therefore the model can be extended beyond Xenon and Krypton. The three models are all linear with respect to n_n and are compared with $n_n = 1e20$ in Figure 2.1 as a function of electron temperature. The coefficients in the Lookup tables supplied by HallThruster.jl are obtained by integrating over the cross sections over the velocity distribution, similar to what is being done in BOLSIG+ [25]. These tables were created by PEPL Phd candidate Thomas Marks.

$$\nu_{en,LU} = n_n * k_{en,LU}(\epsilon) \tag{2.38}$$

Electron Ion collisions

Electron-ion collisions are dominantly electrostatic in nature are therefore largely determined by the charge difference between electrons and ions and the electron to ion mass ratio. Consequently, one model can be applied that is valid for all monatomic propellants. These are computed using the classical formulae from [28].

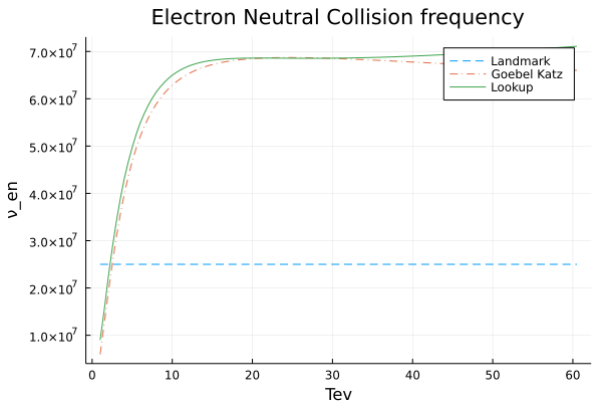

Figure 2.1: Comparison of Electron Neutral collision models with $n_n = 1e20$ [particles/m^3]

$$\nu_{ei} = 2.9 \times 10^{-6}\ Z^2 n_e T_e^{-3/2} \ln \Lambda. \tag{2.39}$$

Z is the ion charge state, n_e is the plasma density in m^{-3} and T_e is the electron temperature in eV. In the above expression, $\ln \Lambda$ is the well-known Coulomb logarithm, given by

$$\ln \Lambda = 23 - \frac{1}{2} \ln \left(10^{-6}\ Z^2 n_e T_e^{-3}\right) T_e < 10\ Z^2 \text{ eV} \tag{2.40}$$

$$\ln \Lambda = 24 - \frac{1}{2} \ln \left(10^{-6}\ n_e T_e^{-2}\right) T_e > 10\ Z^2 \text{ eV}. \tag{2.41}$$

For plasmas containing multiple charge states, the number-averaged charge state $\langle Z \rangle$ is computed and used in the above formula.

$$\langle Z \rangle \equiv \left(\sum_s Z_s n_s \right) / n_e \tag{2.42}$$

2.5 Anomalous collision frequency

Inserting the cumulative collision frequency from classical collisions alone into Equation 2.18, leads to an underpredicted electron transport by three to four orders of magnitude. [29] Most likely kinetic effects on small time- and lengthscales are responsible for the increased transport [16], however those microinstabilities cannot be resolved using a fluid approximation. In order to assimilate simulations closer with experimental results, an anomalous collision frequency has been introduced. The anomalous collision frequency aims to capture the physics not considered by the model and artificially increases the electron transport. Finding closure models for the anomalous collision frequency is considered the major challenge to achieve predictive Hall Thruster simulations.

The total momentum transfer collision frequency is described by Equation 2.34. The main goal of HallThruster.jl is to aid in finding new closure models. Currently, zero-equation (algebraic) and closure models employing a system of partial differential equations are available, however none thus far allow predictive Hall Thruster simulations. Models based on Bohm diffusion [30], wall effects [31] and turbulence [32] [33] have been proposed. Jorns presented a data-driven zero-equation model in [17]. In HallThruster.jl, zero equation closure models as a function of axial position are supported, and more sophisticated models can be implemented. The standard model is a Two-Zone Bohm model:

$$\nu_{AN} = \beta_1 \omega_{ce} \quad (z < L_{ch}) \tag{2.43}$$
$$\nu_{AN} = \beta_2 \omega_{ce} \quad (z \geq L_{ch}) \tag{2.44}$$

where ω_{ce} is the electron cyclotron frequency and L_{ch} is the length of the channel. As an example, in the Landmark benchmark [26], $\beta_1 = 1/160$ and $\beta_2 = 1/16$, while an additional frequency of 10^7 is added inside the channel to "account" for the walls. This model is plotted in Figure 2.2a against the axial position in a simulation using parameters detailed in Section 4.3. Figure B.1d shows the same two zone Bohm model with a slightly more realistic classical collision frequency profile with electron ion collisions taken into account. It is evident from these plots that the anomalous collision frequency is the dominant contribution to the electron momentum transfer collision frequency in this model, while classical collisions are relevant close to the anode. It should be noted that the two zone Bohm model is merely a simple approximation, and in no way should it be employed to draw general conclusions. In Chapter 5 another anomalous collision frequency model calibrated in [18] is presented.

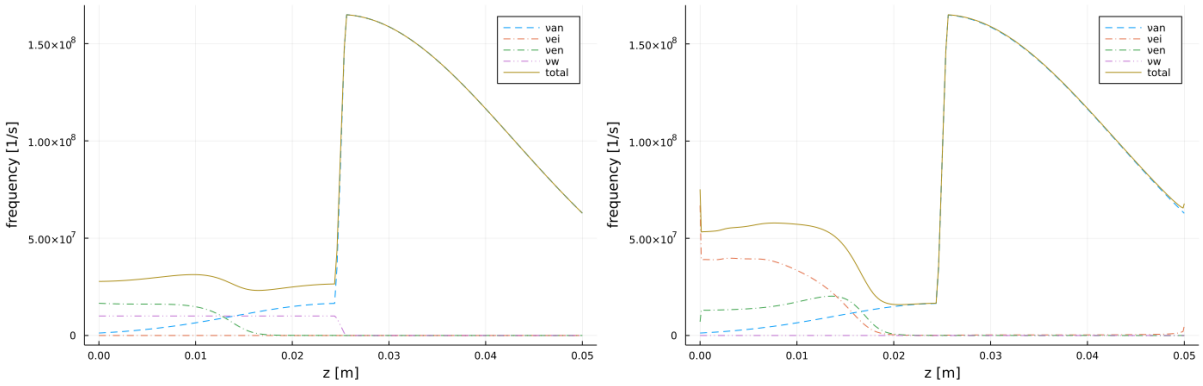

(a) (b)

Figure 2.2: The individual components of the momentum transfer collision frequency

2.6 Electron heat flux and energy loss terms

The electron energy governs the reactions and collisions in a Hall Thruster. This allows the electron energy heat flux and in particular the loss terms to wield strong influence over the simulation characteristics. As a result, an accurate electron energy profile enabled by consistent assumptions is of utmost importance. First, the Braginskii closure model adopted for the heat flux in the electron energy equation is discussed. Then, the terms encapsulated by the loss term in the energy equation are described. They consist of electron energy losses due to ionization and excitation as well as losses to the thruster walls.

$$S_{loss} = P_{ionization} + P_{excitation} + P_{wall} \tag{2.45}$$

Heat flux closure

Taking the second moment of the Vlasov equation, as done in Section 2.1 leads to a closure problem for the heat flux in Equation 2.12. Here, the Braginskii closure is employed. The standard two-Laguerre-polynomial Chapman-Enskog closure scheme is used, however the results are applied only to the field perpendicular electron heat conductivity. Braginskii [34] obtained electron and ion continuity, momentum and energy equations along with closures for the loss and source terms, examining both the magnetized and unmagnetized limit. As the electron larmor radius is much smaller than the characteristic length of

a thruster discharge channel, the magnetized limit for the electron heat flux is of interest. The closure is based on collision-induced random walk diffusion, employing the electron cyclotron radius $\rho_e = \frac{m_e v_{e,\perp}}{q|B|}$ as step-length and ν_e as frequency, consisting of the classical and anomalous electron collision frequency. This leads to factor $(\rho/l)^2$ lower conductivity in the in the perpendicular direction compared to the field aligned direction, for which the mean free path $l = \tau_e v_{t,e}$ is used as step-length. The heat diffusion is governed by a classical Fourier law.

$$q_{ez} = -\kappa_{e\perp} \nabla_\perp T_e \tag{2.46}$$

$$\kappa_{e\perp} \approx \frac{4.7 n_e T_e}{m_e \omega_{ce}^2 \tau_e} \tag{2.47}$$

$$\tau_e = 1/\nu_e = \frac{1}{\nu_{ei} + \nu_{en} + \nu_{ee} + \nu_{AN}} \tag{2.48}$$

where n_e is the electron density, T_e the electron temperature in electron Volts, m_e the electron mass, ω_{ce} the electron cyclotron frequency, and τ_e the electron collision time in seconds, which encapsulates the anomalous electron collision frequency treated in Section 2.5. The coefficient 4.7 changes slightly when multiple charges states Z are present, consequently it is a function an effective charge state Z_{eff}, which is obtained by Equation 2.42.

Ionization and excitation loss

Electron energy can be lost due to ionization of neutrals or ions to higher charge states or excitation of neutrals. The ionization and excitation rates $k_{ionization}, k_{excitation}$ modelled in Section 2.4 are simply divided by the known constant ionization and excitation energy $\Delta\epsilon_{ionization}, \Delta\epsilon_{excitation}$ of the propellant to obtain the ionization and excitation energy loss rate.

$$P_{ionization} = k_{ionization} \Delta\epsilon_{ionization} \tag{2.49}$$

$$P_{excitation} = k_{excitation} \Delta\epsilon_{excitation} \tag{2.50}$$

Wall loss model

In a Hall Thruster, energy will be lost to the thruster walls. Since HallThruster.jl is one-dimensional, this loss cannot be modelled directly but is taken into account as a source term in the electron energy equation Equation 2.16. Three different wall loss models are implemented. The first option is to ignore losses to the wall altogether. Secondly, a simple energy loss model assuming a constant sheath potential is available, and thirdly the sheath potential and loss coefficients can be computed based on a given wall material.

Constant Sheath Potential

This model employs a simple sheath energy loss model with constant sheath potential, based on the electron Boltzmann equation for electron density in the sheath as a function of electron temperature. Constants are set to scale losses inside and outside the thruster. [19] [26]

$$P_{wall} = \nu_{ew} n_e exp\left(\frac{\phi_s}{T_{ev}}\right) \tag{2.51}$$

where in the Landmark benchmark test case 2 $\nu_{ew} = 0.5 * 10^7$ [1/s] for $(x < L_{ch})$ and $\nu_{ew} = 10^7$ [1/s] for $(x > L_{ch})$ while the sheath potential is assumed a constant 20 [V].

Self-consistent sheath approximation

The higher fidelity wall sheath loss model is described in [7] and based upon findings by [35]. The fundamental assumption is that ion and electron currents to non-conductive walls have to be equal to prevent charge build-up.

$$I_{iw} = I_{ew}(1-\gamma) \tag{2.52}$$

where γ is the secondary electron yield. This is estimated from literature [36] [8] employing fit functions for wall materials, returning γ as a function of electron temperature. The supported wall materials are Alumina, Boron Nitride, Stainless steel and BN-SiO2. The sheath potential can then be estimated in the following.

$$\phi_s = -T_{ev} ln\left((1-\gamma)\sqrt{\frac{2m_i}{\pi m_e}}\right) \tag{2.53}$$

However the sheath exhibits a space charge limit once the secondary electron emission coefficient approaches unity, this slightly varies according to the propellant as a function of the ion to electron mass ratio.

$$\gamma_0 = 1 - 8.3\left(\frac{m_e}{m_i}\right)^{\frac{1}{2}} \tag{2.54}$$

[35] also found the space charge limited sheath potential ϕ_0 to scale linearly with the electron temperature, independent of propellant. The constant in Equation 2.55 was obtained in the limit of infinitely massive ions, and is therefore valid for all propellants in HallThruster.jl.

$$\phi_0 = -1.02\frac{kT_e}{e} \tag{2.55}$$

The power lost to the walls is then

$$P_{wall} = \frac{1}{4}\sqrt{\frac{8k_B T_{e,a}}{\pi m_e}} n_e exp\left(\frac{\phi_s}{T_{ev}}\right) 2T_{ev} \tag{2.56}$$

where the first part follows from the half Maxwellian approximation for electron velocity at the sheath boundary. The electron bulk velocity is neglected. The exponential term time electron density accounts for the electron density according to the Boltzmann relation Equation 2.63, while the 2 times electron temperature accounts for the energy deposited per electron hitting the wall. A comparison of the sheath potential according to different gases and the exponential term is given in Figure 2.3. It should be noted that the power losses in the LANDMARK model dwarf the Hobbs Wesson loss due to the the ratio of ν_{ew} over the twice the electron half Maxwellian speed. In the case of a magnetically shielded thruster, the electron temperature at the walls is assumed to be equal to the electron temperature at the anode. The model does not differentiate between axial positions inside and outside the thruster. The same loss model is applied over the entire domain. This approximation is justified when comparing to 2D simulations due to isothermal magnetic field lines.

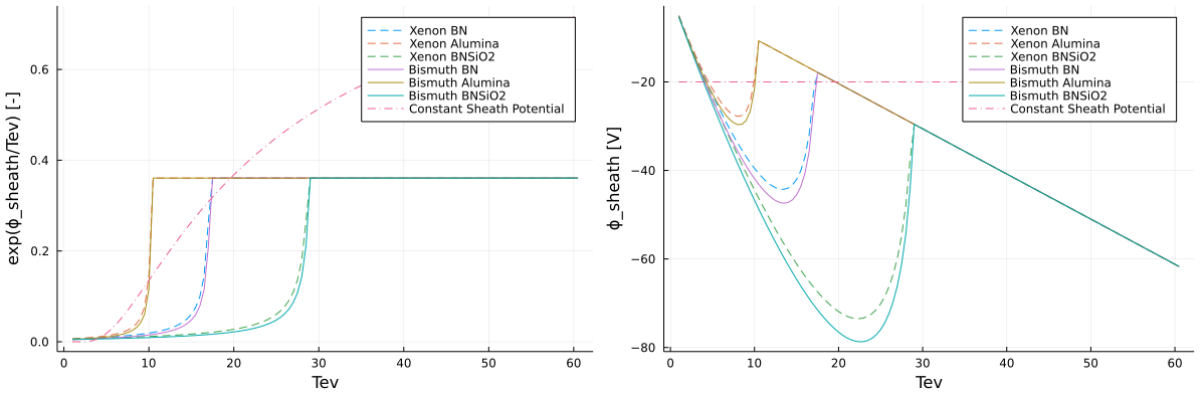

(a) (b)

Figure 2.3: Comparison of exponential term and sheath potential with different gases and wall materials

2.7 Presheath

Quasineutrality is assumed within the domain. However, this assumption breaks down close to surfaces at a potential different to the plasma potential, as charged particles are either attracted or repelled by the sheath. The nature of the sheath depends on the potential difference between the plasma and the surface. The sheath scale is on the order of a Debye length and is not modelled by HallThruster.jl. However in an effort to increase physical fidelity, the ions are forced to the negative Bohm velocity at the anode. This assumes a negatively biased sheath with respect to the plasma potential and results in the formation of a presheath. [24] In the following, it is shown how to arrive at the ion Bohm speed approximation. The potential differences $e\phi$ are assumed to be on the order of the electron temperature kT_e. Furthermore, assume that cold ions fall through an arbitrary potential of ϕ_0 while they move towards the wall. Through conservation of energy, their arrival velocity at the sheath edge can be related to the potential difference.

$$\frac{1}{2}m_i v_0^2 = e\phi_0 \tag{2.57}$$

Additionally, the ion flux during acceleration toward the wall is conserved.

$$n_i v = n_0 v_0 \tag{2.58}$$

The relation for ion velocity as a function of position in the sheath can be written as

$$\frac{1}{2}m_i v^2 = \frac{1}{2}m_i v_0^2 - e\phi(x) \tag{2.59}$$

Rewriting both Equation 2.57 and Equation 2.59 for v_0 and v, and dividing gives

$$\frac{v_0}{v} = \sqrt{\frac{\phi_0}{\phi_0 - \phi}} \tag{2.60}$$

which by applying flux conservation results in

$$n_i = n_0\sqrt{\frac{\phi_0}{\phi_0 - \phi}} \tag{2.61}$$

Close to the sheath edge Equation 2.61 can be expanded as a Taylor series, as ϕ is small compared to ϕ_0.

$$n_i = n_0 \left(1 - \frac{1}{2}\frac{\phi}{\phi_0} + ...\right) \tag{2.62}$$

In one dimension, neglecting collisions with other species and assuming isentropic temperature and pressure terms, no convection and no electron inertia, the electrons can be described by the Boltzmann relation Equation 2.63.

$$n_e = n_0 exp\left(\frac{e\phi}{kT_e}\right) \tag{2.63}$$

In this regime, the electron density is diffusion dominated and dictated by the electrostatic field. This assumption is generally valid along magnetic field lines and across weak magnetic fields with sufficient electron electron collisions. The Boltzmann relation can be expanded by assuming that the change in potential at the sheath edge is small compared to the electron temperature.

$$n_e = n_0 \left(1 - \frac{e\phi}{kT_e} + ...\right) \tag{2.64}$$

Taking Poisson's equation of the form

$$\nabla^2\phi = -\frac{e}{kTe_0}(n_i - n_e) \tag{2.65}$$

and substituting Equation 2.64 and Equation 2.62 leads after rearranging to

$$\nabla^2\phi = \frac{en_0\phi}{\epsilon_0}\left(\frac{1}{2\phi_0} - \frac{e}{kT_e}\right) \tag{2.66}$$

As the sheath is assumed to be ion attracting, it can by definition not slow or repell ions. As a result, the RHS of Equation 2.66 has to always be positive, which leads to the following requirement.

$$\phi_0 > \frac{kT_e}{2e} \tag{2.67}$$

By substituting Equation 2.57, the ion Bohm speed can be recovered. This condition is applied to the anode boundary and will be discussed in the boundary conditions.

$$v_0 > \sqrt{\frac{kT_e}{m_i}} \tag{2.68}$$

A consequence of this result is the formation of a presheath [37] [38], in which quasineutrality holds but the potential is adjusted to allow the ions to accelerate towards the sheath edge. This can lead to an entropy violation on the part of the Ohmic heating term $\mathbf{j} \cdot \mathbf{E}$ in the energy equation, which is discussed further in the context of simulation results in Subsection 4.3.1. Therefore, the currently implemented model is strictly speaking inconsistent.

2.8 Assumption validity in Hall thruster discharges

In this section, some of the key assumptions to arrive at the physical model described here are reiterated with their justification and impact mentioned.

- **One dimensional domain** This results in not being able to model inherently multidimensional fluid phenomena such as turbulence. Losses to the walls and expansion of plasma from the channel to the plume cannot be captured. Consequently, the model fidelity is reduced drastically.

- **Plasma as a fluid in a Hall Thruster discharge** It is assumed that a sufficient number of direct and electrostatic collisions take place to achieve a Maxwellian isentropic velocity distribution function of each species. In a real Hall Thruster discharge, this is definitely not the case. Approximating the neutrals as a fluid than for the charged species, since no coulomb collisions are able to reduce the neutral mean free path and thus thermalize the population. The approximation holds better for electrons and ions, however neither distribution will be fully isentropic nor Maxwellian.

- **Ideal gas law** The ion and electron pressure are evaluated using the ideal gas law. Assumes a Maxwellian distribution.

- **No ion losses to radial walls** An ok assumption to make for the short timescales considered here, since the ions on a large scale are not very energized. Ion losses are more important due to the erosion they cause rather than the energy being lost through them.

- **No ion to neutral momentum transfer** There will be some momentum transfer in reality. Including this contribution would require the neutrals to be modelled kinetically, as done in [13] for example. Modelling neutrals as a fluid with the Euler equations is not an option due to the long mean free path leading to a high Knudsen number, placing them in the molecular regime. Consequently modelling neutrals as monoenergetic simply using the continuity equation is a compromise. impact of neutral temperature on solo regime. [22]

- **No electron inertia** It can be argued that electron inertia is not relevant for the low frequency modes of interest in HallThruster.jl, since the electron timescales are very short. Neglecting eletron inertia leads to the QDD model. In Ref [21], Sahu et al. compared this to a 1D model employing non-neutral drift diffusion (NDD) and full fluid moment models, solving the full Euler equations for the electrons. The main difference between NDD and QDD in a time-averaged sense was found to be the ability to model a sheath at the anode due to the non-neutral assumption. The QDD model did however perform better when comparing global quantities, being only 0.5% off the FFM discharge current, while the NDD was 5% off.

- u_i**,** u_n **negligible in QDD** The electron thermal speed will be orders of magnitude higher than the ion bulk or thermal speeds due to the lower electron mass and higher energies.

- **Neglecting electron kinetic energy in energy equation** Generally over most of the domain, the contribution of the kinetic energy in the electron energy equation is negligible. However, the can change in the presheath region where the $\mathbf{j} \cdot \mathbf{E}$ loss term takes on negative values, which is unphysical. See Section 2.7 and Section 4.3.

- **Ions unmagnetized** A very valid assumption since the operating principle of a Hall thruster requires this in the first place. As long as realistic Hall thruster magnetic field profiles are simulated, the ion mass is sufficient to keep the Larmor radius much larger than the channel dimensions.

- **Isothermal ions** The ions remain cold throughout most of the domain, which supports the validity of isothermal ions. On the other hand, especially in the acceleration region, the ion velocity distribution function is highly energetic, which may be a result of the oscillating electric field. Roberts et al. [39] quantified this effect and showed that the ion temperature may reach 5eV. This temperature however was estimated by fitting a bi-maxwellian with heavy tails to the VDF, which technically calls the fluid assumption in HallThruster.jl into question.

- **Quasineutrality** Good assumption in a plasma with strong Debye shielding in general, but very strong electric fields might introduce regions of non-neutrality. This assumption can be tested using the Poisson equation. The strongest electric field is expected in the acceleration zone. One can assume a realistic value of maximum electric field $5 * 10^4$ V/m over a conservative distance of 0.5 cm. Plugging this into Equation 2.65 yields $n_i - n_e = 3e12\ m^{-3}$. Normalized by an average Hall thruster plasma density of $1e17\ -/\mathrm{m}^3$, results in $\frac{n_i - n_e}{n_0} = 2e - 5 \approx 0$. Quasineutrality therefore remains a valid approximation with Hall thruster typical electric fields.

2.9 Summary

To conclude, a 1D fluid model for application to Hall thruster discharges has been derived. Several different approximations have been presented for collision frequencies and loss term, while the formation of a presheath has been discussed. Next, the system of PDEs needs to be discretized and implemented computationally. The goal was to keep the model flexible and easily adaptive while making it as computationally efficient sa possible. This is covered in the next chapter.

Chapter 3

Implementation

This chapter provides an overview of the implementation of the equations. In Section 3.1, an overview of the code structure is presented. Section 3.3 dives into the numerical discretization and integration schemes. Challenges and properties of different numerical methods are shown.

The system of equations presented in the previous chapter has been discretized and implemented in the programming language Julia. The package DifferentialEquations.jl has been used for time integration of the heavy species (neutrals and ions). The equations were discretized on a one dimensional domain in space. The finite volume method was used mainly due to it being conservative by design, a good fit when solving a system of hyperbolic conservation laws. The fluxes appearing in this discretization have been approximated by different schemes including approximate Riemann solvers. A finite-difference approximation was used to solve the elliptic potential equation on a staggered grid to avoid odd-even decoupling. The code was developed together with PhD student Thomas Marks.

3.1 Global concept

The main requirement of the implementation is to facilitate simulations at low computational expense while allowing for a high degree of flexibility in terms of thrusters, propellants, domain sizes and choice of physical models for wall losses and collisional terms. The user has to provide a thruster geometry and magnetic field, which are both part of the Thruster object in HallThruster.jl. Additionally the neutral mass flow rate has to be fixed and boundary conditions need to be selected. The number of ionization states has to be set. The user can use preset initial conditions. Simulation parameters such as the simulation time, timestep (when setting a manual timestep) and number of cells has to be set as well. The user can either use the default physics models for collisions and losses, choose one of higher fidelity, or implement their own approximations. Theses choices are summarized in the *User defined* box in Figure 3.1. The loop in Figure 3.1, illustrates the computations in a single time step in HallThruster.jl. *Update timeinvariant* describes the evaluation of certain parameters. Note that the anomalous collision frequency is shown as a function of the magnetic field strength B, which does not necessarily have to be the case but seems to be an important parameter in current closure models. The vector $\mathbf{C}_{ano}$ can include other state, geometric, time-invariant or time-evolving plasma or other parameters. Having updated these properties, the elliptic equation for the potential is solved in *Solve potential*. Next, the electron momentum equation Equation 2.18 is solved for the electron velocity in *Electron momentum*. Having updated these values, the heavy species partial differential equations are propagated forward one step in time in *Fluid update*. The *Constants* box refers to lookup tables being used for ionization and excitation rates and loss terms to evaluate the source terms of the heavy species and the electron energy equation. The heavy species are integrated in time using DifferentialEquations.jl [40], while the electrons are integrated semi-implicitly using a Crank Nicolson scheme. The loop is repeated until the simulation comes to an end. The user can determine the interval at which the solution is to be saved and extract the quantities of interest. This is detailed further in Section 3.4.

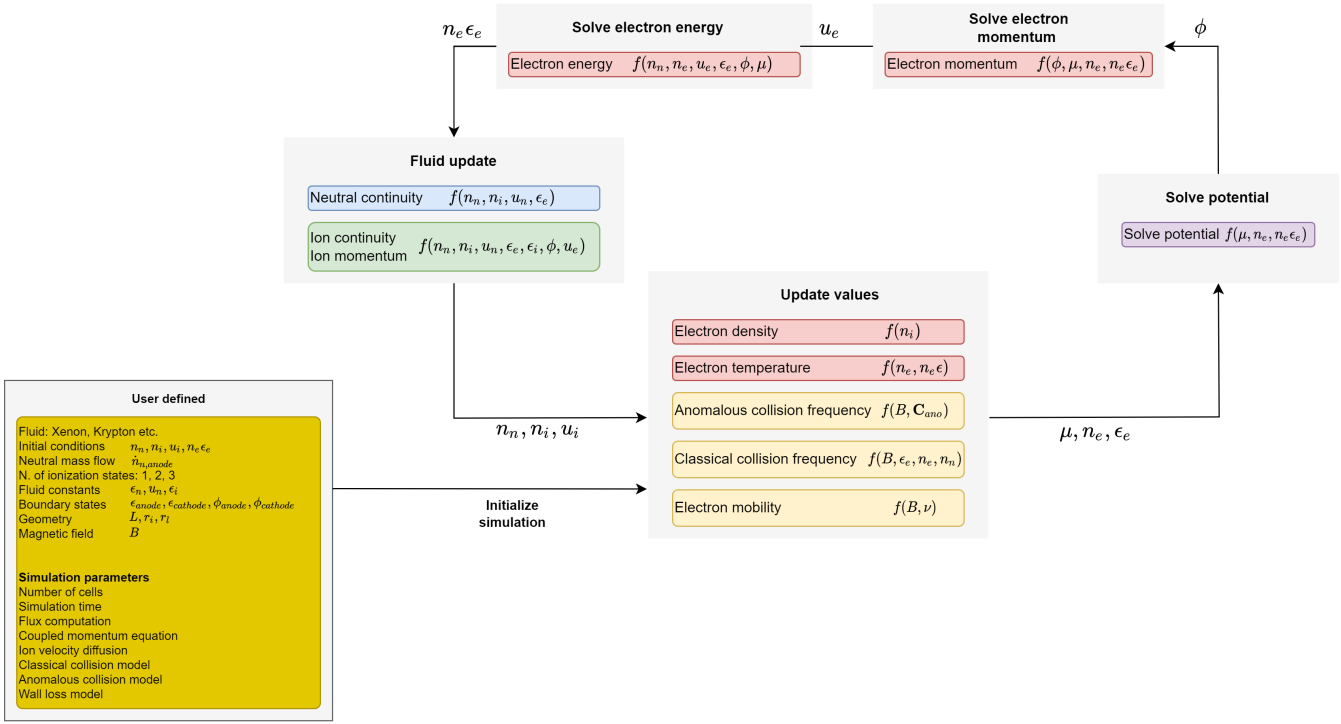

Figure 3.1: Flowchart illustrating the computations in HallThruster.jl

3.2 Julia

One of the main requirements of HallThruster.jl is a fast runtime. For this reason, the code was written in the programming language Julia. It is a dynamic high level language that has been compared to Python. Julia incorporates a multiple-dispatch architecture, which allows functions to execute different methods solely based on the type or number of arguments. This is different from classical object-oriented programming languages, in which dispatch is usually based only on the first argument. Multiple dispatch proved extremely useful in the implementation of the numerical method. For example, a flux function `Flux(U, ...)` can be defined differently depending whether `U` was of type `SVector{1}` or `SVector{2, T}`. In the first case, the `Flux(U, ...)` function returns the flux for a single advection equation, while in the second case the function evaluates the convection velocity and returns the two dimensional isothermal Euler flux. The performance penalty for the added flexibility is small as Julia uses Just in time compilation and type inference. The Julia compiler is more efficient than Python's interpreter. The developers claim that well written Julia code approaches the performance of C. On the downside, experience showed that initial compilation time is relatively long. As compilation only has to take place once, this does not negatively affect the overall time when simulating hundreds of discharges, but led to some wait time during code development.

3.3 Numerics

The finite volume method is used for spatial discretization and illustrated in Subsection 3.3.2. This transforms the PDEs into a system of ODEs as a function of time, which can be integrated by DifferentialEquations.jl. A constant grid size is used throughout the domain. Most of the implementation should make a generalization to a variable cell size easy, however this has not been tested intensively.

3.3.1 Schemes and flux computation

The finite volume methods has been chosen for its suitability to discretize hyperbolic conservation laws, as the discretization is conservative by design. Applying this approach to Equation 2.13 yields

$$\int_{i-\frac{1}{2}}^{i+\frac{1}{2}} \frac{\partial n_n}{\partial t}\, dz + \int_{i-\frac{1}{2}}^{i+\frac{1}{2}} \frac{\partial n_n u_n}{\partial z}\, dz = \int_{i-\frac{1}{2}}^{i+\frac{1}{2}} \dot{n}_n\, dz \tag{3.1}$$

This essentially corresponds to a control volume technique. The value within a cell is determine by the balance of incoming and outgoing fluxes. The $n_n u_n$ can be replaced by a generic flux term $F(z)$ and generalized to any advection like equation. The right hand side does not need to be considered further, as the term is taken care of in terms of a lookup table and is explained in **??**. Integration results in

$$h\frac{\partial n_n}{\partial t} + \left(F_{i+\frac{1}{2}} - F_{i-\frac{1}{2}}\right) = h\dot{n}_n \tag{3.2}$$

The fluxes $F_{i+\frac{1}{2}}$ and $F_{i-\frac{1}{2}}$ can be approximated by different schemes.

The classical Reconstruct, Evolve, Average (REA) algorithm [41] has been implemented to allow switching between different flux approximations. First, cell values are reconstructed at the cell edge. This leads to a left state `UL` and a right state `UR`. The standard reconstruction is piecewise constant, where the edge values correspond to the cell centered values. This leads to first order accurate spatial discretizations with all flux approximations, which are discussed later. In order to increase the spatial accuracy and reduce the smearing out of discontinuities, the discretizations can be augmented to second order of accuracy by piecewise linear reconstruction. In this case, the primitive variables are evaluated at the cell centers and then linearly reconstructed at the cell edge. There, the variables are converted back into the conservative form, as the flux approximations were implemented to take the conservative variables as input. The slope for reconstruction is determined by the gradient in the solution. In order to avoid spurious oscillations

and ensure the schemes are total variation-diminishing (TVD), limiters have to be used. This leads to a Godunov type scheme with MUSCL (Monotonic upstream-centered scheme for conservation laws) reconstruction. The averaging step in in REA algorithm can be omitted since HallThruster.jl uses a constant grid spacing and the average of the constant or linear slopes will thus always be the cell centered value anyways. Averaging will have to be added in case nonlinear reconstruction or variable grid spacing is applied.

Four different flux approximations have been implemented in HallThruster.jl. The upwind method is the simplest flux approximation suitable for hyperbolic conservation laws and simply advects information from either one side or the other in the control volume, depending on the sign of the velocity. Thus using the nomenclature introduced above, the upwind scheme merely considers either `UL` or `UR`. However, it can be shown by modified equation analysis that the method very diffusive. Additionally, the upwind method may not approximate physical systems well when information travels along different characteristic wave speeds, which is the case in hyperbolic conservation laws. Having two states in a problem governed by a conservation law, separated by a single discontinuity in the domain of, can the termed a Riemann problem. The solution of a Riemann problem contains shocks and rarefaction waves as characteristics. Therefore, in order to increase the fidelity of a flux approximation, a Riemann problem can be solved at a cell interface with the goal of including the physics of shock and rarefaction waves in the simulation. Riemann solvers thus take both `UL` and `UR` into account. In the interest of simplicity and low computational complexity, approximate rather than exact Riemann solvers were viewed as ideal. The global Lax-Friedrichs, local Lax-Friedrichs and HLLE approximate Riemann solver are presented in detail later in this section. Finally, a at best 5th order accurate weighted essentially non-oscillatory (WENO) scheme is implemented. In this case the fluxes are approximated taking adjacent fluxes into account. This scheme is 5th order only if the solution is sufficiently smooth.

Upwind

The simplest scheme is the upwind method. Its derivation by using Taylor expansion applied to the neutral continuity equation is illustrated in the following. Since the neutrals are merely modelled by the continuity equation, the axial velocity is constant over the entire domain and is assumed positive in the following. The fluxes in Equation 3.2 can be written as follows.

$$F_{i+\frac{1}{2}} = u n_{n_{i+\frac{1}{2}}} \tag{3.3}$$

$$F_{i-\frac{1}{2}} = u n_{n_{i-\frac{1}{2}}} \tag{3.4}$$

Next, the face values $n_{n_{i+\frac{1}{2}}}$ and $n_{n_{i-\frac{1}{2}}}$ need to be reconstructed. For $n_{n_{i+\frac{1}{2}}}$, a stencil where $l = -\frac{1}{2}$ and $r = -\frac{1}{2}$ is chosen.

$$n_{n_{i+\frac{1}{2}}} \approx w_{-\frac{1}{2}} \bar{n}_{n_i}$$

where the bar refers to cell average notation. $\bar{n}_{n_i} = n_{n_i} + \frac{h^2}{24} \frac{\partial^2 n_n}{\partial z^2}\big|_i + O(h^4)$. Due to the low order of accuracy the cell average notation can be dropped. Therefore

$$n_{n_i} = n_{n_{i+\frac{1}{2}}} - \frac{h}{2} \frac{\partial n_n}{\partial z}\bigg|_{i+\frac{1}{2}} + O(h^2)$$

Collecting terms leads to

$$n_{n_{i+\frac{1}{2}}} = (w_{-\frac{1}{2}}) n_{n_{i+\frac{1}{2}}} + (-w_{-\frac{1}{2}}) \frac{h}{2} \frac{\partial n_n}{\partial z}\bigg|_{i+\frac{1}{2}} + O(h^2)$$

Solving yields

$$w_{-\frac{1}{2}} = 1$$

$$n_{n_{i+\frac{1}{2}}} \approx 1 n_{n_i} \tag{3.5}$$

This is the first order accurate reconstruction of the face value at $i + \frac{1}{2}$. Applying the same method for the reconstruction at $i - \frac{1}{2}$ results in the upwind scheme.

$$\frac{\partial n_n}{\partial t} = -\frac{u_n}{h}\left(n_{n_i} - n_{n-1}\right) + \dot{n}_n \tag{3.6}$$

Following a similar method, the isothermal or full Euler equations can be discretized, using thermodynamic relations to evaluate velocity and temperature. Von-Neumann analysis with explicit time integration results in the well know CFL stability limit $\frac{u\Delta t}{\Delta x} < 1$ for this discretization. The critical timestep in HallThruster.jl is usually determined by transients in the ion fluids, as the continuity and momentum equations are solved and the ion velocity can reach values in excess of 20 km/s, depending on the applied potential. The upwind method is very diffusive and merely considers the one side of a given Riemann problem and therefore in fact does not solve a Riemann problem at all. As a result, wavespeeds in the solution are not considered at all. The following three approximate Riemann solvers were implemented to address this issue.

Global Lax-Friedrichs

The Global Lax-Friedrichs flux vector splitting (FVS) scheme is one of the simplest possible approximate Riemann solvers. Both states `UL` and `UR` are considered, and the flux is corrected by a factor containing the maximum wavespeed s_{max} in the entire system.

$$F_{i+\frac{1}{2}} = \frac{1}{2}(F_i + F_{i+1}) - \frac{1}{2} s_{max}(u_{i+1} - u_i) \tag{3.7}$$

$$s_{max} = \max_k |\lambda_k^{\pm}| \tag{3.8}$$

$$\lambda_k^{+-} = \frac{1}{2}(\lambda_k \pm |\lambda_k|) \tag{3.9}$$

where in this system the eigenvalues are $\lambda_1 = u$, $\lambda_2 = u + c$ and $\lambda_3 = u - c$.

As an example, the implementation of this flux is included below. Among other inputs, the function definition takes the conservative variables `UL` and `UR` as arguments. `NUM_CONSERVATIVE` is either 1, 2, or 3, depending whether the input is merely for the advection equation [ρ], isothermal Euler equations [ρ, ρu] or full Euler equations [ρ, ρu, ρE]. `velocity()` is a helper function to determine the advection velocity, constant in the case of the continuity equation, or $\frac{\rho u}{\rho}$ for the isothermal Euler equations. The electron pressure on either side is evaluated and used in case the electron pressure coupled method is applied, see Subsection 3.3.7. `charge_factor` is evaluated for the same reason. Finally the flux on both the left and right sides are evaluated, resulting in [ρu] for the advection equation or [$\rho u, \rho u * u + p + pe$] for the isothermal Euler equations, where pe again is a relict of the electron-pressure coupled method. The flux at the edge is the computed according to the global Lax-Friedrichs FVS outlined above. `lambda_global` corresponds to s_{max} in Equation 3.7. The maximum wavespeed is computed before iterating through the domain to reduce computational expense and fed to the `global_lax_friedrichs()` function.

```
function global_lax_friedrichs(UL::SVector{$NUM_CONSERVATIVE, T}, UR::SVector{$NUM_CONSERVATIVE,
T}, fluid, coupled = false, TeL = 0.0, TeR = 0.0, neL = 1.0,
neR = 1.0, lambda_global = 0.0, args...) where T
    Z = fluid.species.Z
```

```
    uL = velocity(UL, fluid)
    uR = velocity(UR, fluid)

    peL = TeL * neL
    peR = TeR * neR

    charge_factor = Z * e * coupled

    FL = flux(UL, fluid, charge_factor * peL)
    FR = flux(UR, fluid, charge_factor * peR)

    return @SVector[
        0.5 * (FL[j] + FR[j]) + 0.5*lambda_global*UL[j] - 0.5*lambda_global*UR[j]
        for j in 1:$(NUM_CONSERVATIVE)]
end
```

Local Lax-Friedrichs

This flux vector splitting scheme is of similar form to the global Lax-Friedrichs scheme discussed before. Equation 3.7 is still valid, with the distinction that s_{max} is now the maximum local wavespeed in the place of the maximum global wavespeed. The local Lax-Friedrichs flux is also known as the Rusanov flux. [42] The flux remains very dissipative, which can however be desireable for the applications of HallThruster.jl to dampen some high frequency discharge current oscillations.

$$s_{max} = \max(s_{i+1,max}, s_{i,max}) \tag{3.10}$$
$$s_{i+1,max} = \max(|u_{i+1} - c_{i+1}|, |u_{i+1} + c_{i+1}|) \tag{3.11}$$
$$s_{i,max} = \max(|u_i - c_i|, |u_i + c_i|) \tag{3.12}$$

One of the advantages of this flux is its simplicity and consequently low computational complexity, while increasing fidelity compared to the global Lax Friedrichs scheme. Note that this scheme will reduce to the global Lax-Friedrichs scheme unless the electron pressure coupled method is applied, since the sonic speed will be constant throughout the domain as the neither the ion nor neutral temperatures change.

HLLE

The Harten Lax van-Leer Einfeldt flux is an approximate Riemann solver first proposed by [43]. A numerical approximation of the largest and smallest signal velocities is computed, omitting the need to estimate the primitive variables in a Riemann problem. The resulting flux is computed as follows.

$$F_{i+\frac{1}{2}} = \frac{1}{2}(F_i + F_{i+1}) - \frac{1}{2}\frac{s_{max} + s_{min}}{s_{max} - s_{min}}(F_i - F_{i+1}) + \frac{s_{max}s_{min}}{s_{max} - s_{min}}(u_{i+1} - u_i) \tag{3.13}$$

where

$$s_{min} = \min(s_{i,min}, s_{i+1,min}) \tag{3.14}$$
$$s_{max} = \max(s_{i,max}, s_{i+1,max}) \tag{3.15}$$
$$s_{i,min} = \min(0, u_i - c_i) \tag{3.16}$$
$$s_{i+1,min} = \min(0, u_{i+1} - c_{i+1}) \tag{3.17}$$
$$s_{i,max} = \max(0, u_i + c_i) \tag{3.18}$$
$$s_{i+1,max} = \max(0, u_{i+1} + c_{i+1}) \tag{3.19}$$
$$\tag{3.20}$$

The HLLE flux is thus a three state solver. The signal velocities are evaluated using the bulk velocity and the local speeds of sound. The speed of sound is obtained through thermodynamic relations. The flux is relatively dissipative and smears out near discontinuities, but still offers higher fidelity than the Lax-Friedrichs scheme due to advection the solution at two rather than one signal velocity.

Second order TVD schemes

The Godunov type schemes described above are at most first order accurate, even if the applied Riemann solver itself was exact. The order of accuracy can be extended to second order by employing piecewise linear reconstruction in the reconstruction step of REA. First, the primitive variables at the cell centers and one cell before and after are computed. Then, the gradients on both sides of the solution are determined using the primitive variables. These are $\nabla U_+ = U_{i+1} - U_i$ and $\nabla U_- = U_i - U_{i-1}$. The solution is then reconstructed on the cell face by $U_{i+\frac{1}{2}} = U_i + \frac{1}{2}\nabla U_+$, where the factor $\frac{1}{2}$ can be used since the cell size is constant. Applying this form of reconstruction would lead to spurious oscillations and a scheme that is not total-variation diminishing (TVD). To alleviate this problem, slope limiters $\phi(r)$ are introduced. The limiters are informed by the ratio of the gradients $r = \frac{U_+}{U_-}$. The linear reconstruction step then takes the form $U_{i+\frac{1}{2}} = U_i + \frac{1}{2}\phi(r)\nabla U_+$. A wide array of limiters have been proposed that lie within the TVD regions, the ones implemented in HallThruster.jl are the following.

$$\text{Minmod} \quad \phi(r) = \max(0, \min(1, r)) \tag{3.21}$$
$$\text{Koren} \quad \phi(r) = \max(0, \min(2r, \min\left(\frac{1+2r}{3}, 2\right))) \tag{3.22}$$
$$\text{Superbee} \quad \phi(r) = \max(0, \min(2r, 1), \min(r, 2)) \tag{3.23}$$
$$\text{van Leer} \quad \phi(r) = \frac{r + |r|}{1 + |r|} \tag{3.24}$$
$$\text{van Albada} \quad \phi(r) = \frac{r^2 + r}{r^2 + 1} \tag{3.25}$$
$$\text{Osher} \quad \phi(r) = \frac{r^2 + r}{r^2 + 1} \tag{3.26}$$

It was found experimentally in Section 4.2 that only the Osher and van Albada limiters lead to non-oscillatory results in practice with all flux schemes. The van Leer limiter is stable with the local and global Lax Friedrichs flux scheme. Ref. [21] also used MUSCL reconstruction coupled with Global Lax Friedrichs Flux Vector Splitting for fluid models of low temperature magnetized plasma discharges and compared various limiters for symmetry and the ability to obtain smooth profiles on shock tube problems. They conclude by recommending the van Leer limiter.

WENO

As the schemes described thus far have a maximum order of accuracy of 2, it has been attempted to implement a weighted essentially non-oscillatory 5th order scheme. This scheme is 5th order if the solution

is sufficiently smooth [44]. The essentially non-oscillatory idea is similar to a MUSCL reconstruction, but using interpolation over a stencil rather than linear reconstruction. A weighted essentially non-oscillatory scheme then uses a linear combination of smaller stencils to add up to a higher-order stencil. Below, w_i are the final weights that add up to one, and β_k are the smoothness indicators. ϵ is chosen to be 10^{-6} to stop the denominator from going to 0. The linear weights are $\gamma_1 = 0.1, \gamma_2 = 0.6, \gamma_3 = 0.3$. See reference [45] for more details.

$$F_{i+\frac{1}{2}} = w_1 F^{(1)}_{i+\frac{1}{2}} + w_2 F^{(2)}_{i+\frac{1}{2}} + w_3 F^{(3)}_{i+\frac{1}{2}} \tag{3.27}$$

where

$$F^{(1)}_{i+\frac{1}{2}} = \frac{1}{3}F_{i-2} - \frac{7}{6}F_{i-1} + \frac{11}{6}F_i \tag{3.28}$$

$$F^{(2)}_{i+\frac{1}{2}} = -\frac{1}{6}F_{i-1} + \frac{5}{6}F_i + \frac{1}{3}F_{i+1} \tag{3.29}$$

$$F^{(3)}_{i+\frac{1}{2}} = \frac{1}{3}F_i + \frac{5}{6}F_{i+1} - \frac{1}{6}F_{i+2} \tag{3.30}$$

$$w_i = \frac{\tilde{w}_i}{\sum_{k=1}^{3} \tilde{w}_k} \tag{3.31}$$

$$\tilde{w}_k = \frac{\gamma_k}{(\epsilon + \beta_k)^2} \tag{3.32}$$

$$\beta_1 = \frac{13}{12}(F_{i-2} - 2F_{i-1} + F_i)^2 + \frac{1}{4}(F_{i-2} - 4F_{i-1} + 3F_i)^2 \tag{3.33}$$

$$\beta_2 = \frac{13}{12}(F_{i-1} - 2F_i + F_{i+1})^2 + \frac{1}{4}(F_{i-1} - F_{i+1})^2 \tag{3.34}$$

$$\beta_3 = \frac{13}{12}(F_i - 2F_{i+1} + F_{i+2})^2 + \frac{1}{4}(3F_i - 4F_{i+1} + F_{i+2})^2 \tag{3.35}$$

The scheme is implemented in the domain and can be coupled with any of the previously described flux schemes. However, different biased stencils are required in close to the boundaries. This has not been done yet, and is required for the scheme to actually increase fidelity.

3.3.2 Ions and neutrals

The ions and neutrals are discretized using one of the schemes described in the previous section. Thermodynamic relations are used to evaluate the speed of sound, which is constant for both neutrals and ions due to constant temperature. The ion pressure changes as a function of ion density. The reader is referred to the documentation and code base on Github to look at the actual implementation in Julia. [23]

$$c = \sqrt{\gamma R_{specific} T} \tag{3.36}$$

$$p = n k_B T \tag{3.37}$$

The electric field in the acceleration source term in the ion momentum equation is obtained by finite differences. The general finite difference approach adopted to evaluate derivatives numerically in HallThruster.jl is described in Subsection 3.3.8.

3.3.3 Potential

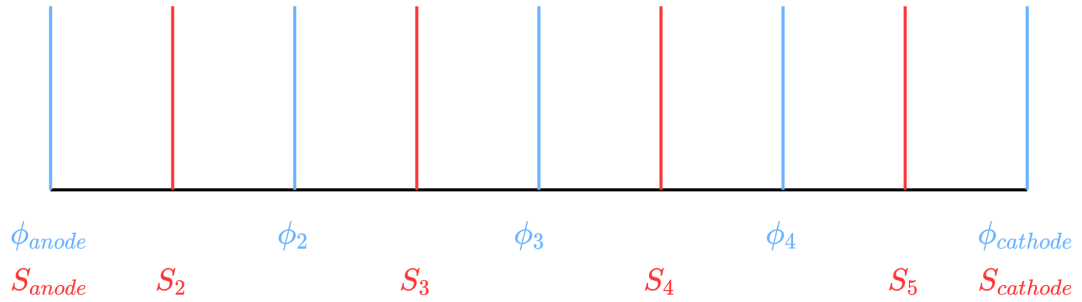

Figure 3.2: Staggered grid showing FVM cell centers in red and the potential discretization on the edges

In this model, the potential can be seen as an analog to the pressure in incompressible fluid simulations, both being governed by elliptic equations with infinite information propagation speed. Consequently, similar issues as in incompressible Navier-Stokes simulations arise. A staggered grid, illustrated in Figure 3.2, is employed to prevent odd-even decoupling and also eliminates the need for interpolation to a large extent. The potential is discretized using a second order centered difference scheme, with all derivatives appearing approximated in a similar fashion. The tridiagonal system $\underline{\underline{A}}\underline{x} = \underline{b}$ is then solved. The left hand side of Equation 2.25 is discretized as follows, the indexing refers to the fluid discretization.

$$\frac{\partial}{\partial z}\left(\mu_\perp n_e \frac{\partial \phi}{\partial z}\right)\Bigg|_{i+\frac{1}{2}}^{\delta} \approx \frac{1}{h}\left(\left(\mu_\perp|_{i+1}^{\delta} n_e|_{i+1}^{\delta} \frac{\partial \phi}{\partial z}\Bigg|_{i+1}^{\delta}\right) - \left(\mu_\perp|_{i}^{\delta} n_e|_{i}^{\delta} \frac{\partial \phi}{\partial z}\Bigg|_{i}^{\delta}\right)\right) + O(h^2) \tag{3.38}$$

where

$$\frac{\partial \phi}{\partial z}\Bigg|_{i+1}^{\delta} \approx \frac{1}{h}\left(\phi_{i+\frac{3}{2}} - \phi_{i+\frac{1}{2}}\right) + O(h^2) \tag{3.39}$$

similarly

$$\frac{\partial \phi}{\partial z}\Bigg|_{i}^{\delta} \approx \frac{1}{h}\left(\phi_{i+\frac{1}{2}} - \phi_{i-\frac{1}{2}}\right) + O(h^2) \tag{3.40}$$

results in

$$\frac{\partial}{\partial z}\left(\mu_\perp n_e \frac{\partial \phi}{\partial z}\right)\Bigg|_{i}^{\delta} \approx \frac{1}{h^2}\left(\mu_\perp|_{i+1}^{\delta} n_e|_{i+1}^{\delta} \phi_{i+\frac{3}{2}} - (\mu_\perp|_{i+1}^{\delta} n_e|_{i+1}^{\delta} + \mu_\perp|_{i}^{\delta} n_e|_{i}^{\delta})\phi_{i+\frac{1}{2}} + \mu_\perp|_{i}^{\delta} n_e|_{i}^{\delta} \phi_{i-\frac{1}{2}}\right) + O(h^2) \tag{3.41}$$

The right hand side of Equation 2.25 follows a similar procedure. The left hand side is incorporated into a NxN matrix A, while the RHS is added to the vector b and $N = n_{cells} + 1$. This results in a tridiagonal matrix that is diagonally dominant, and can therefore be solved using the Thomas algorithm at a computational expense of O(N), rather than O(N^3) for standard Gaussian elimination. A very strong numerical derivative in the electron density or electron mobility, for example caused by a discontinuity, may lead to a matrix that is not diagonally dominant. In this case, the Thomas algorithm would fail. Dirichlet boundaries are employed on both sides. The boundary cells are coincident with the domain boundaries and Dirichlet conditions are applied. The implementation was verified using the method of manufactured solutions, corresponding plots can be inspected in Chapter 4.

3.3.4 Electrons

When integrated explicitly, the diffusive term in the energy equation, governed by the magnitude of the heat flux q_{ez}, introduces severe timestep restrictions arising from von Neumann stability analysis. [20] Consequently, the fluxes of the electron energy equation are treated implicitly or semi-implicitly to circumvent the explicit stability limit, while the source terms are treated explicitly. This reduces the computational complexity. The gradients required for the computation are approximated using second order finite difference. The electron velocity follows from the generalized Ohm's law. The left hand side of Equation 2.16 can be rewritten by applying product rule.

$$\frac{\partial}{\partial t}\left(\frac{3}{2}n_e k_B T_e\right)+\frac{\partial}{\partial z}\left(\frac{5}{2}n_e k_B T_e u_{ez}\right)+\frac{10}{9}\left(\frac{\partial}{\partial z}\left(\mu n_e k_B T_e\right)\frac{\partial}{\partial z}\left(\frac{3}{2}k_B T_e\right)+\mu n_e k_B T_e \frac{\partial^2}{\partial z^2}\left(\frac{3}{2}k_B T_e\right)\right) = RHS \tag{3.42}$$

The advective term is discretized as described before on the neutral continuity equation, using an upwind scheme, changing advection direction according to the electron velocity. No approximate Riemann solver is applied here. The first part of the diffusive term in approximated in a similar manner, as a product of 2 first derivative approximations. The last term containing the second derivative is discretized as follows.

$$\mu n_e k_B T_e \int_{i-\frac{1}{2}}^{i+\frac{1}{2}} \frac{\partial^2}{\partial z^2}\left(\frac{3}{2}k_B T_e\right) dz = \mu n_e k_B T_e|_i \left(\frac{\partial \frac{3}{2}k_B T_e}{\partial z}\bigg|_{i+\frac{1}{2}} - \frac{\partial \frac{3}{2}k_B T_e}{\partial z}\bigg|_{i-\frac{1}{2}}\right) \tag{3.43}$$

The derivative needs to be reconstructed on the face, a stencil where $l = -\frac{1}{2}$ and $r = \frac{1}{2}$ is chosen.

$$\frac{\partial \frac{3}{2}k_B T_e}{\partial z}\bigg|_{i+\frac{1}{2}}^{\delta} \approx w_{-\frac{1}{2}}\left(\frac{3}{2}k_B \bar{T_e}\right)\Big|_i + w_{\frac{1}{2}}\left(\frac{3}{2}k_B \bar{T_e}\right)\Big|_{i+1} \tag{3.44}$$

Due to the low order of accuracy the cell average notation can be dropped, since the approximation of the cell average $\frac{3}{2}k_B\bar{T_e}|_i = \frac{3}{2}k_B T_e|_i + \frac{h^2}{24}\frac{\partial^2 \frac{3}{2}k_B T_e}{\partial z^2}\big|_i + O(h^4)$ becomes irrelevant.

$$\frac{\partial \frac{3}{2}k_B T_e}{\partial x}\bigg|_{i+\frac{1}{2}}^{\delta} = w_{-\frac{1}{2}}\frac{3}{2}k_B T_e|_i + w_{\frac{1}{2}}\frac{3}{2}k_B T_e|_{i+1} + \frac{h^2}{24}\left(w_{-\frac{1}{2}}\frac{\partial^2 \frac{3}{2}k_B T_e}{\partial z^2}\bigg|_i + w_{\frac{1}{2}}\frac{\partial^2 \frac{3}{2}k_B T_e}{\partial z^2}\bigg|_{i+1}\right) + ...$$

$$\frac{3}{2}k_B T_e|_i = \frac{3}{2}k_B T_e|_{i+\frac{1}{2}} - \frac{h}{2}\frac{\partial \frac{3}{2}k_B T_e}{\partial z}\bigg|_{i+\frac{1}{2}} + O(h^2)$$

$$\frac{3}{2}k_B T_e|_{i+1} = \frac{3}{2}k_B T_e|_{i+\frac{1}{2}} + \frac{h}{2}\frac{\partial \frac{3}{2}k_B T_e}{\partial z}\bigg|_{i+\frac{1}{2}} + O(h^2)$$

Collecting terms and solving for $w_{-\frac{1}{2}}$ and $w_{\frac{1}{2}}$ results in

$$w_{-\frac{1}{2}} = -\frac{1}{h} \text{ and } w_{\frac{1}{2}} = \frac{1}{h}$$

$$\frac{\partial \frac{3}{2}k_B T_e}{\partial z}\bigg|_{i+\frac{1}{2}}^{\delta} \approx \frac{1}{h}\left(\frac{3}{2}k_B T_e|_{i+1} - \frac{3}{2}k_B T_e|_i\right) \tag{3.45}$$

Applying the same analysis to the other derivative results in the following discretization, which is second order accurate in space. Even though a finite volume approach was used here, the result is equivalent to a second order finite difference approximation.

$$\mu n_e k_B T_e \frac{\partial^2}{\partial z^2}\left(\frac{3}{2}k_B T_e\right)\Big|_i^{\delta} \approx \mu n_e k_B T_e|_i \frac{1}{h^2}\left(\frac{3}{2}k_B T_e|_{i+1} - 3k_B T_e|_i + \frac{3}{2}k_B T_e|_{i-1}\right) \tag{3.46}$$

Propagation in time has been implemented as a linear combination between explicit and implicit $U_i^{n+1} = U_i^n + \Delta t(1-c_t)U_i^n + c_t \Delta t U_i^{n+1}$. Setting c_t to 0.5 yields the Crank-Nicholson method, while setting it to 1 makes the method fully implicit. The problem can be written in form of a tridiagonal matrix problem $\underline{\underline{A}}\underline{x} = \underline{b}$, which just like the potential previously can be solved efficiently by the Thomas algorithm. The solver has been implemented in HallThruster.jl by PhD student Thomas Marks.

3.3.5 Boundary conditions

The fluid equations are hyperbolic conservation laws, and as such boundary conditions need to be specified. The neutral mass is determined by the neutral mass flow into the domain and recombination of ions hitting the anode. It is assumed that all ions hitting the anode come back into the domain as neutrals, see Equation 3.47.

$$n_{n,anode} = \frac{\dot{n}_{n,inflow}}{A_{ch} m_i u_n} + \frac{\Gamma_{i,anode}}{u_n} \tag{3.47}$$

where A_{ch} is the channel cross sectional area and m_i the ion $\approx$ neutral mass with $\Gamma_{i,anode}$ the ion flux towards the anode. In the simple boundary condition model, the ion velocity is forced to be at least the ion Bohm velocity, with the ion density changing according to flux conservation, see Section 2.7. This corresponds to forcing the sheath to be ion attracting and leads to the formation of a presheath, where the electric field takes on negative values to allow the ions to be accelerated towards the anode. This can lead to non-physical electron energy Ohmic heating as currently employed in Equation 2.16. The Ohmic heating term would eventually become a loss term. It is recommended to implement higher fidelity anode sheath model that allows the sheath potential to evolve from ion attracting towards ion repelling. The electron energy is fixed to certain values at both anode and cathode in the Landmark study. Note that the internal energy ϵ and not the product ϵn_e is specified, which is the conserved variable in the Equation 2.16. Another option is to let the electron energy float at the anode, which would be a more realistic assumption. However, this requires a higher fidelity sheath model. Dirichlet boundary conditions are applied for the potential at both domain ends. Ghost cells are used to enforce the boundary conditions for the fluid equations.

3.3.6 Integration in time

After performing the spatial discretization and setting up a system of ODEs, the solution has to be propagated in time. Time marching for the heavy species is performed using the algorithms provided by DifferentialEquations.jl. The second order strong stability preserving Runge-Kutta (SSPRK22) scheme was chosen as standard for its robustness. It guarantees monotonicity (or strong stability) $||\mathbf{u}^{n+1}|| \leq ||\mathbf{u}^n||$, which is crucial in nonlinear hyperbolic conservation laws, as discontinuities can cause non-physical oscillations. The package does include options for automated timestepping, which evaluates scaled error estimates to decide whether to accept or reject a certain timestep. This has been disabled, since the electrons are integrated separately, either with a Crank-Nicolson method or fully implicitly. A constant timestep therefore allows the two systems to be evaluated separately. Performing von-Neumann analysis on the advection equation with forward Euler time integration yields the well known CFL number $\sigma = u\frac{\Delta t}{\Delta x}$. The SSPRK22 method can be rearranged as a convex combination of forward Euler steps, yielding a stability limit of $\sigma < 1$, just like the Euler method itself. In order to set the timestep in HallThruster.jl, the maximum signal velocity of the selected flux scheme is estimated. All implemented flux schemes use $s_{max} = max(|c_s + u|, |c_s - u|)$, where the sound speed can be computed through $c_s = \sqrt{\gamma k_B T / m_i}$. The maximum expected ion velocity can be easily estimated using conservation of energy $\frac{1}{2} m_i u_i^2 = qU$, where U is the applied potential difference. As the ions are assumed isothermal, the sonic speed does not change throughout the domain, unless the electron pressure coupled method is applied, see Subsection 3.3.7.

3.3.7 Electron pressure coupled method

Here, a solution to the numerical oscillations around 0 ion velocity is presented. These oscillations are similar to incompressibility limit issues arising at low Mach numbers when solving the compressible Navier-Stokes equations. As the electron pressure depends on the ion density due to quasineutrality, the electric field depends on the ion density. As a result, the electron pressure is nonlinearly coupled to the ion momentum, which causes numerical oscillations when ion velocity becomes very low. Equation 2.18 can be rewritten in the following assuming only one charge state. The electron pressure coupled method has only been implemented for singly charged ions, the charge state is therefore omitted in the following.

$$E = \frac{-u_e}{\mu} - \frac{1}{en_i}\nabla(n_i k_B T_e) \tag{3.48}$$

Substituting Equation 3.48 into the ion momentum equation Equation 2.15 results in

$$\frac{\partial}{\partial t}(n_i u_i) + \frac{\partial}{\partial z}(n_i u_i^2 + \frac{p_i}{m_i}) = \frac{e}{m_i}\left(n_i \frac{-u_e}{\mu} - \frac{1}{en_i}\nabla(n_i k_B T_e)\right) \tag{3.49}$$

and can be rearranged into

$$\frac{\partial}{\partial t}(n_i u_i) + \frac{\partial}{\partial z}(n_i u_i^2 + \frac{p_i + p_e}{m_i}) = \frac{-en_i u_e}{m_i \mu} \tag{3.50}$$

This method was first proposed by Hara [11]. Here, the electron pressure is directly coupled to the ion momentum, which eliminates the numerical oscillations. In case the gradient in the electron pressure is negligible, the electric field is recovered. The method also changes the ion sound speed from the ion thermal to the ion acoustic speed, thereby decreasing the range of Mach numbers covered in the simulation domain.

3.3.8 Other approximations

The derivatives appearing in the source terms of the fluid equations and the generalized Ohm's law have been discretized by standard second order finite differences. At the around the thruster exit area, commonly used anomalous collision frequency models exhibit strong discontinuities an order of magnitude. Similar discontinuities may appear in the energy loss terms, for example in the Landmark study. These discontinuities can introduce numerical oscillations, and led to the community to adopt smoothed out profiles. The discontinuities in HallThruster.jl are either smoothed by linear or quadratic approximations over a defined length interval.

3.4 Postprocessing

Postprocessing functions have been implemented to relate simulation results to Hall Thruster quantities of interest. The thrust is estimated from the ion fluxes out of the domain, and the discharge current can be computed as a function of the electron and ion currents, possibly multiple ion fluids. A fast fourier transform to inspect the discharge current in the frequency domain was added. As Hall Thrusters are highly oscillatory devices, time-averaged results are of interest. A function accommodating the solution object and averaging the fluid properties has been added to HallThruster.jl.

3.5 Documentation

The code is hosted on the Github page of the Plasmadynamics and Electric Propulsion Laboratory of the University of Michigan. [23]. A documentation has been added using the package Documenter.jl.

It contains a review of the physics model and provides an overview of the different options. The documentation should be sufficiently extensive to allow users to generate results, even with little experience in computational fluid dynamics or plasma physics. A short Jupyter notebook tutorial guides new users through an example simulation. Most functions and methods have comments that were added to provide an explanation of the purpose and application.

Chapter 4

Verification & Discussion

Verification is critical to any simulation. It serves the purpose to gain confidence that the code is actually computing what was intended. The HallThruster.jl verification strategy rests on three pillars. In Section 4.1 the output of implemented functions is compared to the expected values by employing unit tests. In order to verify the spatial discretization of the differential equations, order verification studies using the method of manufactured solutions are presented in Section 4.2. Finally, the results are compared to the Landmark 1D fluid model benchmark and to results obtained by [22] in Section 4.3 [26]. The LANDMARK model solves similar equations to HallThruster.jl and with using the same ionization and collision model, the results should agree.

4.1 Unit tests

Extensive unit testing has been implemented to help in searching for bugs. Currently 78% of the code used for generating simulations, which excludes plotting and postprocessing, is covered by unit tests. The standard implementation is to use functions defined in HallThruster.jl and compare their output to the expected output, which is calculated manually. Provided exact agreement for integers and strings, or sufficiently close agreement for floating point numbers, the tests pass. Test are also checking that functions output the correct type or size of an array. This is important as Julia's multiple dispatch architecture allows to define functions with many different methods. An example is included below. Unit tests are automated in a testing module and can be run anytime to verify new code additions do not cause new bugs. This has been implemented using the Julia testing module.

```
#global_lax_friedrichs
@test global_lax_friedrichs(continuity_state, continuity...) == flux(continuity...)
@test global_lax_friedrichs(isothermal_state, isothermal...) == flux(isothermal...)
@test global_lax_friedrichs(euler_state, euler...) == flux(euler...)
```

4.2 Order verification studies

The method of manufactured solution has has been applied to verify the correct implementation of the spatial discretization. The expected orders of accuracy from Taylor expansions are compared to the actual orders of convergence by successively refining the grid and investigating the evolution of the error. As the name suggests, the solution is forced to a manufactured solution. Candidate functions should be bounded, smooth, not display any asymptotes and are ideally periodic. These properties make the trigonometric functions ideal candidates. The solution is then substituted into the differential equation. As an illustration, the manufacured solution of the form $n_{man} = c + Acos(kz + \phi)$ is chosen **also what about source terms**, where c is the base value, A the amplitude of the cos, $k = \frac{2\pi n}{L}$, n is the wavenumber, L the domain length and ϕ a phase shift. The wavenumber should be more than two times smaller than the number of grid cells to avoid aliasing effects. Applying this to the neutral continuity Equation 2.13 by replacing it for the neutral number density and neglecting the ionization source term, yields the following

$$\left(\frac{\partial}{\partial t} + u_n \frac{\partial}{\partial z}\right) n_{man} = 0 - u_n k A sin(kz + \phi) \tag{4.1}$$

The constant c disappears when taking derivatives. Dirichlet boundary conditions are applied at the inflow and the boundary states have to correspond to the value of the manufactured solution at $z = 0$. When applying the upwind method and simple forward (explicit) Euler marching, Equation 4.2, the discretization leads to the following.

$$n_n^{n+1} = n_n^n + \Delta t \frac{\partial n_n}{\partial t}\bigg|^n + \cancel{\frac{1}{2}(\Delta t)^2 \frac{\partial^2 n_n}{\partial t^2}\bigg|^n} + ... \tag{4.2}$$

$$n_{n_i}{}^{t+1} = n_{n_i}^n - u_{n,i}\frac{\Delta t}{\Delta x}\left(n_{n_i}^n - n_{n_{i-1}}^n\right) + \Delta t(-u_{n_i} k A sin(kz_i + \phi)) \tag{4.3}$$

Here, z_i refers to the position of the center of cell z_i. As the upwind method is merely first order accurate in space, no distinction between cell centers and cell average values has to be made. The non-dimensional error at cell i at timestep n is defined as $e_i = \frac{|n_{n_i}^n - n_{man}(x_i)|}{n_{man_{ref}}}$. Convergence of the numerical solution can be determined by applying a threshold to quantify how much the solution evolves from one timestep to another. However in practice, it is often deemed sufficient to run the simulation for a large number of steps and visually investigate convergence. As the order of accuracy of the spatial discretization is evaluated, the CFL number $\frac{u_n \Delta t}{\Delta z}$ is being kept constant as the grid is refined to not skew the results. Forward Euler in time is chosen for its simplicity and allows the verification of the spatial discretization without invoking DifferentialEquations.jl. The $L1$, $L2$ and L_∞ error norms are applied to the errors.

$$E_1 = \frac{1}{N}\sum_{i=1}^{n}|e_i|,\ E_2 = \frac{1}{N}\sum_{i=1}^{n}|e_i|^2 \text{ and } E_\infty = \max|e_{i \text{ for } 1 \leq i \leq N}|$$

All of these norms should experience the same order of convergence. Order verification studies are conveniently plotted on log log scale due to the exponentials with respect to cell size on the truncated terms in the Taylor series when deriving spatial discretizations. The method of manufactured solutions evaluates the order of convergence in a region where the discretization error is dominant. When grid size becomes to small, numerical errors results from machine floating point inaccuracies might dominate. Consequently, order verification studies are usually carried out over 5 - 10 grid refinements. This is sufficient to experimentally investigate the evolution of the error.

In HallThruster.jl, the implementation neutral continuity equation, the ion continuity coupled with the ion momentum equation, the potential equation and the electron energy equation are all verified using the method of manufactured solutions. To allow for a more flexible process, the Julia package Symbolics.jl has been used [46]. It provides symbolic math functionality and thereby enables changing manufactured solutions quickly without the need to manually rederive and rewrite derivatives.

Neutrals and Ions

The neutral and ion equation implementations are verified together. In this case, the advection velocity used for the reference CFL number of 0.2 is the maximum wavespeed appearing in the isothermal Euler system. The value of 0.2 was chosen to allow stability with the 5th order WENO scheme as well. For the other fluxes, any value below 1 would be sufficient, as long as the largest signal velocities are considered in the place of the neutral and ion bulk velocities imposed by the manufactured solution. When the ion momentum equation is electron pressure coupled, the ion sonic speed is effectively the ion acoustic speed as shown in Subsection 3.3.7. Therefore, the CFL number and consequently the timestep used in successive grid refinements is a function of the chosen solution for electron temperature. Manufactured solutions are also applied to all relevant variables that are not being solved self-consistently in this system, but influence the neutrals and ions. This includes the electron temperature, potential profile and consequently electric field, electron mobility and electron velocity. The ionization and excitation coefficients are set to known exponential functions.
An illustration of the exact solution and numerical approximation of the neutral density, ion density and ion velocity is shown in Figure 4.1. The manufactured solutions are presented in the form of previous example

$$n_{n_{man}} = 6 * 10^{13} + 1 * 10^{13} sin\left(\frac{2\pi 0.5}{0.05} + \frac{\pi}{2}\right) \tag{4.4}$$

$$n_{i_{man}} = 6 * 10^{18} + 2 * 10^{18} sin\left(\frac{2\pi 2}{0.05} + \frac{\pi}{2}\right) \tag{4.5}$$

$$u_{i_{man}} = 3000 + 2000 sin\left(\frac{2\pi 0.5}{0.05} - \frac{\pi}{2}\right) \tag{4.6}$$

The order verification studies were carried out for each flux at a few different wavenumbers to ensure correct implementation of the numerical schemes. Plots displaying showing the rate of convergence for neutrals and ions can be inspected in Figure C.1 for the HLLE flux with $n = 1$ for the ion density, $n = 0.5$ for the neutral density and in Figure C.2 with $n = 2$ for the ion density and $n = 4$ for the neutral density. These plots have been generated with piecewise constant reconstruction, therefore the order of accuracy one is expected.

In Figure 4.2 the exact solution is compared to a numerical solution produced by the HLLE flux with piecewiese linear reconstruction using the minmod limiter. The numerical solution develops strong oscillations towards the right end of the domain. Looking at the slope in Figure C.3, it does approach 2 as expected on a coarser grid, however as the grid is refined instabilities develop and the solution becomes increasingly oscillatory before it diverges. It was found that only the osher and the van Leer limiters results produce non-oscillatory results and approach the manufactured solution with an order of accuracy 2. This is shown in Figure C.4.

Consequently, only the use of the osher and van Leer limiters is recommended in HallThruster.jl. The behaviour of the other limiters is not fully understood, since all of them should ensure a total-variation diminishing solution in theory.

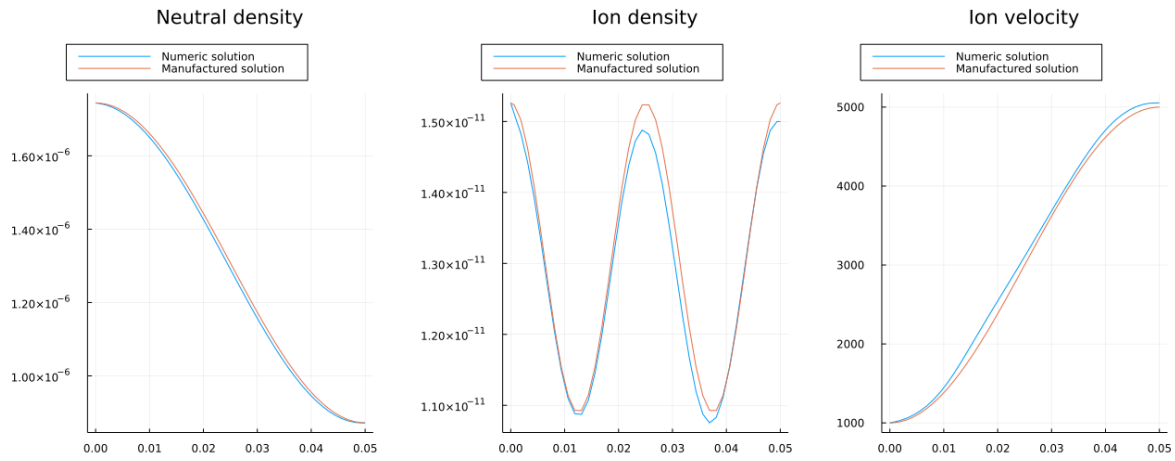

Figure 4.1: Numerical and manufactured solution, HLLE flux, piecewise constant reconstruction, 40 grid cells

Electron energy

The electron energy equation contains both a convective and diffusive term, which invites some discussion. Their relative rates are evaluated using a dimensionless ratio called the Peclet number $P_e = \frac{n_{cells}\sigma}{d}$. In the order verification study, both the CFL number σ and the effective diffusive equivalent d, see

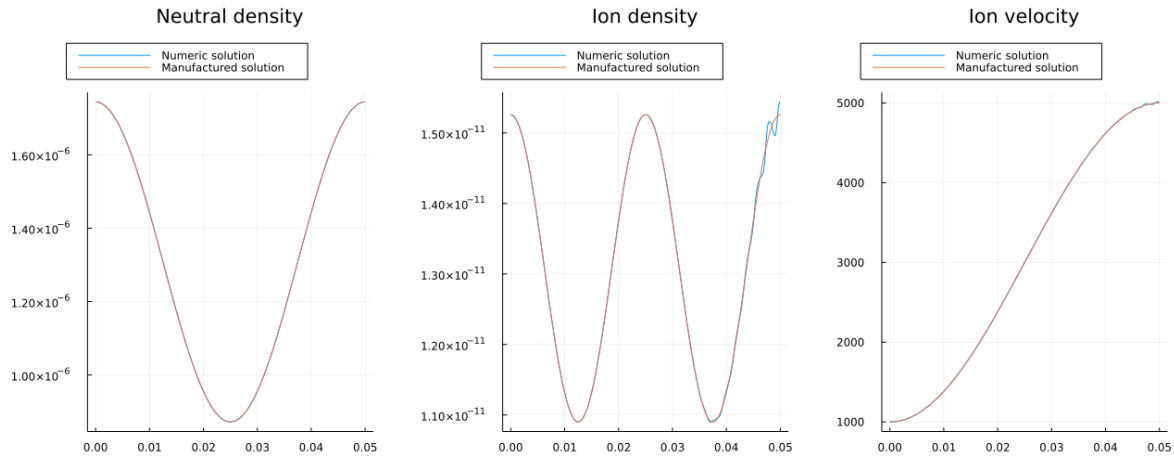

Figure 4.2: Numerical and manufactured solution, HLLE flux, piecewise linear reconstruction, minmod limiter, 200 cells

Subsection 3.3.4, were nonzero, leading to a Peclet number not close to zero. Consequently the order of accuracy resulting from a grid refinement study corresponds to the lowest order in the numerical approximation. This yields an order of accuracy of one, since the discretization of the convective term has a spatial order of accuracy one. Corresponding plots for implict and Crank-Nicolson time integration can be found in Figure C.5 and Figure C.6. Forcing the electron velocity to be very low, yields a Peclet number close to 0. In this case, the the above mentioned plots show second order convergence, corresponding to the discretization of the diffusive term. In addition to what has been described here, Thomas Marks also discretized the convective derivative to second order, the resulting plots can be inspected in Figure C.7 and Figure C.8. This scheme sometimes leads to diverging solutions when applied to Hall thruster simulations in practice, since it is not total-variation diminishing. It is therefore not recommended in practical application.

Potential

The expected spatial order of accuracy for the potential solver is 2, as second order finite differences were applied. As Equation 2.25 is not a partial differential equation, no integration in time is required, which sets this OVS apart from the fluid equations previously considered. Again, all variables that are a function of z and appear in the equation for the potential are set to a manufactured solution based on a trigonometric function. These variables are $\mu_\perp, n_e = n_i, p_e(\epsilon)$. The manufactured solution for ϕ is substituted into the equation and added as a source term. A plot resulting from successive grid refinement can be inspected in Figure C.9. The slope confirms the correct implementation of the discretization. The slight deviation is attributed to the fact that second order finite differences are applied to estimate the derivative for quantities such electron pressure and the ion density.

Evaluation of derivatives

In a similar manner to the potential verification, the implementation of the numerical derivative estimation has been checked. $\nabla\phi$ is critical for ion acceleration source term and electron momentum equation, while ∇p_e is required for the latter as well. Both demonstrate second order of convergence as expected.

4.3 LANDMARK

LANDMARK is a benchmark created by the low temperature magnetized plasma simulation research community to compare codes and help in creating consistent results. One test case is dedicated to a 1D fluid model for Hall Thruster discharges. The reader is refered to reference [26] for a complete list of the physics model. The flexibility of HallThruster.jl allows it to emulate the equations of the Landmark test case. The settings required are listed below and all options can be found in Chapter 2.

- **Constant Sheath Wall loss** The wall loss model adopted is a simple constant sheath model. Coefficients are given and change along the domain. These coefficients differentiate the three cases to be compared in this section.
- **Electron Neutral collisions** A simple electron neutral collision model is applied, determining the collision frequency as a linear function of neutral density.
- **Ionization and excitation model** Lookup tables are supplied in the benchmark and are used to determine rate coefficients as a function of electron temperature.
- **Anomalous collision model** Two-zone Bohm model with $\beta_1 = 1/160$ and $\beta_2 = 1/16$. An additional factor of 10^7 added inside the thruster channel.
- **Electron ion collisions** Neglected.
- **Number of ion charge states** 1.
- **Ion temperature** 0 [K]. In the Landmark study, unlike to HallThruster.jl, the non-conservative ion momentum equation is solved and the pressure contribution is neglected. In order to approximate this, the ion temperature is set to 0, which in turn sets the pressure contribution to 0. In the Landmark study, an additional artificial diffusion term $\eta \frac{\partial^2 u_i}{\partial z^2} u_i$ is added to the ion momentum equation for stability. The artifical viscosity coefficient is applied as $\eta = \delta \sqrt{\frac{2e\epsilon}{3m_i}}$. In this section, the electron pressure coupled method was used in HallThruster.jl, which eliminated the need for artificial diffusion. [1]
- **Heat flux in electron energy equation** The constants in the Braginskii closure for the electron heat flux differ slightly in the LANDMARK benchmark. **add this to heat flux closure description**.
- **Boundary conditions** Similar boundary conditions as described in Subsection 3.3.5. The electron temperature is fixed on both anode and cathode, Dirichlet boundaries are applied on both sides for the potential. The ion velocity at the anode is force to be at least the ion Bohm speed. Ions hitting the anode reenter the discharge channel as neutrals after recombination. A constant neutral mass inflow is applied.
- **Gas** Xenon.

The geometry is loosely approximating an SPT-100 type Hall Thruster. The magnetic field profile is given by

$$B(z) = B_{max} exp\left(-\frac{(z - l_{ch})^2}{2\delta_B^2}\right) \tag{4.7}$$

where $B_{max} = 0.015$ T refers to the maximum magnetic field strength, coincident with the thruster exit plane. $\delta_B = 0.011$ m inside the channel and $\delta_B = 0.018$ m outside. The discharge channel length $l_{ch} = 0.025$ m and the domain length is $L = 0.05m$. The wall loss coefficients differ inside and outside the channel, which differentiates the following three cases.

[1] The global and local Lax-Friedrich flux scheme was found to be diffusive enough to not cause numerical oscillations at the ion stagnation point even when the electron pressure coupled method is not applied.

4.3.1 Time-averaged results

The Landmark benchmark does not mention how many cells or which discretization was used in the computations, however since one the authors mentioned it was most likely 1024 cells, it was decided to use this value. The simulations were carried out for all flux schemes with piecewise constant reconstruction, thus being first order accurate in space and not requiring limiters. The timestep was constant at 1 nanosecond. The electrons were integrated implicitly, being first order accurate in space. For heavy species time-marching a second order strong stability preserving Runge Kutta scheme from DifferentialEquations.jl has been employed. All results shown in the plots corresponding to the three different cases are time-averaged over a period of 1ms, which contains at least 7 breathing mode oscillation periods.

Case 1 $\nu_{ew} = 10^7 \text{ s}^{-1} \ (x \leq l),\ \nu_{ew} = 10^7 \text{ s}^{-1} \ (x > l)$

Case 1 is shown in Figure 4.3. Compared to the reference, the neutral density, potential and electron temperature profile match very well with the global Lax Friedrichs (GLF) and Rusanov (LLF) flux splitting schemes. The HLLE scheme slightly underpredicts electron temperature, while overprediciting ionizaiton rate and plasma density. The ionization region peak can be found at about 0.015 m into the channel, close to the peak of plasma density. Both are slightly skewed compared to the reference data indicating dispersive errors. The value in knowing this is however questionable since the LANDMARK results themselves were created using numerical simulations, with a scheme that most likely exhibits diffusive and dispersive errors as well. The HLLE scheme experiences strong transient effects. The electron velocity close to the anode is large in magnitude. The high values are caused by the short ion backflow region compared to the other cases. This is further discussed in Subsection 4.3.3. The highly oscillatory nature of the HLLE scheme in LANDMARK case 1 is further discussed in Subsection 4.3.3. Overall the time-averaged properties of the LANDMARK benchmark are well approximated.

Case 2 $\nu_{ew} = 0.5 * 10^7 \text{ s}^{-1} \ (x \leq l),\ \nu_{ew} = 10^7 \text{ s}^{-1} \ (x > l)$

Case 2 is presented in Figure 4.4. Inspecting the plot it is evident that a change in wall loss model has a large effect on the overall simulation. Again potential and and electron temperature are very close to the reference data. The plasma density is overpredicted close to the anode. This results in a high ion flux towards the anode, and by recombination therefore raises the neutral density as well. A dispersive shift in ionization rate can be noticed as well. The reason for the strong discrepancy in plasma density could not be determined and remains unknown. The most likely culprit are the boundary conditions. The presheath region in case 2 is much longer, leading to a smoother electron velocity profile and longer ion backflow region. Electric field and potential are well approximated.

Case 3 $\nu_{ew} = 0.4 * 10^7 \text{ s}^{-1} \ (x \leq l),\ \nu_{ew} = 10^7 \text{ s}^{-1} \ (x > l)$

Case 3 is presented in Figure 4.6. The results are very similar to case 2. The plasma and neutral density close to the anode are overestimated as before. Electron temperature and potential profile almost match exactly. Overall, the simulations tend to agree. The discharge currents are compared to the fluid and hybrid LANDMARK cases in Table 4.1. The electron currents are overpredicted by 1 Ampere by all schemes for case 1. The reason might an excessively high plasma density, caused by delayed ionization. The ion exit velocity is notable lower in case 1 compared to cases 2 and 3. A long presheath forms close to the anode, corresponding to a long ion backflow region and moderate electron velocities. A direct comparison of the presheath region in case 1 and 3 focusing on ion velocity and electron temperature profiles is shown in Figure 4.5. In the case of a long presheath region, the electric field is negative or zero over a longer axial distance. This turns the Ohmic heating term in the energy equation, $\mathrm{j} \cdot \mathrm{E}$, effectively into a cooling term. This is an entropy violation and unphysical since random kinetic (thermal) energy

is converted into directed energy without any loss. The effect on the electron temperature of case 3 is clearly visible in Figure 4.5. The ion velocities are differing at the anode since the ion Bohm velocity is enforced as a maximum, but the velocity is allowed to be more negative. As a result, he electric field is actually more negative close to the anode in case 1, albeit over a much shorter axial distance. A higher fidelity anode boundary condition model which self-consistently takes the sheath potential into account and adapts the ion velocity constraint accordingly.

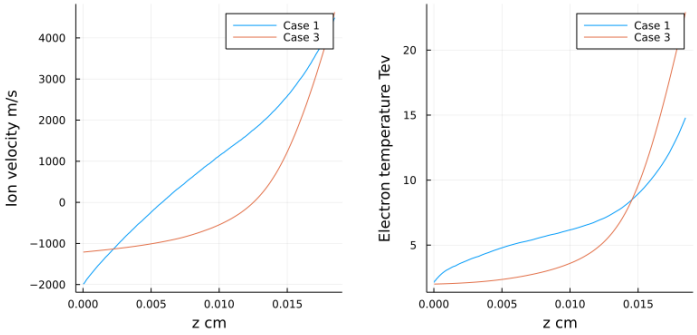

Figure 4.5: The presheath region in case 1 vs case 3

4.3.2 Comparison of flux schemes

In order to gain further insight into code behaviour and be able to make a recommendation as to which approximate Riemann solver to use, the results of the LANDMARK cases have been compared using the global Lax-Friedrichs, local Lax-Friedrichs and HLLE scheme. Looking at the timeaveraged results of case 1, it is evident that the HLLE scheme predicts the highest plasma density, followed by the local and then global Lax Friedrichs FVS schemes. The generally least diffusive scheme therefore results in the highest plasma density. The opposite is true for the electron temperatures. It may look like the Global Lax-Friedrichs scheme best approximates the LANDMARK benchmark, however that might be simply due to the fact that similar flux scheme was employed. The deviation between the different schemes is much smaller in case 2 and 3. One of the reasons might be a similar transient behaviour in these cases, which is highly scheme dependent in case one. Applying second order accuracy in space using piecewise linear reconstruction and the Osher limiter, the time-averaged results are basically identical to the first order schemes. In the transient case however, it can be noted that the oscillation amplitude increases with increasing spatial order of accuracy. The reason is most likely less dissipation in the numerical method.

4.3.3 Transient results

The transient response is of interest, as the breathing mode and transit time oscillations are naturally occurring in Hall Thrusters. Ideally, HallThruster.jl could be used to infer time-resolved anomalous collision frequency profiles. In this case, an accurate and well characterised transient behaviour is of utmost importance. The parameters of interest are the individual ion and electron as well as the total discharge current. The current has been computed at the right boundary, corresponding to the location of the cathode in a 1D domain. The simulations were initialized using coarse approximations of the eventual system states in the domain. This effectively leads to a step input, showing the damping of the system in case the simulation is non-oscillatory. The results for 200 cells are shown in Figure 4.7. In case 1, the local Lax-Friedrichs scheme and the HLLE flux enter a stable oscillatory mode with neither damping nor growth, while in case 3 all three schemes exhibit strong damping. This is in contrast to the results of the LANDMARK study, which predicts a stationary solution in Case 1 and and large

	LANDMARK			HallThruster.jl		
	$\delta = 0.5mm$	$\delta = 1mm$	hybrid (HALLIS)	Global LF	Local LF	HLLE
Electron current						
Case 1	4.54	4.48	4.67	5.16	5.58	5.89
Case 2	4.47	4.37	4.54	4.34	4.34	4.37
Case 3	4.27	4.22	4.37	4.14	4.14	4.16
Ion current						
Case 1	3.67	3.67	3.68	3.69	3.71	3.72
Case 2	3.68	3.68	3.68	3.65	3.65	3.65
Case 3	3.63	3.67	3.66	3.63	3.62	3.62
Total current						
Case 1	8.21	8.15	8.36	8.84	9.30	9.61
Case 2	8.15	8.05	8.22	7.99	7.99	8.02
Case 3	7.90	7.89	8.03	7.77	7.75	7.78

Table 4.1: Comparison of discharge currents using different schemes, Values in Ampere

amplitude low-frequency breathing mode oscillations in Case 3, with Case 2 showing weak low-frequency discharge current oscillations.

Case 1 has been simulated for 5 milliseconds to increase the resolution of the power spectral density in the frequency domain shown in Figure 4.8. The saving interval was 1 μs, which sets the highest resolvable frequency to about 2 Mhz. The range on the x-axis is from 5 to 200 kHz. It was chosen to include such a large range as the increase in spectral density between the 100 and 150 kHz could be interpreted as corresponding to transit time oscillations. The main peak in the Local Lax-Friedrichs scheme can be found at around 8.2 kHz, while in the HLLE case it is around 13.4 kHz. Both show a relatively strong secondary peak at the first harmonic, and strongly attenuated multiple harmonics thereafter. The difference in both oscillation amplitude and frequency is very large. Consequently, these tests show a very high sensitivity of the transient response to the flux scheme used.

The results described above match responses reported by Reference [22]. In this paper, Chapurin et al. study the response of a 1D fluid model to cases similar to the LANDMARK benchmarks. The fluid model is basically identical to HallThruster.jl, solving the continuity equation for neutrals, assuming isothermal ions and also solves for internal electron energy with the same loss terms and employs the drift-diffusion approximation. Neutral and ion losses to the walls are neglected. As in LANDMARK, Chapurin et al. solve the non-conservative ion momentum equation. As in the HLLE case, Chapurin et al. report a high frequency oscillation around 150 kHz, which is modulated by a low frequency breathing mode type oscillation around 15 kHz. In case 3, Ref. [22] report a stable low frequency oscillation without any higher frequency components, which they termed the solo regime. This does not agree with the result in Figure 4.7. However it is shown that the transient behaviour in case 3 is grid dependent. In this case, the higher the amount of cells, the lower the damping in the oscillations. The discharge current response of case 3 with 1024 cells can be inspected in Figure 4.9. The stable oscillations for all three schemes agree with the results predicted by LANDMARK. On the other hand, LANDMARK reports and amplitude of approximately 5 Amperes, while the results show an amplitude of the order 1. Both the frequency and amplitude are flux dependent.

It was hypothesized that the artificial diffusion term in the LANDMARK study might dampen the oscillations in case 1. Consequently, this term has been added to the conservative isothermal equations as well. However, no change in the transient response was observed.

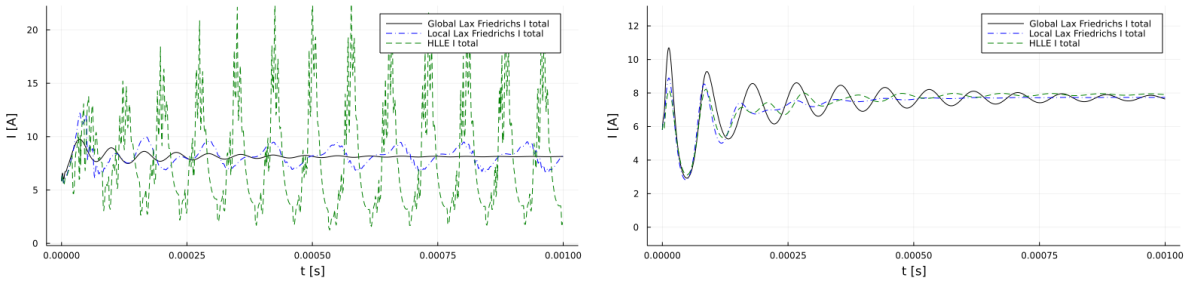

(a) LANDMARK case 1, 200 cells

(b) LANDMARK case 3, 200 cells

Figure 4.7: Comparison of total discharge current over time

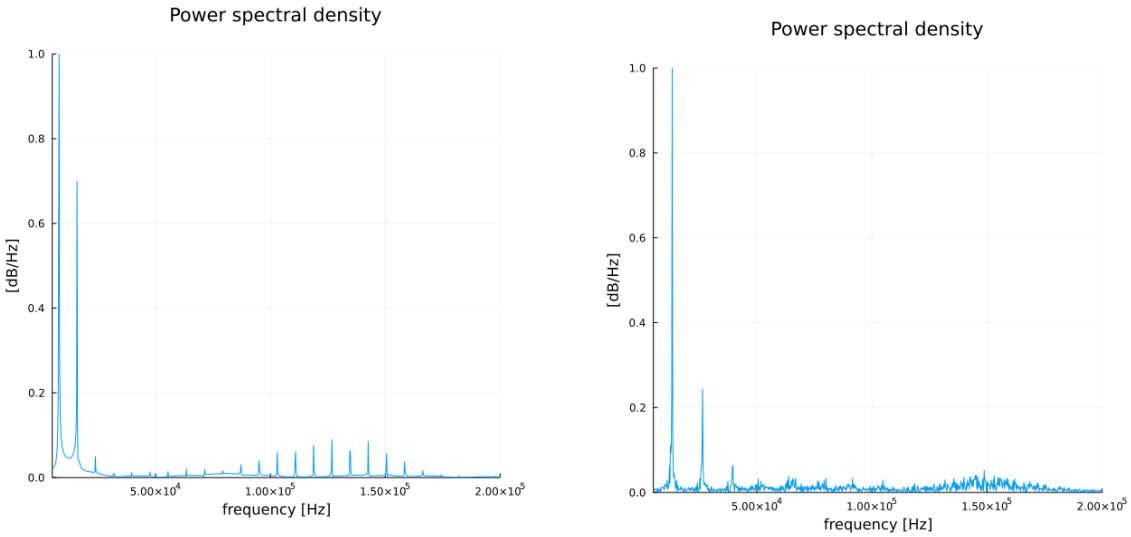

(a) LANDMARK case 1, 200 cells, Local Lax-Friedrichs scheme

(b) LANDMARK case 3, 200 cells, HLLE scheme

Figure 4.8: Power spectral densities, normalized by maximum value in positive domain

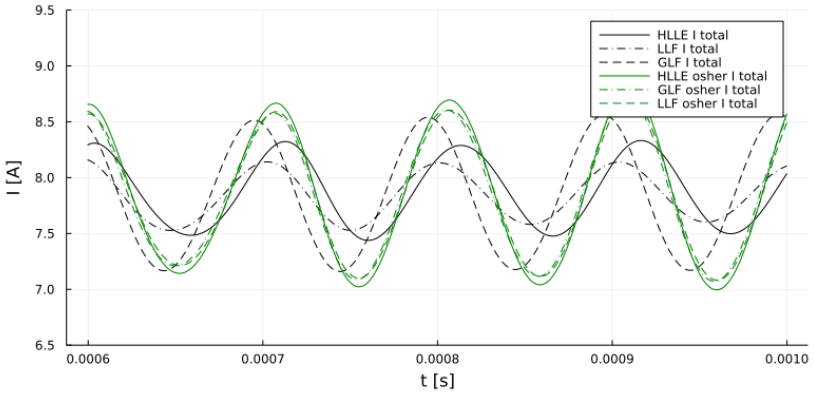

Figure 4.9: Total discharge current, LANDMARK case 3, 1024 cells

4.4 Grid independence study

Ideally, the solution of a numerical simulation should approach the exact solution as the number of computational cells increases. It is expected that the absolute value of the error decreases as a function of the spatial order of accuracy. Vastly differing results between different grid sizes can indicate discretization or implementation errors. Lacking a Hall Thruster realistic time-variant analytical solution to the entire system, the solutions at different grid sizes are merely compared to each other. The CFL number for the heavy species was kept constant throughout grid refinement, which led to $\Delta t_{new} = \Delta t_{old}/2$ if $\Delta x_{new} = \Delta x_{old}/2$. The computational effort scaled linearly with both grid size and timestep, increasing 4 fold with every time the cell size and timestep were halfed. Simulating 1 millisecond, which corresponded to 143000 timesteps for a grid size of 200 cells, took 14 seconds on a machine with 16GB random access memory and an Intel(R) Core(TM) i7-8565U CPU at 1.80GHz. LANDMARK case 1 has been simulated four times with 100, 200, 400 and 800 cells using the electron-pressure coupled method and the HLLE scheme. The time-averaged results are shown in Figure 4.10. The x-axis is normalized over the thruster channel length $l_{ch} = 0.025$ mm. The electron properties and the potential profile look virtually identical as the grid is refined, while a deviation is apparent in the plasma density and ionization rate. Interestingly, there is a large jump in plasma density from 400 to 800 cells, while there seems to be another phenomenon affecting the ion velocity which occurs between 200 and 400 cells. Further investigation is necessary. Figure 4.11 display the total discharge currents over time. The profiles look qualitatively similar, with mid frequency oscillations paired with a lower frequency wave. The oscillation amplitudes and frequencies are comparable. All cases exhibit stable oscillations. The simulations were started from similar initial conditions corresponding to the 200 cell case, which make the 100 cell case appear decaying, however the mode it enters from about $t = 0.0003$ s is stable. Analysing the frequency spectra in Figure 4.12, shows that the oscillation frequencies change with grid refinement. The first large peak corresponding to breathing mode oscillations can found at 14.8 kHz with 100 cells, 13.2 kHz with 200 cells, and 13 kHz with 400 and 800 cells. This might indicate that the oscillation period reaches a natural plateau with sufficiently small grid size. The solutions experience further very low frequency oscillations not shown at the range of the plots in Figure 4.12. The 200 cell case for example has a stable mode at about 400 Hz and one at 1000 Hz. It is concluded that the transient response is grid dependent in both amplitude and frequency, which is not ideal when trying to apply HallThruster.jl to infer time-resolved anomalous collision frequency profiles. Further investigation may reveal that the oscillations are independent of the grid at sufficiently small cell sizes.

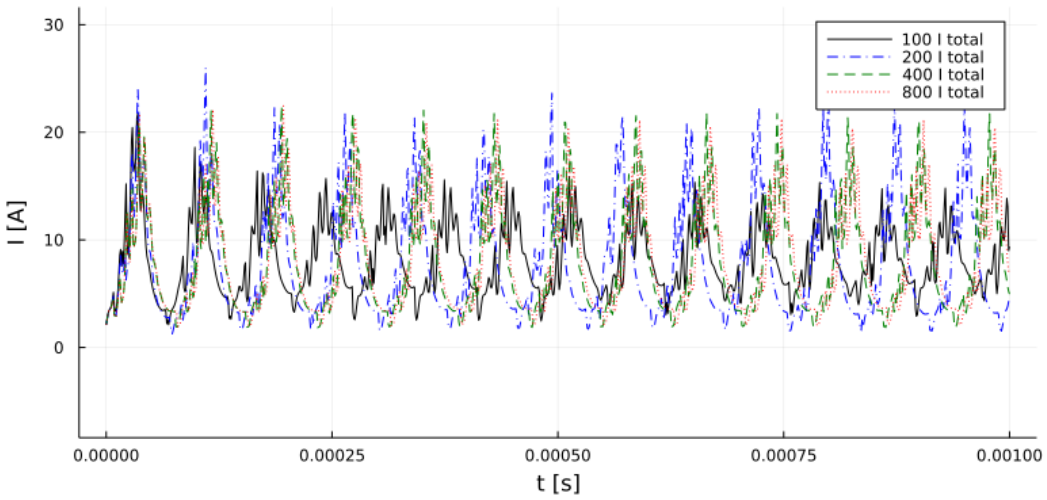

Figure 4.11: Discharge current LANDMARK case 1 at various numbers of cells, HLLE flux

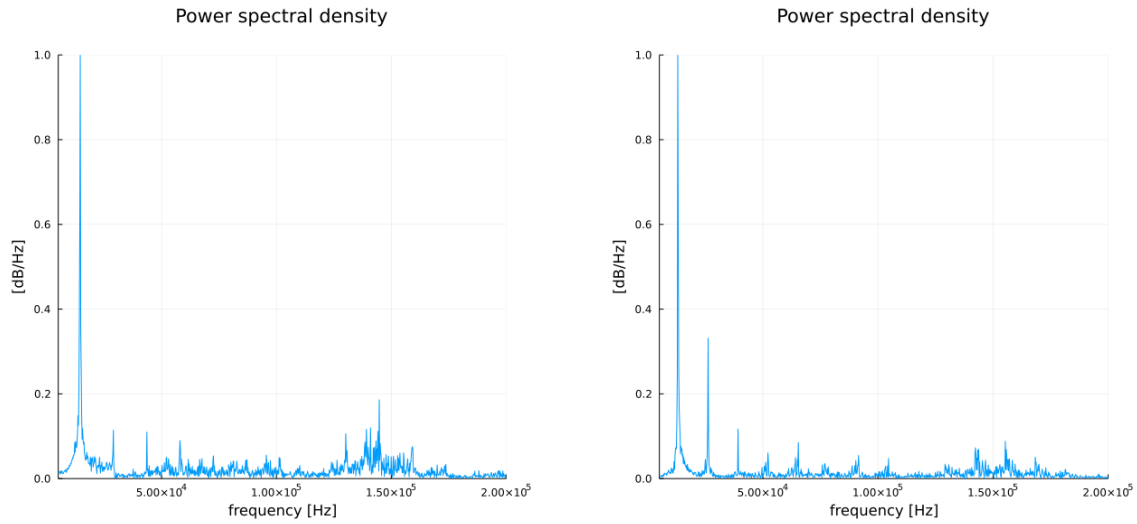

(a) 100 cells

(b) 200 cells

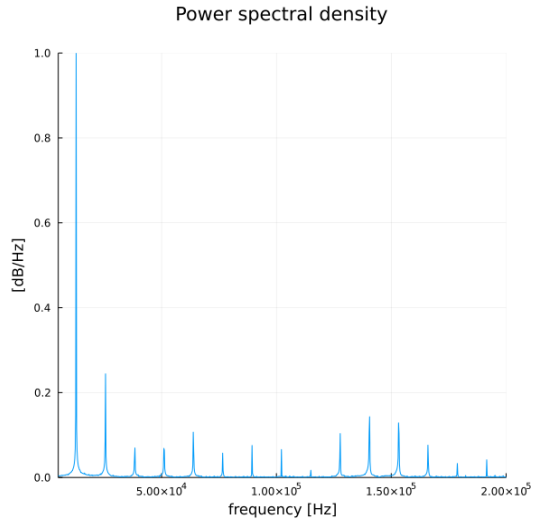

(c) 400 cells

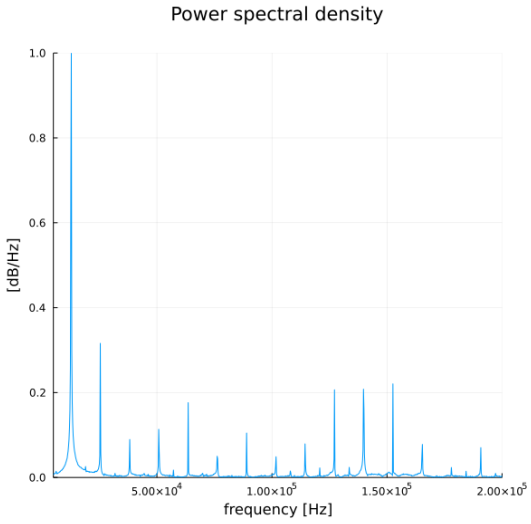

(d) 800 cells

Figure 4.12: Power spectral densities, normalized by maximum value in positive domain, HLLE flux, LANDMARK case 1

4.5 Comparison to HALLIS2D

To gain further understanding of simulation behaviour, the LANDMARK case results have been compared to results obtained with the hybrid 2 dimensional HALLIS code. One difference is that the simulation domain has been extended to 8 cm. The results agree reasonably well, except for the much higher neutral density close to the anode. This might be due to different anode boundary condition in HALLIS.

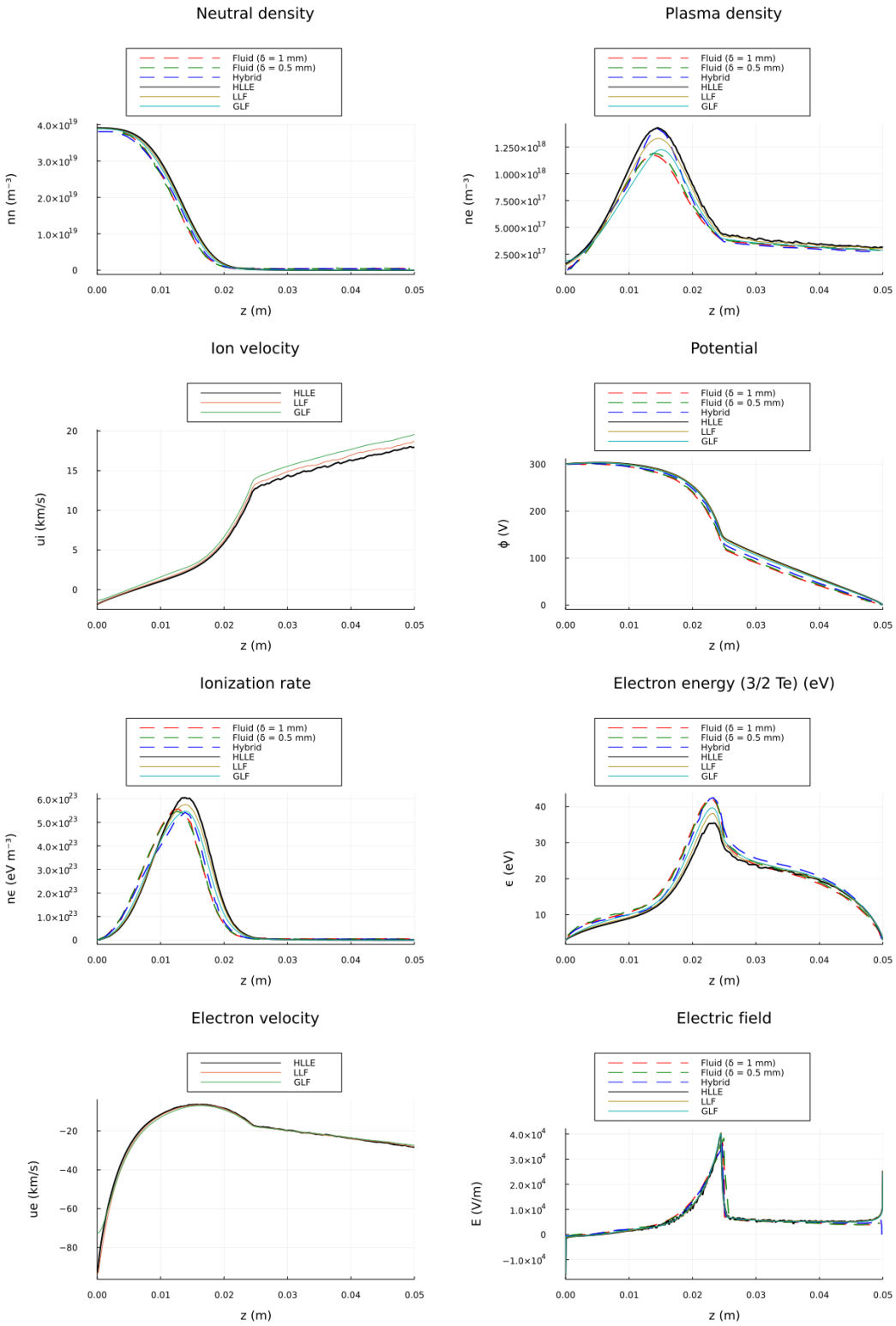

Figure 4.3: Landmark benchmark case 1, 1024 cells

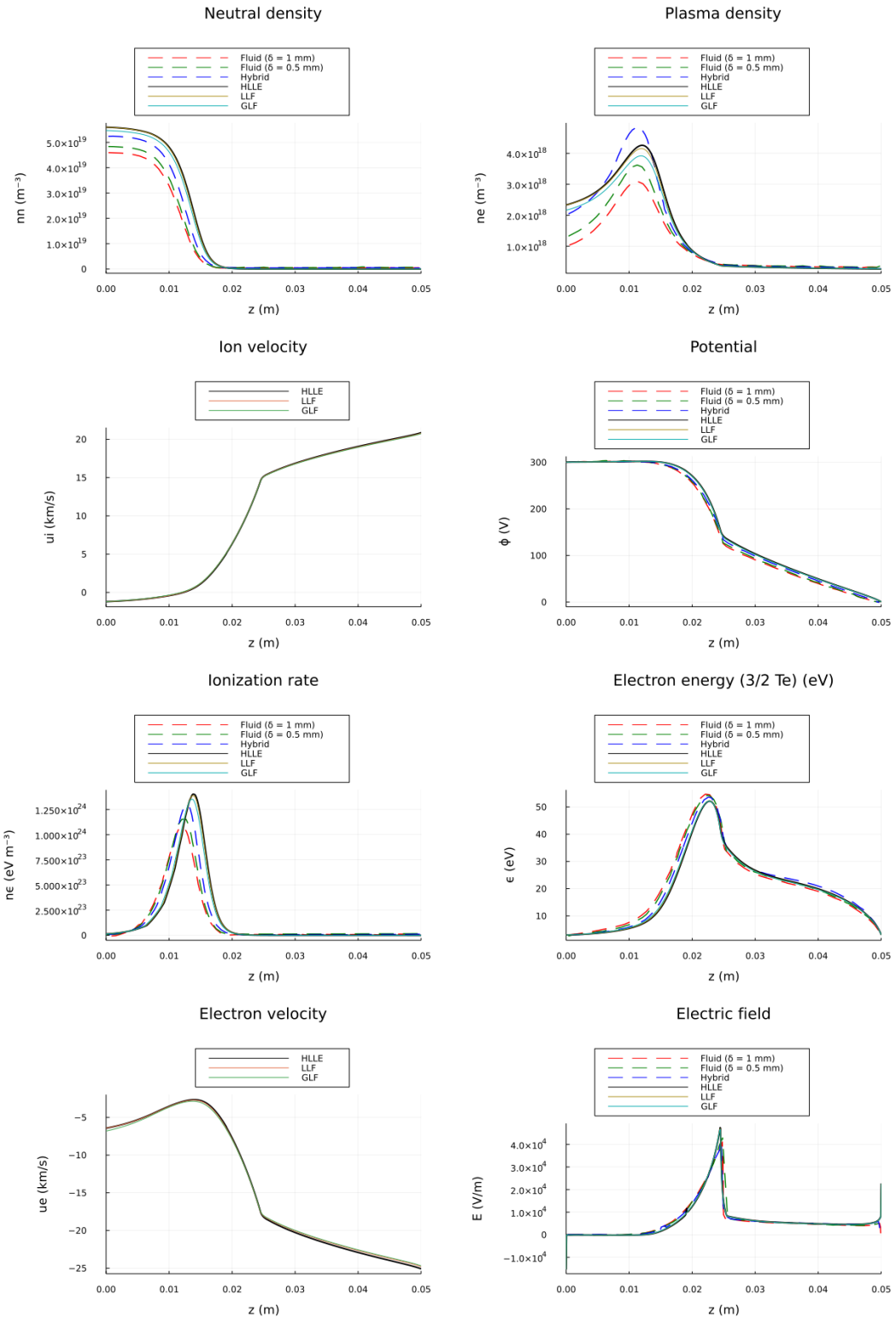

Figure 4.4: Landmark benchmark case 2, 1024 cells

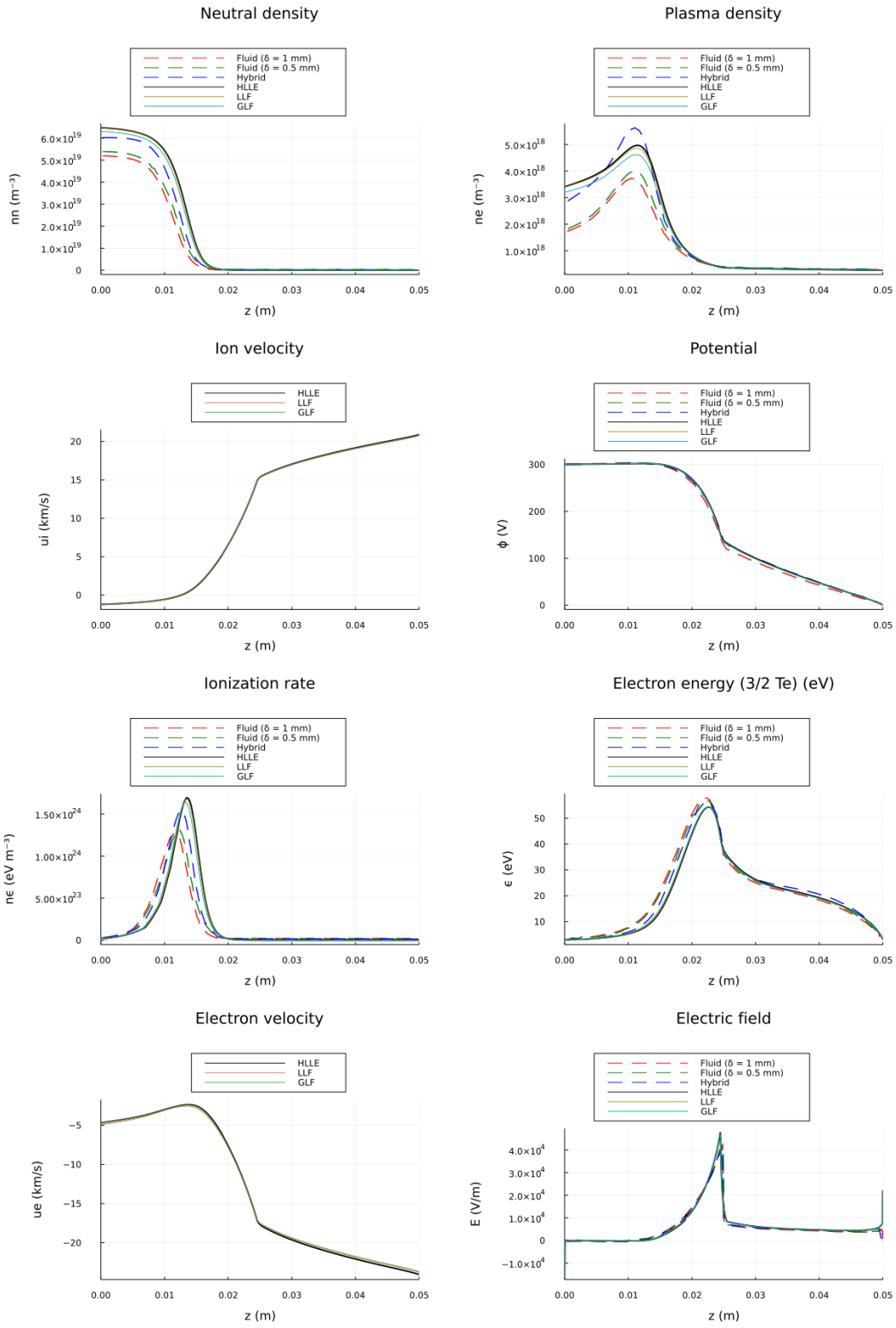

Figure 4.6: Landmark benchmark case 3, 1024 cells

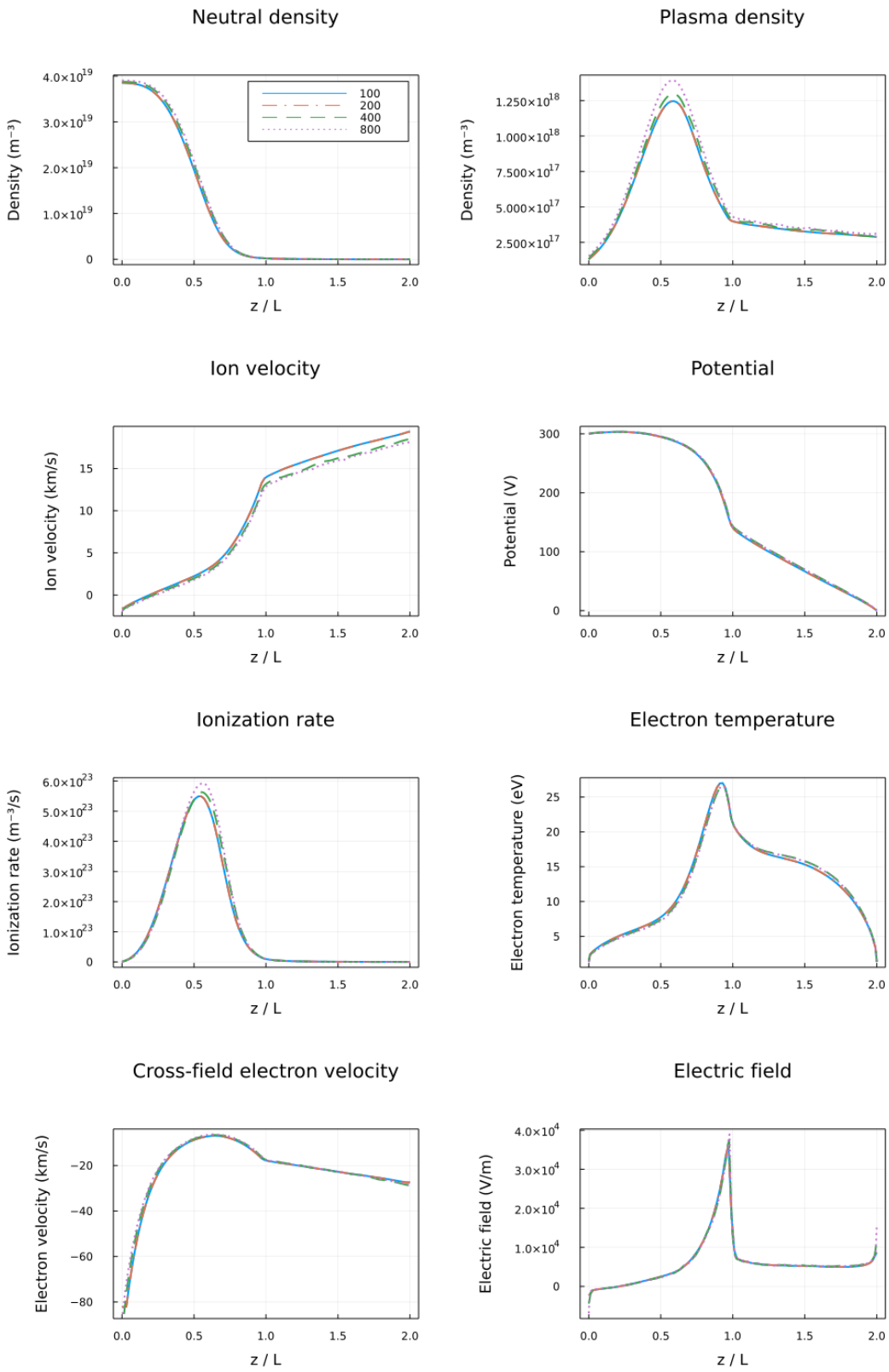

Figure 4.10: LANDMARK case 1 at various numbers of cells, time-averaged results, HLLE flux

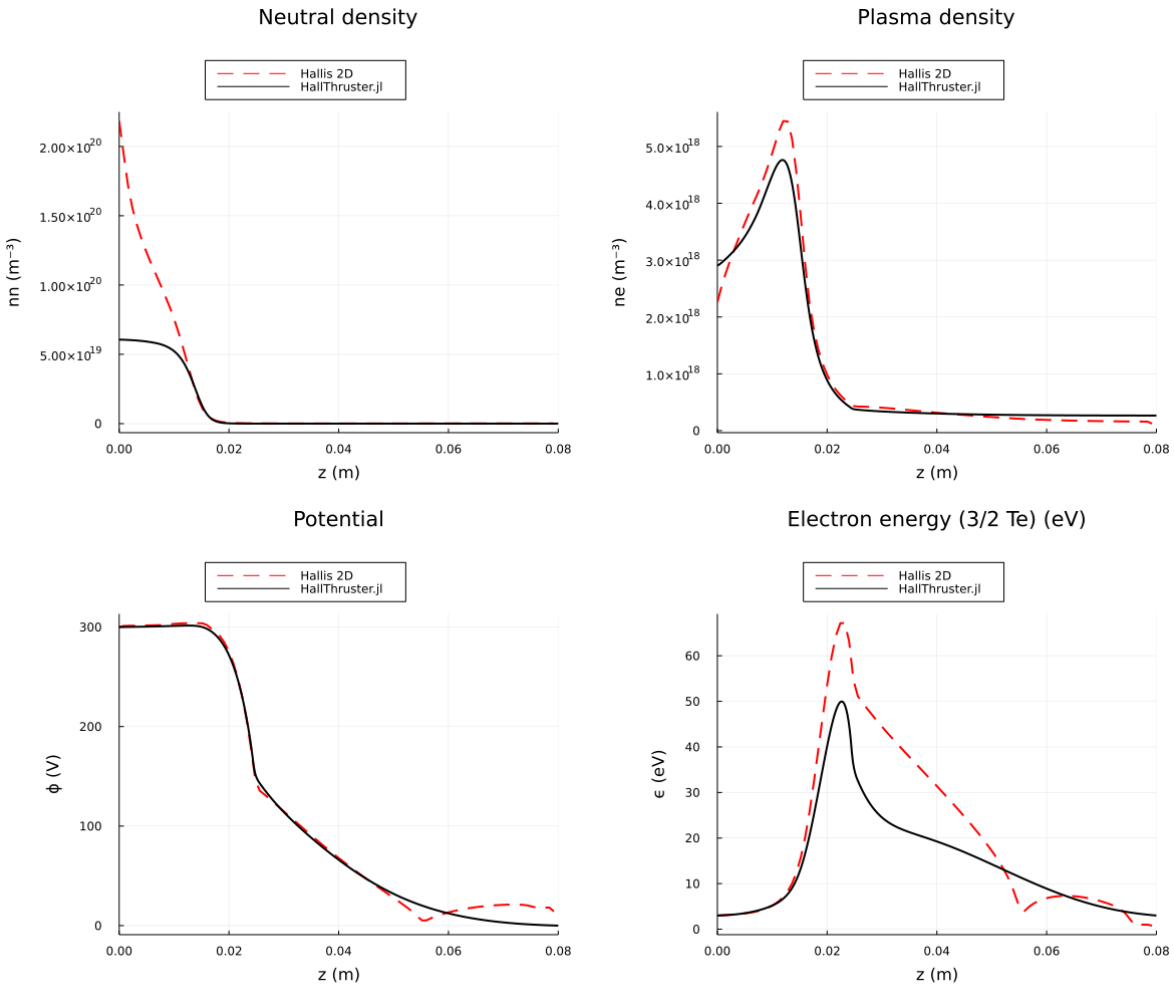

Figure 4.13: Comparison of Landmark case 3 simulated with HALLIS 2D and HallThruster.jl

Chapter 5

Comparison to Hall2De results

The implementation of HallThruster.jl has been verified in the previous chapter. The code can now be applied to a more realistic problem, trying to approximate the SPT-100 thruster. A higher fidelity anomalous collision frequency profile is used, and the results are compared to a simulation obtained by Hall2De. Ultimately the goal is to use HallThruster.jl for anomalous collision frequency calibration tasks, therefore robustness and accuracy with employing higher fidelity source terms is of paramount importance.

5.1 Simulation of SPT-100

A SPT-100 is shown in Figure 5.1. In operation, it produces a thrust of about 90 mN at a nominal power rating of 1.35 kW. It is the same thruster the LANDMARK study attempts to emulate. However, in this section, higher fidelity physics are applied to achieve a more realistic simulation. The simulation characteristics are listed here for repeatability.

- **Anomalous collision frequency model** The model chosen has been identified by [17] and was calibrated by [18]. The model is shown and explained below.
- **Electron ion collisions** are considered.
- **Number ion charge states** 1.
- **Ion temperature** 500 [K].
- **Gas** Xenon.
- **Neutral mass inflow** 4.93 g/s.
- **Injection velocity** 300 m/s.
- **Electron temperature at cathode** 2 eV.
- **Potential drop** 300 V.
- **Geometry** $L_{ch} = 0.025$ m.

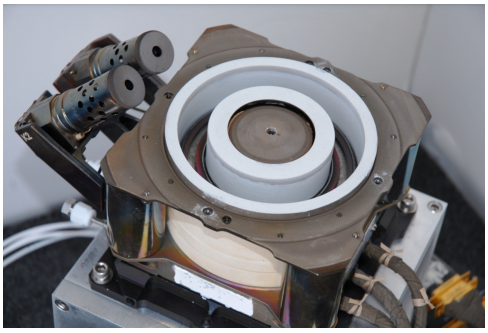

Figure 5.1: A SPT-100 flight model [1]

The magnetic field is described by Equation 4.7. The anomalous collision frequency model is of the form

$$\nu_{AN} = \omega_{ce}\left(c_0 + \frac{c_1|\mathbf{u_i}|}{c_2 c_s + \nu_{de}}\right) \tag{5.1}$$

where ω_{ce} is the electron cyclotron frequency, $|u_i|$ is the local magnitude of the ion velocity, $c_s = \sqrt{T_{ev}/m_i}$ the local ion acoustic speed and $\nu_{de} = |\frac{E}{B}|$ the ratio of electric to magnetic field.

In the 1D code, a Dirichlet boundary to the electron temperature was applied at the anode as well, forcing it to 2eV. The following physics models were applied in HallThruster.jl.

- **Wall loss model** The Hobbs Wesson wall loss model is adopted. The sheath potential is evaluated self-consistently a function of electron temperature and secondary electron emission coefficient. Boron Nitride is used as a wall material.
- **Electron Neutral collisions** The higher fidelity lookup table for electron neutral collisions is used. The coefficients were generated integrating the collisional cross sections over the maxwellian velocity distribution.

- **Ionization and excitation model** Ionization and excitation rates created with the BOLSIG+ code are used. [25]

Here, a simulation of a SPT-100 is carried out and compared to the results obtained using the Hall2De code developed by JPL [13]. The domain length in the 1D simulation was 0.08 m, which is slightly more than 3 channel lengths. The coefficients in the anomalous collision frequency model were chosen to be $c_0 = 0$, $c_1 = 2$ and $c_2 = 3$. In addition, in an effort to display sensitivity, HallThruster.jl has been run 49 times were the coefficients were drawn from normal distributions centered around previously mentioned values. The standard deviations were estimated from [18] and are $\sigma_0 = 0.005$, $\sigma_1 = 0.5$ and $\sigma_2 = 2.5$. Figure 5.3 presents the time-averaged results. Averaging was started once the discharge currents seemed to have reached steady-state. The computational complexity of a Hall2De simulation is about 4000 times higher than HallThruster.jl. [1]

The neutral density at the anode is extremely low in HallThruster.jl compared to Hall2De. This is most likely a result of the boundary conditions. Hall2De uses a higher fidelity anode model that self-consistently evaluates the sheath potential and does not enforce an ion attracting sheath. Interestingly, the plasma density at the anode is higher in HallThruster.jl. Looking at the evolution over the axial domain, the plasma density is notably higher in the one-dimensional simulation. This coupled with a higher exit velocity overpredicts the thrust, as evident in Figure 5.2b. The acceleration profile and location of the maximum electric field is shifted between the two simulations. This is also evident in the electron temperature profile. The discharge currents are compared in Figure 5.2a. Both simulations show low frequency breathing mode oscillations together with lower amplitude transit time oscillations. The pattern in HallThruster.jl is much more uniform, which could be a result of the lower dimensionality. In order to quantitatively compare the simulation results on a global scale, the Hall thruster efficiency model first proposed by Hofer can be applied. [47] The model breaks the anode efficiency down into five individual efficiencies, shown in Equation 5.2. See Appendix A for a definition of the components.

$$\eta_a = \frac{T^2}{2\dot{m}_a V_d I_d} = \eta_m \eta_d \eta_b \eta_v \eta_q \tag{5.2}$$

In Table 5.1 the efficiencies of both simulations are presented. Since HallThruster.jl is a 1D code, the divergence efficiency η_d is by definition 1, which is a stark contrast to Hall2De's 60%. The mass utilization efficiency η_m is one in the 1D simulation, which would mean that all propellant is ionized, which is certainly not realistic. The beam utilization efficiency η_b is comparable in both cases, indicating a similar fraction of ion to total current. Voltage utilization η_v in the case of HallThruster.jl is higher than 1, meaning that the average ion sees a larger potential drop than the applied voltage. One contributing factor are the simple boundary conditions and the lack of a cathode coupling model, forcing the potential to be 0 at the outflow. The discrepancy is evident comparing the potential profiles at the right boundary. In addition, the potential at the anode is increased by the presheath. The charge utilization efficiency η_q is 1 in both cases by definition, since only singly charged ions were considered in this simulation. Histograms showing the sensitivity of the efficiencies on the coefficients in the anomalous collision frequency model are shown in Figure B.1. This has been mostly done for illustrative purposes showing the impact of the coefficients.

	I_a (A)	T (mN)	η_m	η_b	η_v	η_d	η_q	η_a
Hall2De	8.47	65.1	0.96	0.41	0.81	0.61	1.00	0.19
HallThruster.jl	8.72	105.6	1.00	0.42	1.04	1.00	1.00	0.43

Table 5.1: Efficiencies obtained with Hall2De and HallThruster.jl

Insights from this study can be applied to make recommendations for future work. First, the discrepancy in beam divergence η_d is expected and can be relatively easily compensated for, by making an educated

[1] Evaluated from the ratio of runtimes of each simulation using the same machine.

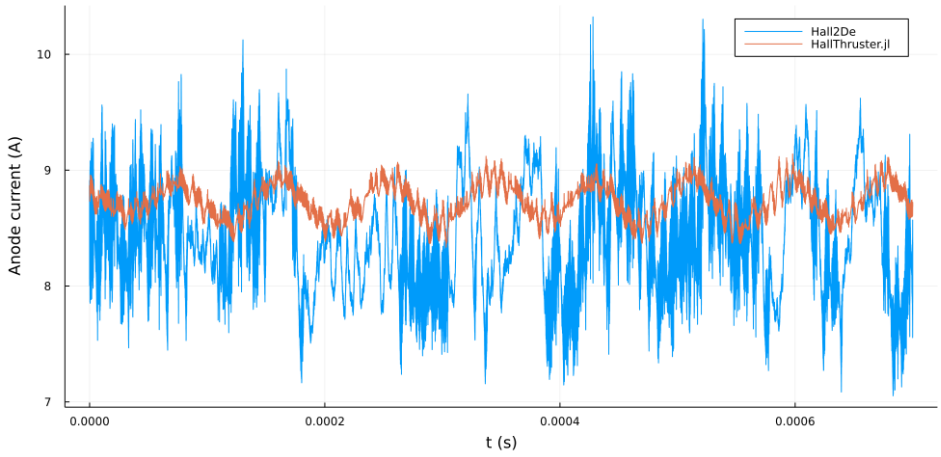

(a) Anode current

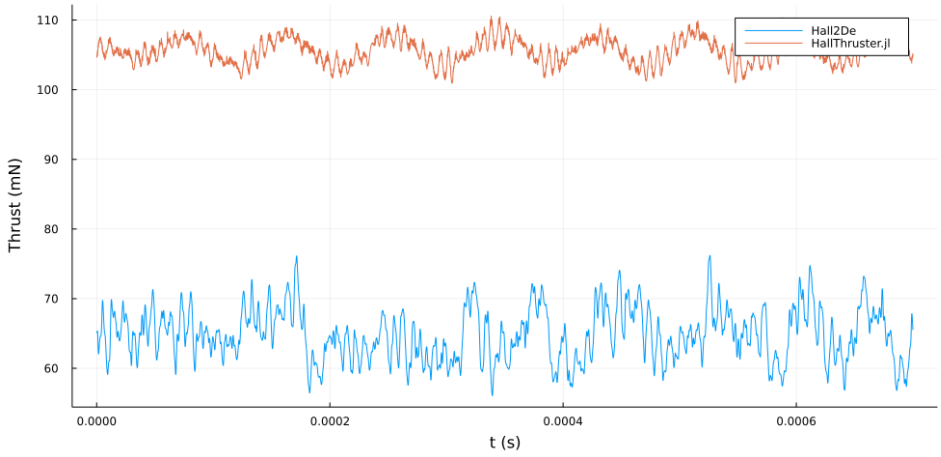

(b) Thrust

Figure 5.2: Transient behaviour of HallThruster.jl and Hall2De simulations of the SPT-100

guess on the divergence for HallThruster.jl. Such a mapping can be calibrated. Second, the discrepancy in the voltage utilization η_v can be decreased by employing higher fidelity anode and cathode coupling models. Especially the potential difference at the cathode is immediately apparent. Thirdly, the beam utilization efficiency η_b matches very well between the two simulations, instilling confidence that the results can be extrapolated to higher dimensions. Last but not least, the discrepancy in the mass utilization η_m should be investigated further. The root cause is immediately clear and might have to do with the ionization rate coefficients. Investigating these points and applying corrections will lead to closer alignment between the anode efficiencies and thrust values.

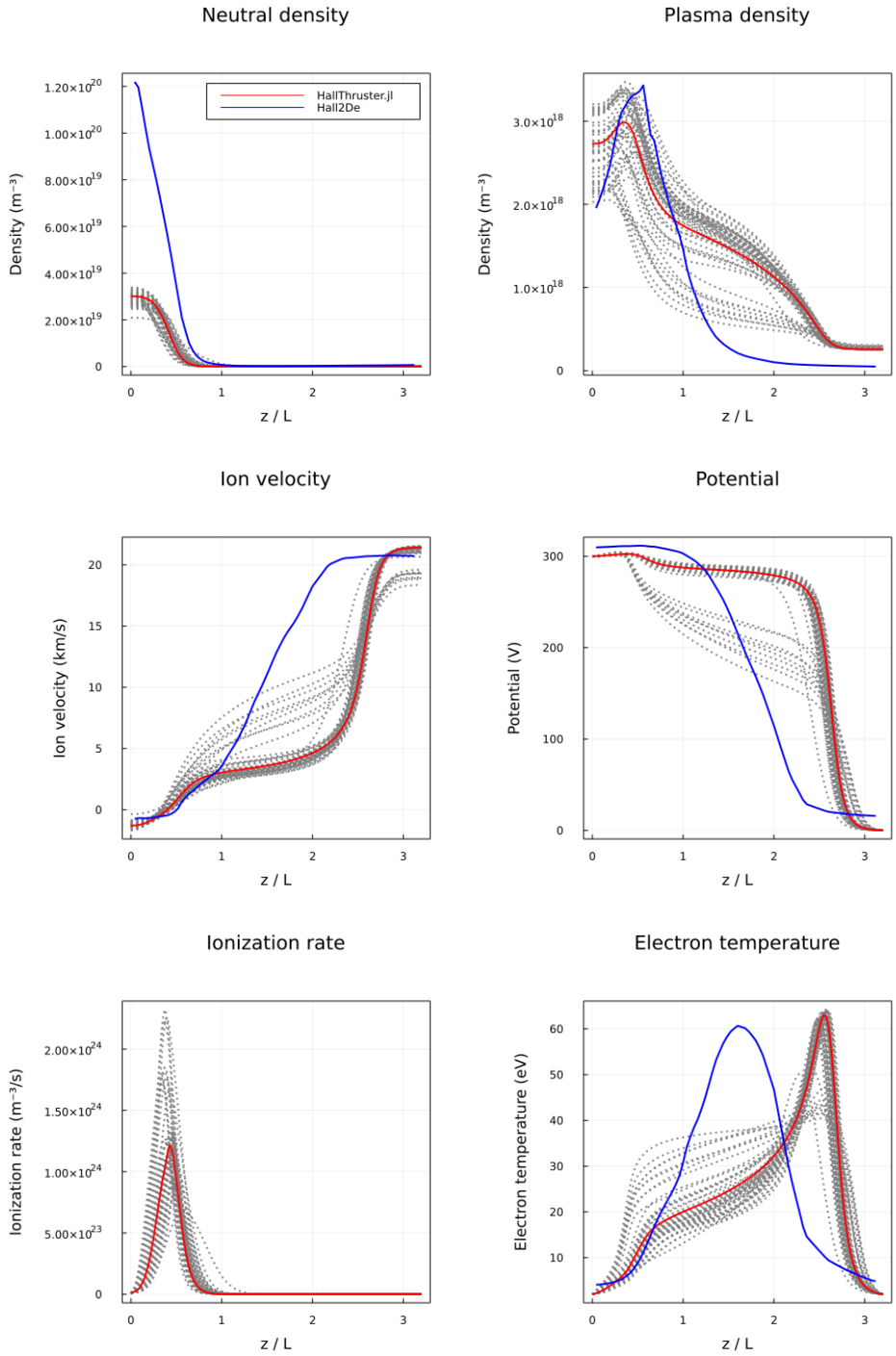

Figure 5.3: Time-averaged results of the SPT-100 simulation. Solid lines: $c_0 = 0, c_1 = 2, c_2 = 3$ in Equation 5.1. Dotted lines: 49 simulations with HallThruster.jl where coefficients c_0, c_1 and c_2 were drawn from normal distributions

Chapter 6

Conclusion & Outlook

The demand for predictive Hall thruster simulations has been outlined in Chapter 1. It was shown that the main issue preventing predictive simulations is the increased electron cross field transport compared to classical theory when employing fluid approximations. The need to calibrate new closure models comes along with a requirement for more data for inference tasks. It was shown that 2D fluid or hybrid codes are too expensive to evaluate for such purposes, while a 1D fluid model wins the trade-off between fidelity and complexity. However, no openly accessible 1D fluid models were easily adaptable or had the ability to change physical approximations by the user. Consequently, a 1D fluid model for Hall thruster discharges has been derived and implemented in the programming language Julia, applying Julia's multiple dispatch architecture.

The correct implementation of the governing equations has been verified. Additionally, the model was compared to the LANDMARK case study and the deviations have been discussed, with the time-averaged results matching very well. A grid independence study was carried out showing overall consistency in the time-averaged results, while the oscillatory behaviour changed both in amplitude and in frequency. Furthermore, the time-averaged results have been compared to the 2D hybrid code HALLIS, with the results aligning well.

The runtime of HallThruster.jl is drastically lower than a 2D fluid simulation. A discharge simulation over 1 ms after reaching steady-state is usually considered sufficient to resolve the axial transient phenomena of interest. On the same machine, the runtime of such a simulation for Hall2De is typically on the order of 10 hours, while it takes HallThruster.jl about 10 seconds. The simulation thus fulfills the requirements outlined in the introduction.

Before applying HallThruster.jl to inference tasks, it is recommended to adapt the electron energy source terms, as discussed in Chapter 2 and Section 4.3. Furthermore, the implementation of a self-consistent anode sheath model would increase model fidelity. This would result in relaxing the requirement for a strictly ion attracting sheath, which means the strict enforcement of the ion Bohm velocity at the anode could be relaxed as well. One model requiring an iterative procedure is outlined in [48] [49], while a direct evaluation is possible with the model proposed in [50]. In addition to that, the model fidelity could be increased by treating the boundary conditions more carefully. Rather than assuming flux conservation at the anode, the velocity distribution function could be reconstructed and a kinetic flux vector splitting scheme applied. This would allow capturing the recombination at the anode in a more realistic way. An implementation is discussed in [21] and is based on the methodologies outlined in [51] and [52]. Due to the nature of the 1D geometry, the cathode is coincident with the outflow. By enforcing a 0 potential at the outflow, the voltage utilization efficiency will always be overestimated, as cathode coupling is not modelled. Including such a model could lead to lower and more realistic acceleration voltages.

The code can then be compared again to higher fidelity simulations and experiments. HallThruster.jl can subsequently be applied to Bayesian inference tasks to find anomalous collision frequency model coefficients, similar to what has been described in [18]. The quick runtime enables running many more simulations while sampling parameters of interest from probability distributions. Through applying a surrogate modelling approach, the results from the lower fidelity 1D simulations can inform the parameter space for 2D simulations, therefore requiring less high fidelity simulations and reducing overall computational cost.

Another approach inspired by dynamical systems theory would be to represent the time evolution of state parameters in a Hall thruster simulation as a time-lagged phase portrait, where the parameter evolution is mapped against itself at a different time. When both the reference (training) data and simulation data are represented in such a way, the difference between the two can be evaluated using

a defined metric. The difference, or cost function, can then be optimised by drawing input coefficients from a probability distribution until the cost function converges to a minimum. This approach allows to calibrate anomalous collision frequency models. [53]

Further possibilities are opened by applying Kalman Filters. Greve et al. [54] have been applying an extended Kalman Filter to estimate state variables in Hall thrusters from discharge current measurements. For application to data assimilation and parameter estimation tasks, such as calibrating anomalous collision frequency models, ensemble Kalman Filters are suited well. [55] One advantage of ensemble Kalman Filters is that they do not require an underlying linear model. It could therefore be directly integrated with Hallthruster.jl. The best version to apply is probably the ensemble transform Kalman Filter, in which the gain K is computed in a lower dimensional subspace. In their standard form these filters, merely estimate the state based on current and past measurements, while in the setting of parameter calibration against already existing data, future states could be used for parameter estimation as well. This is exactly the principle of the Ensemble Kalman Smoother (EnKs). [56]

To conclude, the stage is set for exciting model calibration tasks. Paired with physical insights gained through experiments and possibly the application of turbulent theory, this will one day lead to practical and predictive Hall thruster simulations. These seem, in light of the volatility of the inert gas market, more important than ever. In addition to reducing expensive testing, predictive simulations will allow more advanced system optimisation and thus contribute to better Hall thruster designs. In the high power segment, it is these very designs that have the potential to power human spaceflight ambitions to the Moon, Mars and beyond.

Bibliography

[1] M. Nakles, W. Hargus, J. Delgado, and R. Corey, "A performance comparison of xenon and krypton propellant on an spt-100 hall thruster," 09 2011.

[2] K. W. Crane, E. Linck, B. Lal, and R. Y. Wei, "Measuring the space economy: Estimating the value of economic activities in and for space," tech. rep., Institute for Defense Analyses, 2020.

[3] B. R. Frongello, W. A. Hoskins, R. J. Cassady, K. L. Kalkowska, and P. K. Maliga, *Spacecraft Electric Propulsion at an Inflection Point.*

[4] I. G. Mikellides, I. Katz, R. R. Hofer, and D. M. Goebel, "Magnetic shielding of a laboratory hall thruster. i. theory and validation," *Journal of Applied Physics*, vol. 115, no. 4, p. 043303, 2014.

[5] J. S. Snyder, V. H. Chaplin, D. M. Goebel, R. R. Hofer, A. L. Ortega, I. G. Mikellides, T. Kerl, G. Lenguito, F. Aghazadeh, and I. Johnson, *Electric Propulsion for the Psyche Mission: Development Activities and Status.*

[6] R. Liang, "The combination of two concentric discharge channels into a nested hall-effect thruster.," 2013.

[7] D. M. Goebel and I. Katz, *Fundamentals of Electric Propulsion*, ch. 7, pp. 325–392. John Wiley and Sons, Ltd, 2008.

[8] J. Fife, M. Martinez-Sanchez, and J. Szabo, *A numerical study of low-frequency discharge oscillations in Hall thrusters.*

[9] T. Lafleur, P. Chabert, and A. Bourdon, "The origin of the breathing mode in hall thrusters and its stabilization," *Journal of Applied Physics*, vol. 130, no. 5, p. 053305, 2021.

[10] O. Chapurin, A. I. Smolyakov, G. Hagelaar, and Y. Raitses, "On the mechanism of ionization oscillations in hall thrusters," *Journal of Applied Physics*, vol. 129, no. 23, p. 233307, 2021.

[11] K. Hara, "Non-oscillatory quasineutral fluid model of cross-field discharge plasmas," *Physics of Plasmas*, vol. 25, no. 12, p. 123508, 2018.

[12] J. C. Adam, A. Héron, and G. Laval, "Study of stationary plasma thrusters using two-dimensional fully kinetic simulations," *Physics of Plasmas*, vol. 11, no. 1, pp. 295–305, 2004.

[13] I. G. Mikellides and I. Katz, "Numerical simulations of hall-effect plasma accelerators on a magnetic-field-aligned mesh," *Phys. Rev. E*, vol. 86, p. 046703, Oct 2012.

[14] J. Perales-Díaz, A. Domínguez-Vázquez, P. Fajardo, E. Ahedo, F. Faraji, M. Reza, and T. Andreussi, "Hybrid plasma simulations of a magnetically shielded hall thruster," *Journal of Applied Physics*, vol. 131, no. 10, p. 103302, 2022.

[15] "Hallis model,"

[16] S. Tsikata, N. Lemoine, V. Pisarev, and D. M. Grésillon, "Dispersion relations of electron density fluctuations in a hall thruster plasma, observed by collective light scattering," *Physics of Plasmas*, vol. 16, no. 3, p. 033506, 2009.

[17] B. Jorns, "Predictive, data-driven model for the anomalous electron collision frequency in a Hall effect thruster," *Plasma Sources Science Technology*, vol. 27, p. 104007, Oct. 2018.

[18] T. A. Marks, A. L. Ortega, I. G. Mikellides, and B. Jorns, *Self-consistent implementation of a zero-equation transport model into a predictive model for a Hall effect thruster.* 2021.

[19] J. P. Boeuf and L. Garrigues, "Low frequency oscillations in a stationary plasma thruster," *Journal of Applied Physics*, vol. 84, no. 7, pp. 3541–3554, 1998.

[20] G. Hagelaar and G. Kroesen, "Speeding up fluid models for gas discharges by implicit treatment of the electron energy source term," *Journal of Computational Physics*, vol. 159, no. 1, pp. 1–12, 2000.

[21] R. Sahu, A. R. Mansour, and K. Hara, "Full fluid moment model for low temperature magnetized plasmas," *Physics of Plasmas*, vol. 27, no. 11, p. 113505, 2020.

[22] O. Chapurin, A. Smolyakov, G. Hagelaar, j.-p. Boeuf, and Y. Raitses, "Fluid and hybrid simulations of the ionization instabilities in hall thruster," 01 2022.

[23] T. Marks and P. Schedler, "Hallthruster.jl," Github, 2022.

[24] P. M. Bellan, "Fundamentals of plasma physics," 2006.

[25] G. J. M. Hagelaar and L. C. Pitchford, "Solving the boltzmann equation to obtain electron transport coefficients and rate coefficients for fluid models," *Plasma Sources Science and Technology*, vol. 14, pp. 722–733, oct 2005.

[26] "Landmark 1d fluid test case." `https://www.landmark-plasma.com/test-case-3`. Accessed: 2021-12-23.

[27] I. Katz, J. R. Anderson, J. E. Polk, and J. R. Brophy, "One-dimensional hollow cathode model," *Journal of Propulsion and Power*, vol. 19, no. 4, pp. 595–600, 2003.

[28] J. D. Huba, "Nrl plasma formulary." `https://library.psfc.mit.edu/catalog/online_pubs/NRL_FORMULARY_13.pdf`, 2013. Accessed: 2022-04-14.

[29] J.-P. Boeuf, "Tutorial: Physics and modeling of hall thrusters," *Journal of Applied Physics*, vol. 121, no. 1, p. 011101, 2017.

[30] Y. V. Esipchuk and G. N. Tilinin, "Drift instability in a hall-current plasma accelerator," *Sov. Phys. - Tech. Phys. (Engl. Transl.); (United States)*, 4 1976.

[31] A. I. Morozov and V. V. Savelyev, *Fundamentals of Stationary Plasma Thruster Theory*, pp. 203–391. Boston, MA: Springer US, 2000.

[32] T. Lafleur, S. D. Baalrud, and P. Chabert, "Theory for the anomalous electron transport in hall effect thrusters. i. insights from particle-in-cell simulations," *Physics of Plasmas*, vol. 23, no. 5, p. 053502, 2016.

[33] B. A. Jorns, "Two equation closure model for plasma turbulence in a hall effect thruster," 2019.

[34] S.I.Braginskii, *in Reviews of Plasma Physics*. 1965.

[35] G. D. Hobbs and J. A. Wesson, "Heat flow through a langmuir sheath in the presence of electron emission," *Plasma Physics*, vol. 9, pp. 85–87, jan 1967.

[36] N. Gascon, M. Dudeck, and S. Barral, "Wall material effects in stationary plasma thrusters. i. parametric studies of an spt-100," *Physics of Plasmas*, vol. 10, no. 10, pp. 4123–4136, 2003.

[37] E. Ahedo, P. Martínez-Cerezo, and M. Martinez-Sanchez, "One-dimensional model of the plasma flow in a hall thruster," *Physics of Plasmas*, vol. 8, pp. 3058–3068, 06 2001.

[38] A. Cohen-Zur, A. Fruchtman, J. Ashkenazy, and A. Gany, "Analysis of the steady-state axial flow in the hall thruster," *Physics of Plasmas*, vol. 9, no. 10, pp. 4363–4374, 2002.

[39] P. J. Roberts, V. H. Chaplin, A. Lopez Ortega, and I. G. Mikellides, "Impact of low-frequency oscillations on ion energy in a high-power magnetically shielded hall thruster," *Journal of Applied Physics*, vol. 131, no. 3, p. 033301, 2022.

[40] C. Rackauckas and Q. Nie, "Differentialequations.jl–a performant and feature-rich ecosystem for solving differential equations in julia," *Journal of Open Research Software*, vol. 5, no. 1, 2017.

[41] R. J. LeVeque, *Finite Volume Methods for Hyperbolic Problems*. Cambridge Texts in Applied Mathematics, Cambridge University Press, 2002.

[42] C.-W. Shu, "Numerical methods for hyperbolic conservation laws (am257)," *Lecture Notes*, 2006.

[43] B. Einfeldt, "On godunov-type methods for gas dynamics," *SIAM Journal on Numerical Analysis*, vol. 25, no. 2, pp. 294–318, 1988.

[44] D. S. Balsara and C.-W. Shu, "Monotonicity preserving weighted essentially non-oscillatory schemes with increasingly high order of accuracy," *Journal of Computational Physics*, vol. 160, no. 2, pp. 405–452, 2000.

[45] C.-W. Shu, "High-order finite difference and finite volume weno schemes and discontinuous galerkin methods for cfd," *International Journal of Computational Fluid Dynamics*, vol. 17, no. 2, pp. 107–118, 2003.

[46] S. Gowda, Y. Ma, A. Cheli, M. Gwozdz, V. B. Shah, A. Edelman, and C. Rackauckas, "High-performance symbolic-numerics via multiple dispatch," *arXiv preprint arXiv:2105.03949*, 2021.

[47] R. R. Hofer, "Development and characterization of high-efficiency, high-specific impulse xenon hall thrusters," tech. rep., University of Michigan, 2004.

[48] J. G. Andrews and R. H. Varey, "The sheath at an electrode close to plasma potential," *Journal of Physics A: General Physics*, vol. 3, pp. 413–420, jul 1970.

[49] I. G. Mikellides, D. M. Goebel, J. S. Snyder, I. Katz, and D. A. Herman, "The discharge plasma in ion engine neutralizers: Numerical simulations and comparisons with laboratory data," *Journal of Applied Physics*, vol. 108, no. 11, p. 113308, 2010.

[50] K. Hara and I. G. Mikellides, *Characterization of low frequency ionization oscillations in Hall thrusters using a one-dimensional fluid model.*

[51] J. Mandal and S. Deshpande, "Kinetic flux vector splitting for euler equations," *Computers & Fluids*, vol. 23, no. 2, pp. 447–478, 1994.

[52] S. Chou and D. Baganoff, "Kinetic flux–vector splitting for the navier–stokes equations," *Journal of Computational Physics*, vol. 130, no. 2, pp. 217–230, 1997.

[53] C. M. Greve, K. Hara, R. S. Martin, D. Q. Eckhardt, and J. W. Koo, "A data-driven approach to model calibration for nonlinear dynamical systems," *Journal of Applied Physics*, vol. 125, no. 24, p. 244901, 2019.

[54] C. M. Greve, M. Majji, and K. Hara, "Real-time state estimation of low-frequency plasma oscillations in hall effect thrusters," *Physics of Plasmas*, vol. 28, no. 9, p. 093509, 2021.

[55] *Chapter 6: The ensemble Kalman filter*, pp. 153–193.

[56] A. A. Emerick and A. C. Reynolds, "Ensemble smoother with multiple data assimilation," *Computers & Geosciences*, vol. 55, pp. 3–15, 2013. Ensemble Kalman filter for data assimilation.

Appendix A

The individual efficiencies contributing to the Hall thruster anode efficiency model Equation 5.2 first defined by Hofer [47] are presented here.

η_m represents the mass utilization efficiency. It is defined as the ratio between ion mass flow rate at the outflow $\dot{m}_i$ and the anode neutral gas mass flow rate $\dot{m}_a$.

$$\eta_m = \frac{\dot{m}_i}{\dot{m}_a} \tag{A.1}$$

The beam utilization efficiency η_b relates the ion beam current I_b to the total discharge current I_d. The ion beam current is the total ion current at the outflow.

$$\eta b = \frac{I_b}{I_d} \tag{A.2}$$

η_d is the divergence efficiency. It is a measure of the ion beam collimation, where I_{bz} is the purely axial component of the total ion beam current.

$$\eta_d = \cos^2 \theta_d = \left(\frac{I_{bz}}{I_b} \right)^2 \tag{A.3}$$

The voltage utilization efficiency η_v relates the discharge voltage to the effective acceleration voltage V_a. V_a is defined as the equivalent potential required to accelerate an ion to the mean ion exit velocity, which results from a simple energy balance (shown here for singly charged ions) $qV_a = \frac{1}{2} m_i u_i^2$.

$$\eta_v = \frac{V_a}{V_d} \tag{A.4}$$

η_q is the charge utilization efficiency, which corrects for multiply charged ions. Z_j refers to the charge state.

$$\eta_q = \frac{\left(\sum_{j=1}^{3} \Omega_j / \sqrt{Z_j} \right)^2}{\sum_{j=1}^{3} \Omega_j / Z_j} \tag{A.5}$$

Appendix B

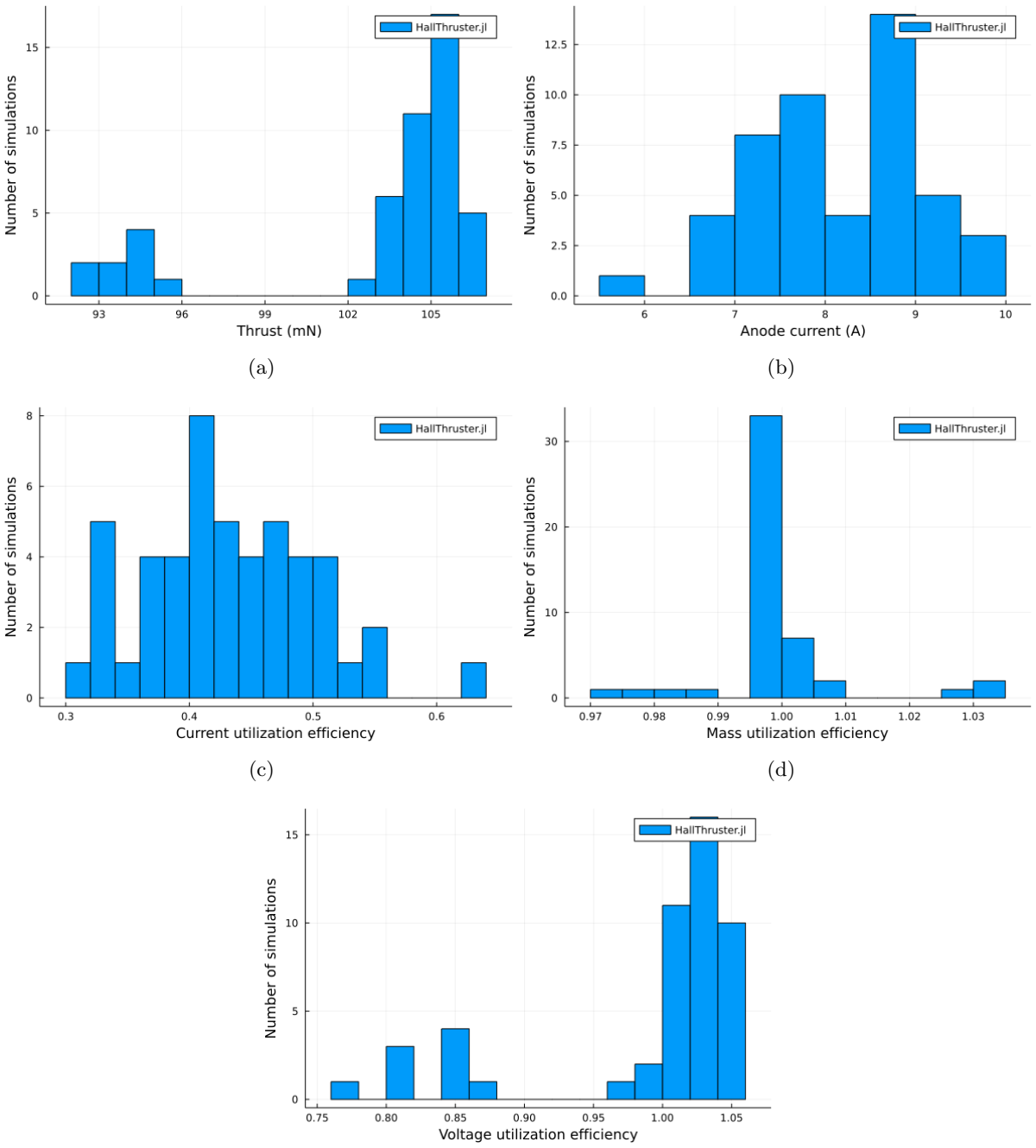

Figure B.1: Sensitivity of efficiency components to coefficients in anomalous collision frequency model

Appendix C

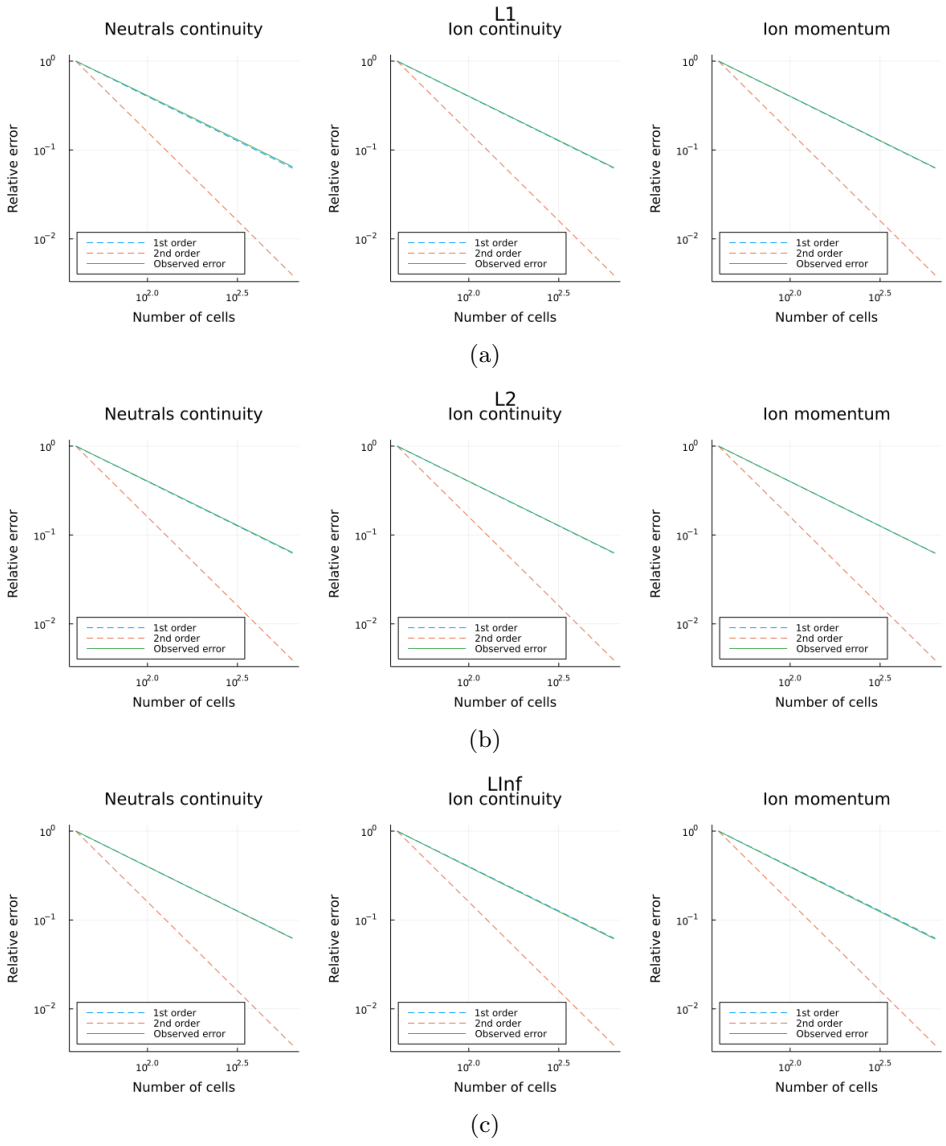

Figure C.1: OVS of neutrals and ions, HLLE flux, piecewise constant reconstruction, first order, wavenumber = 1

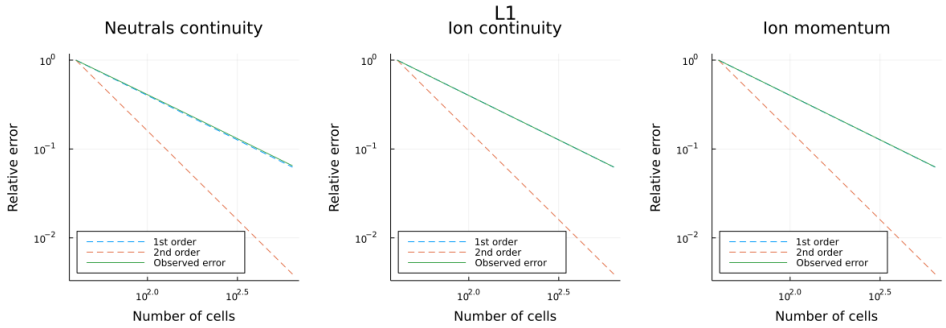

(a)

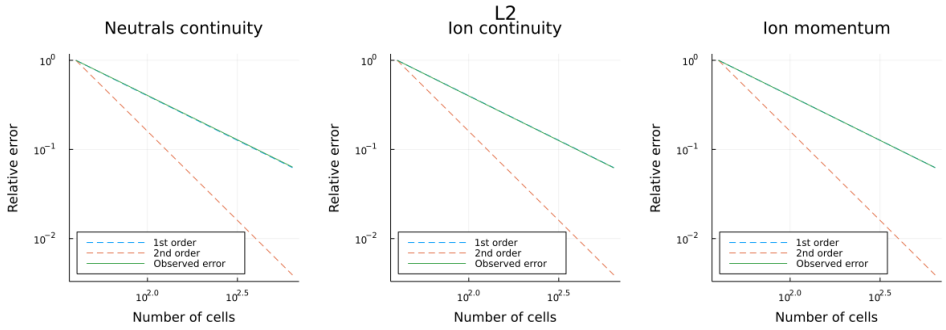

(b)

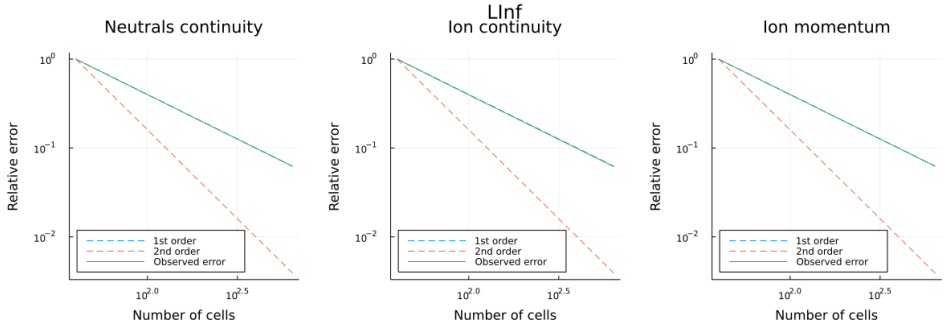

(c)

Figure C.2: OVS of neutrals and ions, HLLE flux, piecewise constant reconstruction, first order, wavenumber = 2

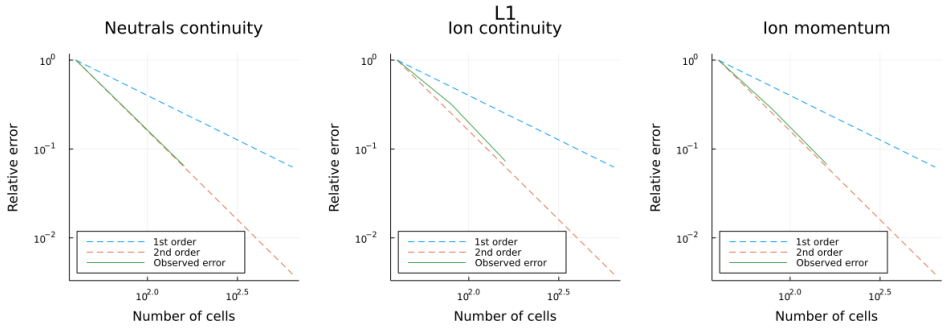

(a)

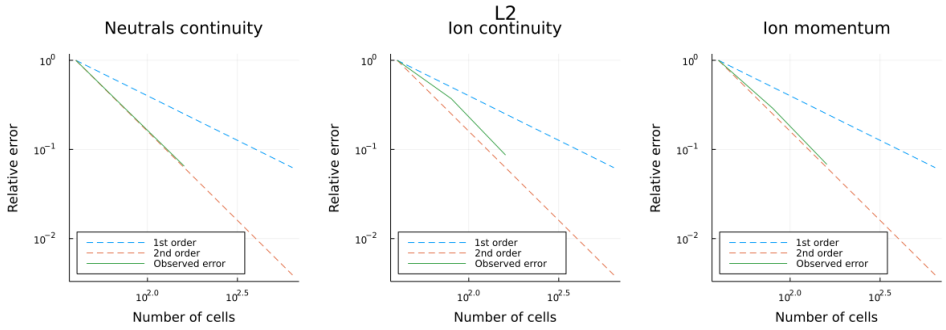

(b)

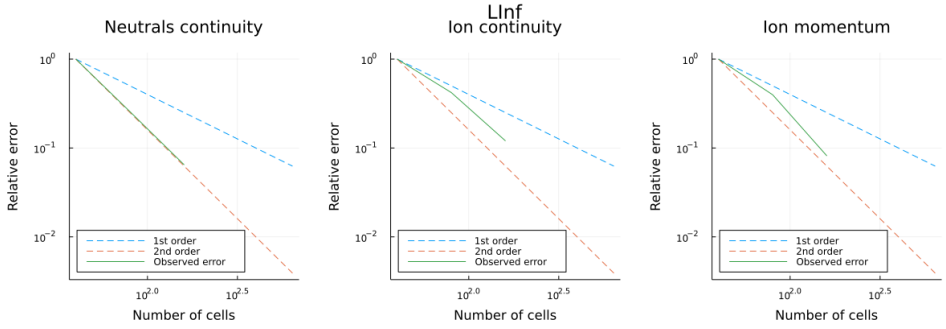

(c)

Figure C.3: OVS of neutrals and ions, HLLE flux, minmod limiter, piecewise linear reconstruction, wavenumber = 1

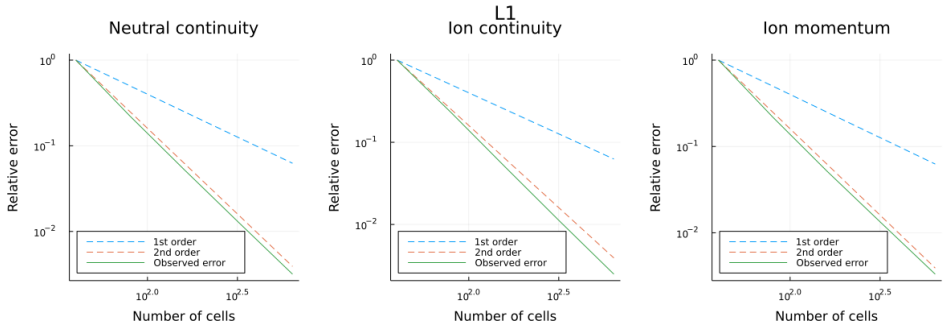

(a)

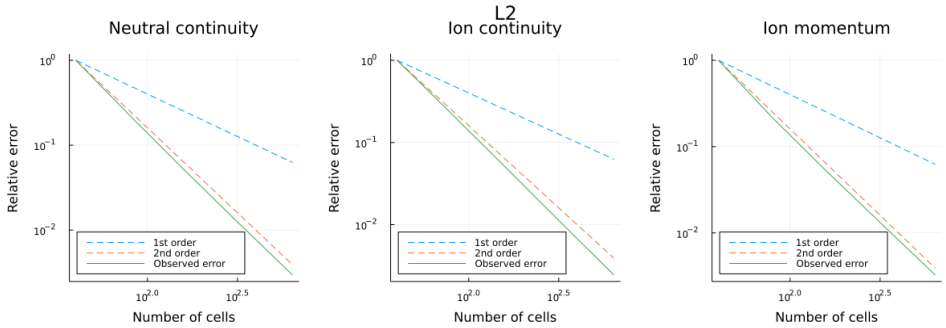

(b)

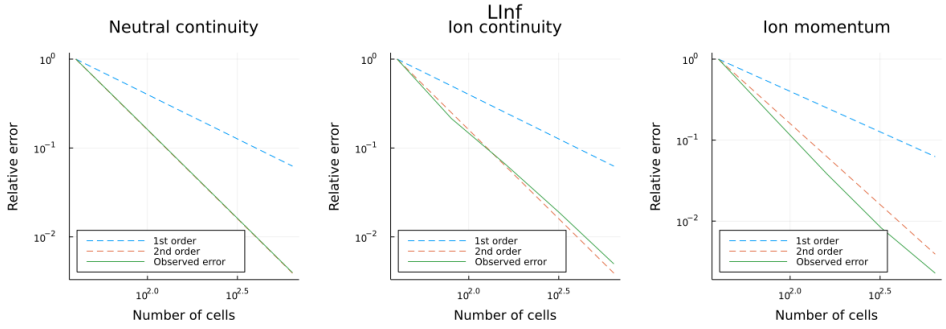

(c)

Figure C.4: OVS of neutrals and ions, HLLE flux, osher limiter, piecewise linear reconstruction, wavenumber = 1

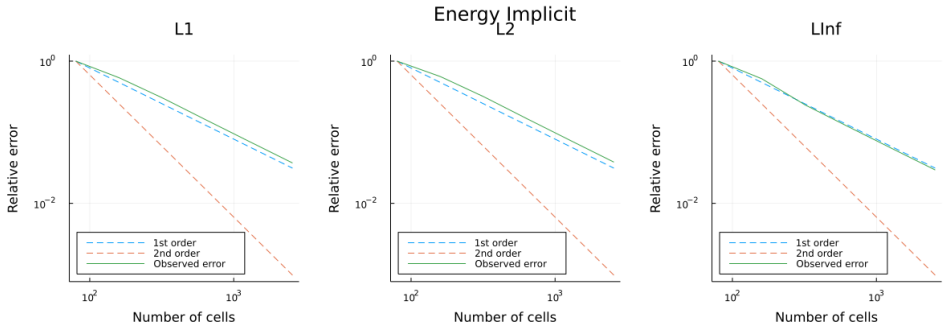

Figure C.5: OVS of electron energy equation, implicit time integration, first order

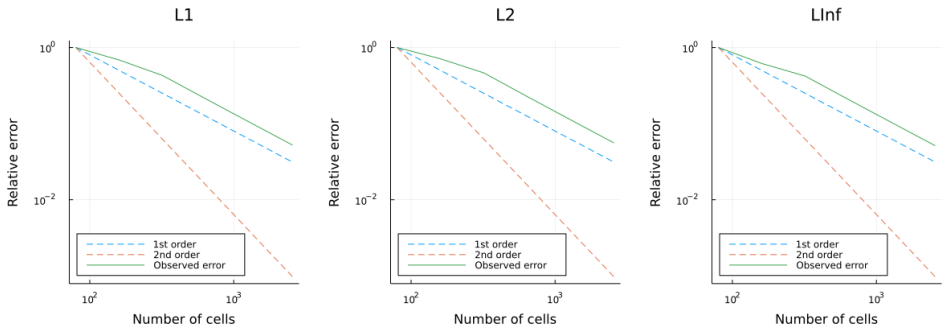

Figure C.6: OVS of electron energy equation, Crank Nicholson time integration, first order

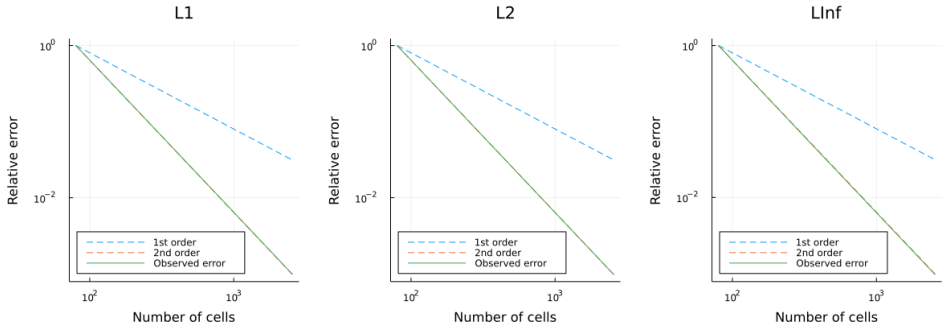

Figure C.7: OVS of electron energy equation, implicit time integration, second order

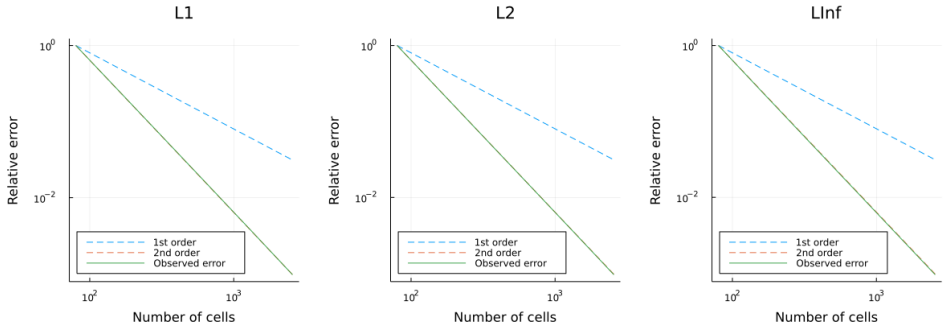

Figure C.8: OVS of electron energy equation, Crank Nicholson time integration, second order

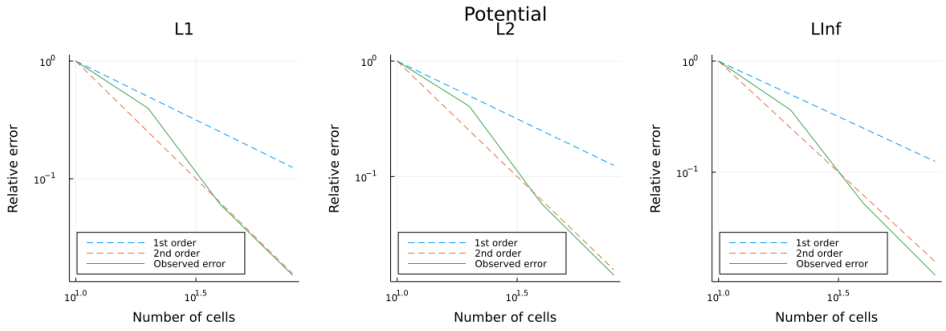

Figure C.9: OVS of potential, second order

Eidgenössische Technische Hochschule Zürich
Swiss Federal Institute of Technology Zurich

Declaration of originality

The signed declaration of originality is a component of every semester paper, Bachelor's thesis, Master's thesis and any other degree paper undertaken during the course of studies, including the respective electronic versions.

Lecturers may also require a declaration of originality for other written papers compiled for their courses.

I hereby confirm that I am the sole author of the written work here enclosed and that I have compiled it in my own words. Parts excepted are corrections of form and content by the supervisor.

Title of work (in block letters):

1D fluid model for a Hall Thruster discharge

Authored by (in block letters):

For papers written by groups the names of all authors are required.

Name(s):	**First name(s):**
Schedler	Paul

With my signature I confirm that

- I have committed none of the forms of plagiarism described in the 'Citation etiquette' information sheet.
- I have documented all methods, data and processes truthfully.
- I have not manipulated any data.
- I have mentioned all persons who were significant facilitators of the work.

I am aware that the work may be screened electronically for plagiarism.

Place, date	**Signature(s)**
Ann Arbor, MI, United States, 04/27/2022	

For papers written by groups the names of all authors are required. Their signatures collectively guarantee the entire content of the written paper.